2018

Design And Fabrication Of Particle-Embedded Polymer Composite Films For Optimized Light-Modulation

Hye-Na Kim
University of Pennsylvania, hyena1015@gmail.com

Recommended Citation

Kim, Hye-Na, "Design And Fabrication Of Particle-Embedded Polymer Composite Films For Optimized Light-Modulation" (2018). *Publicly Accessible Penn Dissertations*. 3136.
https://repository.upenn.edu/edissertations/3136

Design And Fabrication Of Particle-Embedded Polymer Composite Films For Optimized Light-Modulation

Abstract

ABSTRACT

In this dissertation, we develop new composite optical materials by the assembly of silica nanoparticles (NPs) into micron-scaled geometries and embedding them into selected polymer media to achieve tunable and synergistic optical properties for potential applications, including photovoltaics, photobioreactors, or solar-integrated smart windows. The size and the refractive index of NPs, and the geometric arrangements are explored to optimize the targeted optical properties, including forward scattering and the reflectance of light. We also explore different types of the polymer matrix to allow for matching refractive index or introducing stimuli-responsive light scattering.

Firstly, we develop a novel design of semi-transparent composite films for delivering equal and optimally efficient “doses” of sunlight to photosynthetic cells, algae, in a photobioreactor system. The efficient re-distribution of solar flux can allow the algae to receive spatially diluted solar flux and thus avoid photodamages from the direct sunlight. We develop colloidal NPs are assembled into microspheres via water-based emulsion evaporation method which is easy to set up and suitable for large-scale fabrication. Backed by numerical calculations, the overall shape/size of the microsphere and the effective refractive index of the composites are optimized, the synthetic scatterers that recapitulate the salient forward-scattering behavior of the Tridacnid clam system are presented. These hierarchically structured beads also generate various structural colors due to the periodic packing of NPs, which allows back-reflection of photosynthetically inefficient green or yellow lights depending on the sizes of NPs. Our method is simple yet scalable, cost-effective, and environmentally benign, which inspires new designs for small-footprint biofuel applications.

Secondly, we develop new strategies to tune the optical transmittance via mechano-responsive polymers. Stretchable smart window film consisting of an elastomer with micro-scale wrinkles and silica (SiO2) NPs can provide reversible and switchable transparency-opacity. We design and fabricate mechanically responsive films composed of silica NPs and elastomers. By incorporating deformable and controllable wrinkling patterns into the particle-embedded polymer systems with wrinkles and NPs on opposite side of the films, we achieve the desired transparency at a low mechanical strain (< 20%) without wasting energy. The wavelength, amplitude of wrinkles as well as their local ordering can be fine-tuned by the pre-strain vs. applied strain, particle size, oxygen plasma treatment intensity and time, thus, changing the total amount of light refracted from the curved surfaces. We note that since the nano-/micron-sized voids are created at the interface between NPs and polymer matrix upon stretching, they act as light scatters to “reveal” the embedded structural colors, resulting in drastic transparency-opacity switching. Besides, we fabricate the particle-embedded PDMS composite films with wrinkles on the same side of NPs and demonstrate their mechano-responsive optical properties. We confirm that the formation of ordered wrinkling patterns is impeded by the presence of particles on the surface and the homogeneity of wrinkle formation is increased by higher pre-stretch strain and longer plasma exposure time. Thus, we tune the optical transmittance of films by varying the pre-strains and the size of NPs separately. Our material designs offer new insights on how to fine-tune optical properties with minimal energy consumption for applications including on-demand smart windows and strain sensors.

Degree Type

Dissertation

Degree Name
Doctor of Philosophy (PhD)

Graduate Group
Materials Science & Engineering

First Advisor
Shu Yang

Keywords
composite films, light-modulation, light scattering, nanoparticles, particle assembly, wrinkling patterns

Subject Categories
Engineering | Mechanics of Materials

DESIGN AND FABRICATION OF PARTICLE-EMBEDDED POLYMER COMPOSITE FILMS FOR OPTIMIZED LIGHT-MODULATION

Hye-Na Kim

A DISSERTATION

in

Materials Science & Engineering

Presented to the Faculties of the University of Pennsylvania

in

Partial Fulfillment of the Requirements for the

Degree of Doctor of Philosophy

2018

Supervisor of Dissertation

____

Shu Yang

Professor, Materials Science and Engineering

Graduate Group Chairperson

____

I-Wei Chen, Skirkanich Professor of Materials Innovation

Dissertation Committee

Alison Sweeney, Associate Professor, Physics and Astronomy

Randall Kamien, Vicki and William Abrams Professor in the Natural Sciences

Christopher Murray, Richard Perry University Professor of Chemistry and Materials Science and Engineering

DESIGN AND FABRICATION OF PARTICLE-EMBEDDED POLYMER COMPOSITE FILMS FOR OPTIMIZED LIGHT-MODULATION

To my family

ACKNOWLEDGMENT

Through the journey of my doctorate years, I have been so blessed enough to be associated with many people without whose assistance and encouragement this dissertation would not have been possible. It is my great pleasure to thank invaluable support of my professors, collaborators, peers, friends, and family.

First and foremost, I would like to sincerely thank my advisor, Prof. Shu Yang, for all her encouragement, guidance, patience, and invaluable support throughout my doctorate years. She has dedicated a great amount of effort and time to support me in scientific accomplishments as well as my presentation skills, critical thinking skills, and scientific writing. She also taught me how to design research plans and address challenges. Her deep and outstanding inspirations have always guided me and my research in the right direction. Especially, her expertise through interdisciplinary collaborations has motivated me all the time throughout my journey in graduate years. I really appreciate her contribution of time, ideas, and encouragement eventually helped me to grow to be a material scientist. It has been an honor for me to be her Ph.D. student.

I would like to thank my committee members, Professors Alison Sweeney and Randall Kamien of the Department of Physics and Astronomy and Prof. Christopher Murray of the Department of Materials Science and Engineering and Department of Chemistry, for serving as my committee members and supporting me throughout my doctorate studies with guidance, advice, inspiration, suggestions, and feedback to me for the research proposal and all the annual research updates.

I would like to acknowledge all my collaborators for sharing their ideas and knowledge and encouraging me to accomplish my research in novel directions. I would like to acknowledge Professor Alison Sweeney, Dr. Sanaz Vahidinia, and Dr. Amanda Holt at the Department of Physics and Astronomy for their efforts and the great work they provided in our collaboration. I could get a lot of insights from their theoretical and experimental studies in giant clams. I thank Dr. Dengteng Ge and Dr. Elaine Lee who have been my great collaborators and mentors for many years since we first met in Yang group. I thank Prof. Aaswath Raman, Dr. Lisa Tran, Dr. Yijie Jiang, and Dr. Wenxiang Chen, for invaluable discussion they provided during the interdisciplinary collaboration.

I also would like to thank Professor Kathleen Stebe of the Department of Chemical and Biomolecular Engineering and Professor Russell Composto of the Department of Materials Science and Engineering, Professor Randall Kamien of the Department of Physics and Astronomy, and Professor Francesca Serra of the Department of Physics and Astronomy at Johns Hopkins University, for their guidance in cross-departmental liquid crystal projects where I worked as a contributing researcher. I thank Prof. Cherie Kagan and Prof. Russell Composto for granting me access to UV-Vis-NIR spectrometer. I also thank Prof. Christopher Murray for granting me access to FTIR.

I would like to thank all the present and past members of Yang group for being the source of friendships, good advice, and collaboration, including Dr. Su Yeon Lee, Dr. Younghyun Cho, Dr. Dengteng Ge, Prof. Francesca Serra, Dr. Mohamed Amine Gharbi, Dr. Yigil Cho, Dr. Apiradee Honglawan, Prof. Lili Yang, Dr. Gaoxiang Wu, Dr. Yu Xia, Dr. Alei Deng, Dr. Hyesung Cho, Dr. Hongsuk Kang, Dr. Weerapha Panatdasirisuk, Prof. Xiaoming Yang, Zhiwei Liao, Jiaqi Liu, Heesuk Jung, Jason Christopher Jolly, Yuchong (Arden) Gao, Yuchen Wang, Dr. Se-um Kim, Dr. Wei-Liang Chen, Dr. Dae Seok Kim, Dr. Saihua Jiang, Dr. Xu Zhang, Prof. Bi Xu, Kyudong (Ryan) Noh, Dr. Eusun Yu, Sun

Mi Yoon, Jihoon Lee, Geuntae Yun, Euiyeon Jung, Shenglan Chen, Luke Shi, Evan Dolling, Samagata Sen, Sam Burns, Vidyanand Wagh, Songnan Zhang, Rui Yin, Xinyue Zhang, and Huseyin Kaya.

I would like to acknowledge my MSE friends, including Joongho Shin, Dr. Dequan Er, Liyan Wu, Fan Yang, Boris Rasin, Dr. Joohee Park, and Dr. Jongho Lee. I would like to thank the past MSE seniors, including Dr. Soong Ju Oh, Dr. Albert Chen, Dr. Nicholas Greybush, Dr. L. Robert Middleton, Dr. Sharon Sharick, and Dr. Zoey Davidson. I also thank my friends from Penn, especially Dunbee Choi, and my friends in Korea, especially Miae Kim and Dr. Changyeol Cho. They have been there for me through all the tough times of my long journey in Ph.D. years.

I am grateful to Nanoscale Characterization at Singh Center for Nanotechnology access to SEM, FIB, and AFM, especially to Dr. Jamie Ford and Dr. Matthew Brukman with the training and support on these instruments. I acknowledge Quattrone Nanofabrication at Singh Center for Nanotechnology for access to direct laser writer and RIE, especially to Hiromichi Yamamoto, Eric Johnston, David Jones, Dr. Gyuseok Kim, and Dr. Gerald Lopez for arranging the tool trainings for me and helping me with the equipment manuals. I thank Steve Szewczyk who helped me so many instruments in our department, such as DSC, TGA, furnaces, UV-Vis, and home-built optical set-ups. Besides, I am grateful to the LRSM staff. Felice Macera who kindly helped me a lot with sample imaging and the cover image design. I also thank Pat Overend, Irene Clements, Vicky Lee, Enrique Vargas, and Raymond Hsiao, for offering me help whenever necessary.

Besides, I would like to acknowledge my former advisor, Prof. Jun Hyuk Moon at Sogang University in Korea, for all his encouragement and advice throughout my graduate studies.

Finally, I would like to dedicate my thesis to my parents and my sister. I could not have gone so far in the long journey of Ph.D. without their unconditional love and sacrifice. I am deeply grateful to my mother, Aeseon Yang, for her love and sacrifice. I truly thank my father, Dongnam Kim, though no longer with us on Earth, his love is always with me. My parents have always been there for me and have encouraged me to pursue my dream fearlessly. I truly thank my lovely younger sister, Hyejin Kim, who has always been there for me as the best sister and the best friend.

ABSTRACT

DESIGN AND FABRICATION OF PARTICLE-EMBEDDED POLYMER COMPOSITE FILMS FOR OPTIMIZED LIGHT-MODULATION

Hye-Na Kim

Shu Yang

In this dissertation, we develop new composite optical materials by the assembly of silica nanoparticles (NPs) into micron-scaled geometries and embedding them into selected polymer media to achieve tunable and synergistic optical properties for potential applications, including photovoltaics, photobioreactors, or solar-integrated smart windows. The size and the refractive index of NPs, and the geometric arrangements are explored to optimize the targeted optical properties, including forward scattering and the reflectance of light. We also explore different types of the polymer matrix to allow for matching refractive index or introducing stimuli-responsive light scattering.

Firstly, we develop a novel design of semi-transparent composite films for delivering equal and optimally efficient “doses” of sunlight to photosynthetic cells, algae, in a photobioreactor system. The efficient re-distribution of solar flux can allow the algae to receive spatially diluted solar flux and thus avoid photodamages from the direct sunlight. We develop colloidal NPs are assembled into microspheres via water-based emulsion evaporation method which is easy to set up and suitable for large-scale fabrication. Backed by numerical calculations, the overall shape/size of the microsphere and the effective refractive index of the composites are optimized, the synthetic scatterers that recapitulate

the salient forward-scattering behavior of the Tridacnid clam system are presented. These hierarchically structured beads also generate various structural colors due to the periodic packing of NPs, which allows back-reflection of photosynthetically inefficient green or yellow lights depending on the sizes of NPs. Our method is simple yet scalable, cost-effective, and environmentally benign, which inspires new designs for small-footprint biofuel applications.

Secondly, we develop new strategies to tune the optical transmittance via mechano-responsive polymers. Stretchable smart window film consisting of an elastomer with micro-scale wrinkles and silica (SiO_2) NPs can provide reversible and switchable transparency-opacity. We design and fabricate mechanically responsive films composed of silica NPs and elastomers. By incorporating deformable and controllable wrinkling patterns into the particle-embedded polymer systems with wrinkles and NPs on opposite side of the films, we achieve the desired transparency at a low mechanical strain (< 20%) without wasting energy. The wavelength, amplitude of wrinkles as well as their local ordering can be fine-tuned by the pre-strain vs. applied strain, particle size, oxygen plasma treatment intensity and time, thus, changing the total amount of light refracted from the curved surfaces. We note that since the nano-/micron-sized voids are created at the interface between NPs and polymer matrix upon stretching, they act as light scatters to "reveal" the embedded structural colors, resulting in drastic transparency-opacity switching. Besides, we fabricate the particle-embedded PDMS composite films with wrinkles on the same side of NPs and demonstrate their mechano-responsive optical properties. We confirm that the formation of ordered wrinkling patterns is impeded by the presence of particles on the surface and the homogeneity of wrinkle formation is increased by higher pre-stretch strain and longer plasma exposure time. Thus, we tune the optical transmittance of films by varying the pre-strains and the size of NPs separately. Our material designs offer new insights on how to fine-tune optical properties with minimal energy consumption for applications including on-demand smart windows and strain sensors.

TABLE OF CONTENTS

LIST OF TABLES

LIST OF FIGURES

CHAPTER 1: Particle-embedded polymer composite films for optimized light-modulation

1.1 Introduction

Inorganic nanoparticles (NPs), including quantum dots (QDs), metallic NPs, and stimuli-responsive NPs have been of great interests for light-modulation applications, such as photovoltaics,[1-3] optical smart windows,[4, 5] optical sensors[6], and biomedical applications,[7] due to their unique optical properties.[8-10] For example, semiconducting QDs offer absorption and emission of light at certain wavelengths (see **Figure 1.1**) depending on the size and shape of the particle due to quantum confinement effects. As the size of QDs decreases, the band gap increases, resulting in light emission at shorter wavelengths.[11] In the case of noble metallic (e.g., silver or gold) NPs, they exhibit a resonant oscillation of electrons at a certain energy of the incident light, resulting in optical absorption at a specific wavelength of light, so-called plasmon resonance absorption.[9] As an example, **Figure 1.2** shows that by tuning the aspect ratio of Au NPs, different optical properties (scattering and extinction) can be generated, leading to programmable spectral properties from visible (Vis) to near-infrared (NIR) wavelengths.[12] In the case of stimuli-responsive NPs, often metal oxides, e.g., nickel oxide (NiO), tungsten trioxide (WO_3), and vanadium oxide (VO_2), the optical transmittance or color can be tuned by external stimuli including electrical field,[13, 14] light,[15, 16] and temperature.[17-20]

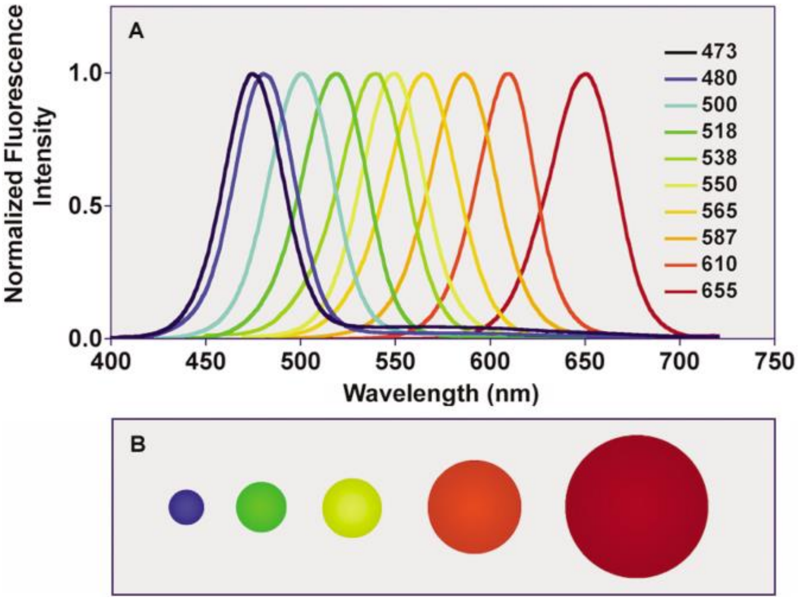

Figure 1.1 Size-tunable fluorescence spectra of CdSe QDs (A) and illustration of the relative QD sizes (B). From left to right, the diameters of QDs are 2.1 nm, 2.5 nm, 2.9 nm, 4.7 nm, and 7.5 nm, respectively. Reproduced from Ref. [11] with permission from The Royal Society of Chemistry.

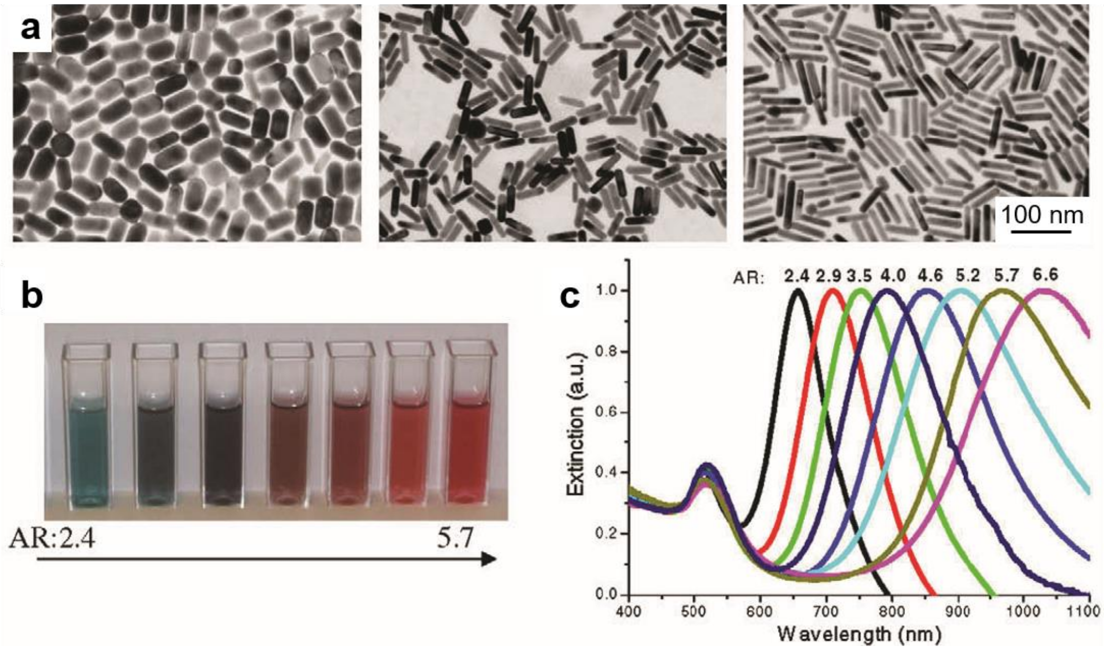

Figure 1.2 Surface plasmonic Au nanorods (NRs) of different aspect ratios (ARs). Transmission electron microscopy (TEM) of Au NRs (a), the corresponding optical images (b), and surface plasmon resonance (SPR) spectra (c). Reproduced from Ref. [12] with permission from Elsevier.

However, these functional inorganic NPs are rather expensive, sometimes chemically or mechanically unstable, and difficult to prepare with uniform size and shape at the nanoscale. Thus, cost-effective and environmentally benign NPs, for example, silica NPs, which are also easy to synthesize and thus scalable, are often of interest to generate tunable optical effects through their assemblies and/or by embedding them in a polymer matrix (see **Figure 1.3**). Polymers are considered as good host materials because they are low-cost, versatile, and easy to process into various geometries to tailor the optical properties.[21] By carefully matching the refractive indices of NPs and polymer matrix, surface chemistry, as well as their mechanical properties, particle-embedded polymer composites can exhibit synergistic effects with improved chemical/mechanical stability, enhanced dispersion of NPs, and optimized, and sometimes stimuli-responsive, optical properties. Typically, polymers are used as dielectric media for embedding chemically vulnerable optical NPs (e.g., metallic NPs, QDs, metal oxide NPs). Polymers can also be used as media to enhance the dispersion of NPs or tune the effective refractive indices of composite films. Further, by embedding NPs into a polymer matrix that is responsive to external stimuli, one can induce dynamic tuning of the spacing between the NPs and the arrays of them, leading to tunable optical properties of the systems. **Table 1.1** summarizes different types of particle-polymer composite films for light-modulation applications.

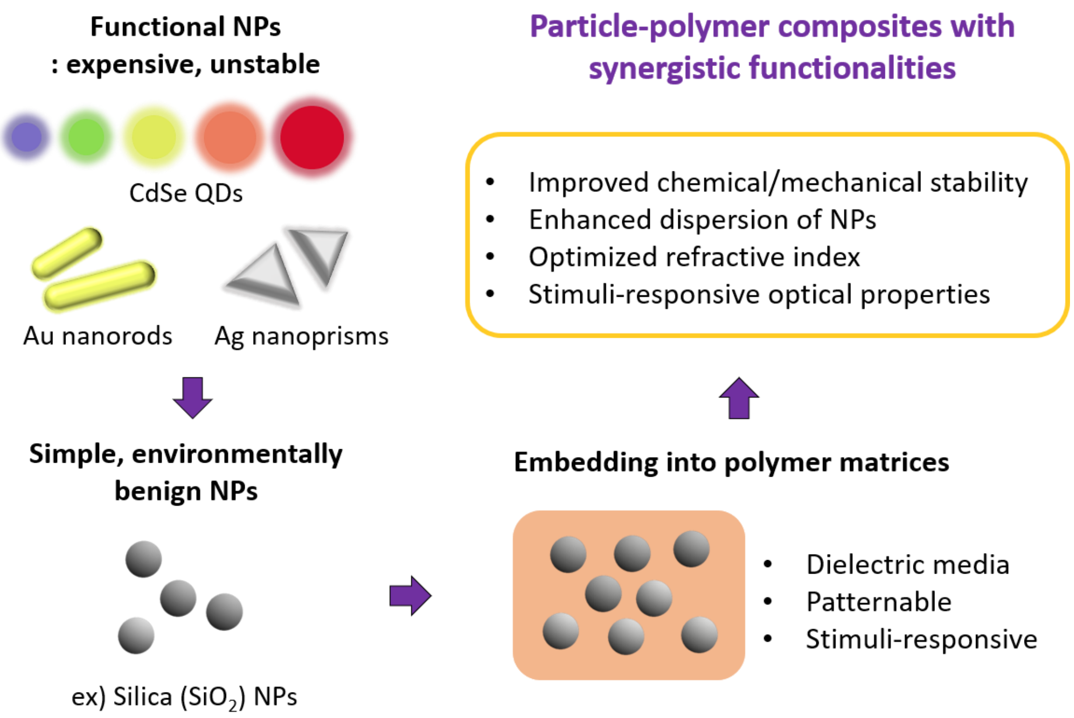

Figure 1.3 Overview of the design for nanoparticle-embedded polymer composites with optimized optical properties.

Table 1.1 Examples of particle-polymer composite films for light-modulation applications.

NPs	**Polymers**	**Targeted optical properties**	**Static or stimuli-responsive**	**Applications**
Metallic NPs-embedded polymer composite films				
AgNPs,[22] Au nanoplates [23]	Polyvinyl alcohol (PVA)	Plasmon resonance absorption	Static	Optical limiting application
AgNPs[24]	Polyethylene terephthalate (PET)	Plasmon resonance absorption	Static	Bandpass filters
AgNPs[25]	Poly(2-hydroxyethyl methacrylate) (HEMA)-based hydrogels	Surface plasmon resonance	pH-responsive	Drug delivery and other applications

AuNPs[26]	Polydimethylsiloxane (PDMS)	Plasmon resonance absorption	Mechano-responsive	Biosensing and solar energy harvesting
AuNPs[27]	Poly(N-isopropylacrylamide) (PNIPAAm)	Plasmon resonance absorption, surface-enhanced Raman scattering (SERS)	Thermo-responsive	Biosensing
AuNPs /PNIPAAm[28]	Polyacrylamide (PAAm) hydrogel	Plasmonic absorbance	Thermo-responsive	Colorimetric thermometers
High-refractive-index NPs-embedded				
TiO_2 NRs (anatase)[29]	Poly(methyl methacrylate) (PMMA)	Transmittance and reflectance in 0.5–2.5 μm range (high refractive-index)	Static	Optical sensor devices
Hollow SiO_2 NPs[30]	UV-curable polymers (acrylate-based)	High diffusive transmittance (Vis-NIR)	Static	Optical diffusers in the back-light unit of LCDs
TiO_2[31]	Polyimide (PI)	Absorbance (UV-Vis)	Static	
QDs-embedded polymer composite films				
QDs (CdSe/ZnS, CdS/ZnS)[32]	Poly(laurylmethacry-late) (PLMA)	Photoluminescence (PL) (UV-Vis-NIR)	Electro-chromic	Full color displays
QDs (PbS)[33]	Polythiourethane (PTU)	UV-vis transmittance (high refractive-index)	Electro-chromic	Filters and antireflection films
Organometal halide perovskites (OHPs)[34]	Poly(vinylidene fluoride) (PVDF)	Photoluminescence, optical transmittance (Vis-NIR)	Electro-chromic	Display backlights
Stimuli-responsive NPs-embedded				
Vanadium dioxide(VO_2) NPs[35]	Polyurethane (PU)	Optical transmittance (UV-Vis-NIR)	Thermo-responsive	Smart windows
Vanadium dioxide (VO_2) NPs[36]	Copolymers of methacrylic acid and ethyl acrylate	Optical transmittance (UV-Vis-NIR)	Thermo-responsive	Smart windows
Tungsten trioxide(WO_3)[37]	PVA	Optical transmittance (UV-Vis)	Photo-chromic	Smart windows
Light-absorbing NPs-embedded				

Graphene flakes[38]	PDMS	Absorption, transmission, and reflectance in 0.4–200 µm range	Static	Sensing, or ultrafast photonics
Birefringence-inducing NPs-embedded				
Cellulose nanowhiskers [39]	PVA	Transmittance (UV-Vis), birefringence	Static	Security papers

Polymers, including poly(vinyl alcohol) (PVA), polydimethylsiloxane (PDMS), poly(methyl methacrylate) (PMMA), and polyimide (PI), are common host materials that are used to protect NPs, especially metallic NPs, metal oxide NPs, and semiconductor QDs that are typically vulnerable to unwanted oxidation because of their high chemical reactivity and high surface-to-volume ratios.[31, 40-42] Specifically, PVA (dielectric constant, ε = ≈5.0 at 1kHz, ≈32 °C)[43] has been commonly used for metallic NPs due to its remarkable chemical resistance, thermostability, flexibility, high mechanical strength as well as high dielectric permittivity.[22, 23, 40, 44] As shown in **Figure 1.4**, PVA thin films are embedded with bimetallic NPs of Ag-Au for generating tunable surface enhanced Raman scattering (SERS) with maximal enhancement factor (EF).[44] The composite film exhibit tunable localized surface plasmon resonance (LSPR) peak across a range of wavelengths (λ = 434 nm - 761 nm), showing a blue shift of the extinction peak with respect to the laser excitation wavelength. As another example of dielectric host materials, PDMS has been used to provide composite films that are flexible, transparent, and able to retain photophysical properties of QD NPs. As shown in **Figure 1.5**, the preparation of organometallic halide perovskite (OHP) QDs embedded in PDMS films is demonstrated with the precise control of QD size, improved stability, and retention of their photophysical properties.[45] A porous PDMS film is prepared by blending AuNPs with the PDMS prepolymer, followed by curing and selective removal of AuNPs. Using porous PDMS as a template for QD growth, the aggregation of methylammonium lead trihalide ($MAPbX_3$, where X = Br) QD is prevented since each QD is isolated within the polymer. Further, PDMS blocks direct contact of QDs with the ambient environment, thus, further improving stability of the QDs. $MAPbBr_3$ QDs/PDMS film shows the same X-ray powder diffraction (XRD) pattern even after several months.[45]

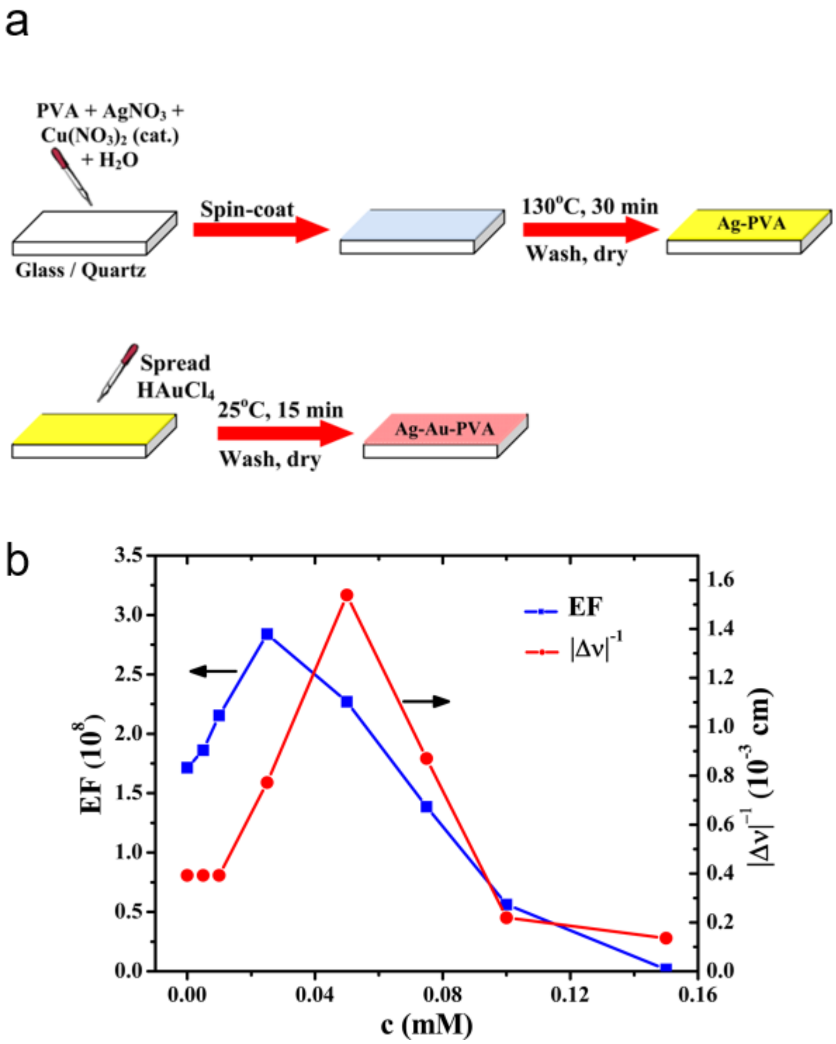

Figure 1.4 Ag-Au NP-embedded polymer thin films with tunable SERS responses. (a) Schematic illustration of the *in-situ* synthesis of a Ag-PVA film, followed by the introduction of Au precursor, $HAuCl_4$, to create a Ag-Au-PVA thin film. (b) SERS enhancement factor (EF) and $|\Delta\nu|^{-1}$ vs. concentration of $HAuCl_4$ aq. solution (c, mM) used to prepare the Ag-Au-PVA thin film. c = 0 corresponds to the Ag-PVA thin film. $\Delta\nu = \nu_I - \nu_{LSPR}$ where ν_I = frequency of the excitation laser, ν_{LSPR} = frequency of the LSPR peak for the Ag-PVA or Ag-Au-PVA thin film (b). Reprinted with permission from Ref. [44]. Copyright © (2015) American Chemical Society.

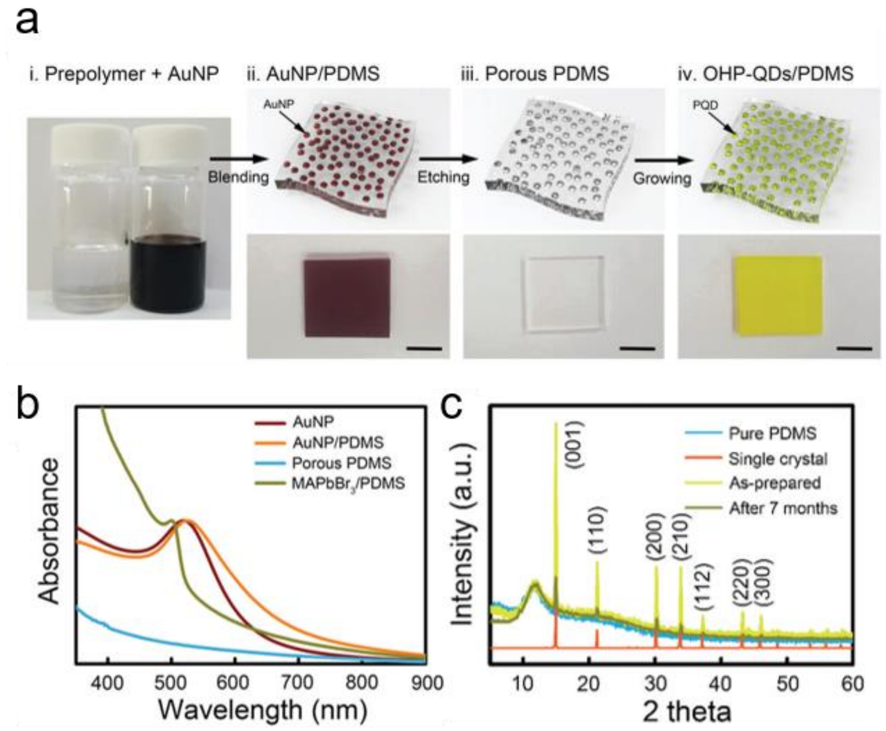

Figure 1.5 (a) Schematic illustration of the synthesis of OHP-QDs/PDMS film. The photographs show the color of the films at each stage (scale bar = 1 cm). (b) The absorption spectra of AuNPs in toluene: dark red. AuNPs/PDMS: orange. porous PDMS: sky blue. $MAPbBr_3$ QDs/PDMS (dark green). (c) High resolution XRD patterns of pure PDMS (blue), a ground $MAPbBr_3$ single crystal (orange), the as-prepared $MAPbBr_3$ QDs/PDMS film (yellow), and the $MAPbBr_3$ QDs/PDMS film aged for several months under ambient conditions (dark green). Reproduced from Ref. [45] with permission from The Royal Society of Chemistry.

Meanwhile, PMMA,[29] UV-curable polymers (e.g., acrylate-based),[30] and PI[31] have been used to disperse metal oxide NPs (e.g., TiO_2, ZnO, or hollow SiO_2), allowing for in-situ fabrication of composite films with homogeneity and high stability. Specifically, PI films can exhibit an exceptional combination of high thermal stability (>500 °C) and mechanical toughness (tensile strength, ≈207 MPa).[46] Thus, PI can be mixed with various inorganic metal oxides by in-situ polymerization or sol-gel processes.[47] Besides, polyurethane (PU)[35] or copolymers of methacrylic acid and ethyl acrylate[36] can be used to uniformly disperse thermochromic VO_2 NP composites that are inherently easy to be aggregated, thus providing homogeneous composite films followed by coating on substrates. Thereby, sustainable thermo-responsive optical films can be utilized in the applications of thermo-responsive solar cells or temperature-responsive smart windows.[35, 36] Moreover, particle aggregation in dispersions can be controlled during the fabrication process of polymer films, allowing for efficient management of optical characteristics.[48] For example, bulk hybrids were fabricated by in situ polymerizations of MMA with dispersed TiO_2 NPs modified with PMMA chains (see **Figure 1.6**).[49] The transparency of the hybrids depends on the chain length of the PMMA grafted on the NPs: when the molecular weight of PMMA is too short, it would lead to aggregation of the TiO_2 NPs during the in-situ polymerization process, which scatters light.

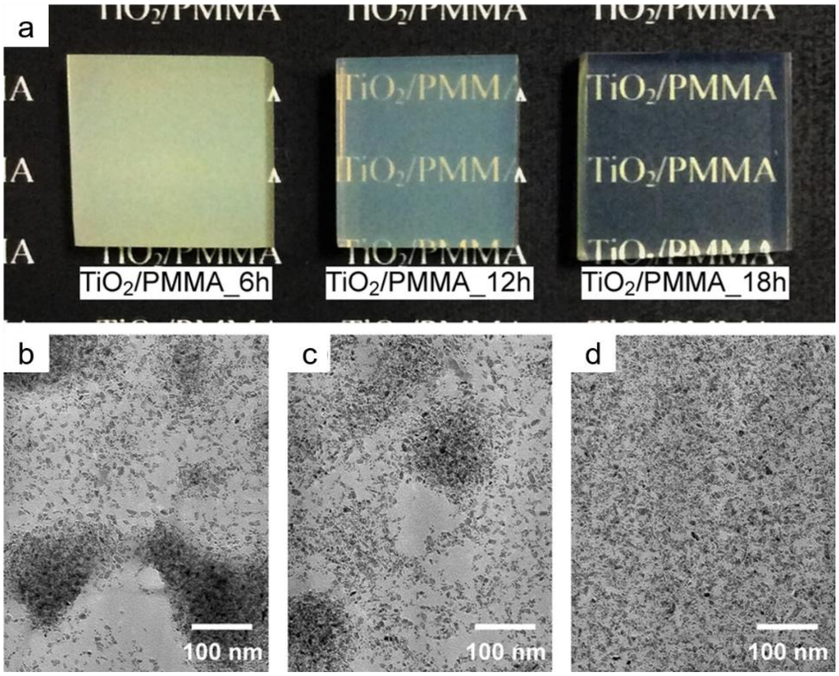

Figure 1.6 (a) Photographs of bulk TiO_2/PMMA hybrids (thickness: 5 mm). TEM images of TiO_2/PMMA-6h (6.3 vol %) (b), TiO_2/PMMA-12h (6.2 vol %) (c), and TiO_2/PMMA-18h (6.3 vol %) hybrids (d). Reprinted with permission from Ref. [49]. Copyright © (2016) American Chemical Society.

Refractive index (n) is an important characteristic for optimizing the optical properties. The effective refractive index of the composite material, $n_{composite}$, can be estimated by the Arago-Biot formula,[50, 51] $n_{composite} = \phi_{particle} n_{particle} + \phi_{polymer} n_{polymer}$, where $n_{particle}$, and $n_{polymer}$ are the refractive indices of NP and polymer, respectively, and $\phi_{particle}$ and $\phi_{polymer}$ are the volume fractions of the NPs and polymer matrix, respectively. Since many high refractive index NPs are light absorbing, for the design of high-refractive-index nanocomposites, overloading of NP s will not only lower light transmission but also decreases the processability of the composite films.[52] For a targeted $n_{composite}$ value and a given type of NPs, we can choose polymers with higher refractive index to the lower the $\phi_{particle}$. This is significant for the designs of high-n composites for light-modulating applications because overloading NPs often decreases transparency of the polymer matrix. Thus, one of the common strategies for this is to use sulfur-containing PIs, which have high-n values in the range of 1.680-1.769, as host matrices for high-n NPs, including TiO_2 (anatase, $n = 2.45$, and rutile, $n = 2.70$), PbS ($n = 4.20$), and ZnS ($n = 2.36$). Especially, a refractive index greater than 1.7 is highly desired for applications such as microlenses for image sensors, encapsulants for LEDs, and high-index thermoplastic lenses.[52]

Another common strategy to tune optical properties is to use stimuli-responsive polymers that can change the particle dispersion/clustering and spacing in response to, e.g., mechanical force, temperature, and pH. In the case of metallic NPs-embedded composite films, the position of the plasmon absorption peak and the absorption intensity depend strongly on the distance between NPs, their arrangement, as well as the chemistry, composition, size and shape of the NPs, and dielectric constant of the polymer matrix.[53] PDMS is an elastomeric material that is stretchable and flexible. In NPs/PDMS films, the spacing between NPs can be changed, or air voids can be introduced upon stretching of PDMS, leading to change of color or optical transparency.[54-57] As shown in **Figure 1.7**, Ge et al. demonstrated a composite film consisting of a thin layer of quasi-amorphous array of silica NPs embedded in an elastomeric PDMS matrix. Initially, the film looks transparent (>90% transmittance in the visible wavelength) since the refractive indices are matched in the system. Upon mechanical stretching, the transmittance is drastically reduced to 30% due to the increased refractive index contrast by air voids. The film shows angle-independent structural color at a strain >40% and the color can be tuned by the size of silica NPs.[56]

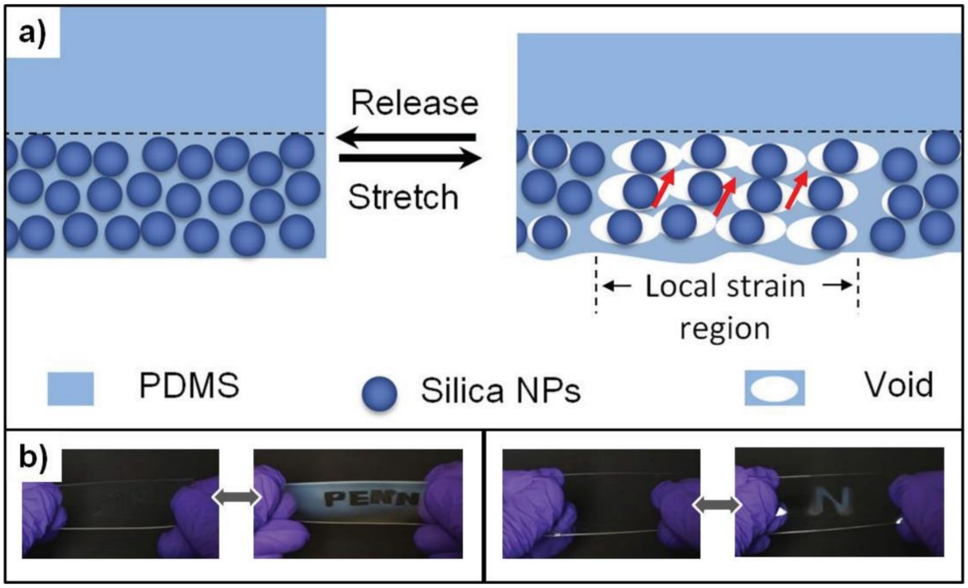

Figure 1.7 (a) Schematic illustration of the void formation around the silica particles when stretched. The arrows indicate PDMS ligaments. b) Optical images showing reversible revealing and hiding of the letters patterned within the silica nanoparticle/PDMS film under mechanical stretching and releasing. Reproduced with permission from reference [56]. Copyright © 2015, John Wiley and Sons.

Poly(N-isopropylacrylamide) (PNIPAAm) is a commonly used temperature-responsive polymer, which has a lower critical solution temperature (LCST) at ≈32 °C. PNIPAAm has been used as a polymer graft on colloidal particle surface or as a gel matrix to fine-tune SERS for biosensing or detecting environmental changes and.[58, 59] **Figure 1.8** shows a facile thermo-responsive color change by the preparation of raspberry-shaped PNIPAAm plasmonic microgels decorated with AuNPs, which allows reversible and temperature-responsive color shifts (between red and grayish violet). A responsive colorimetric patch containing a plasmonic microgel exhibits a considerable extinction peak shift (176 nm) in 1 sec, with a temperature-sensing resolution of 0.2 °C.[59]

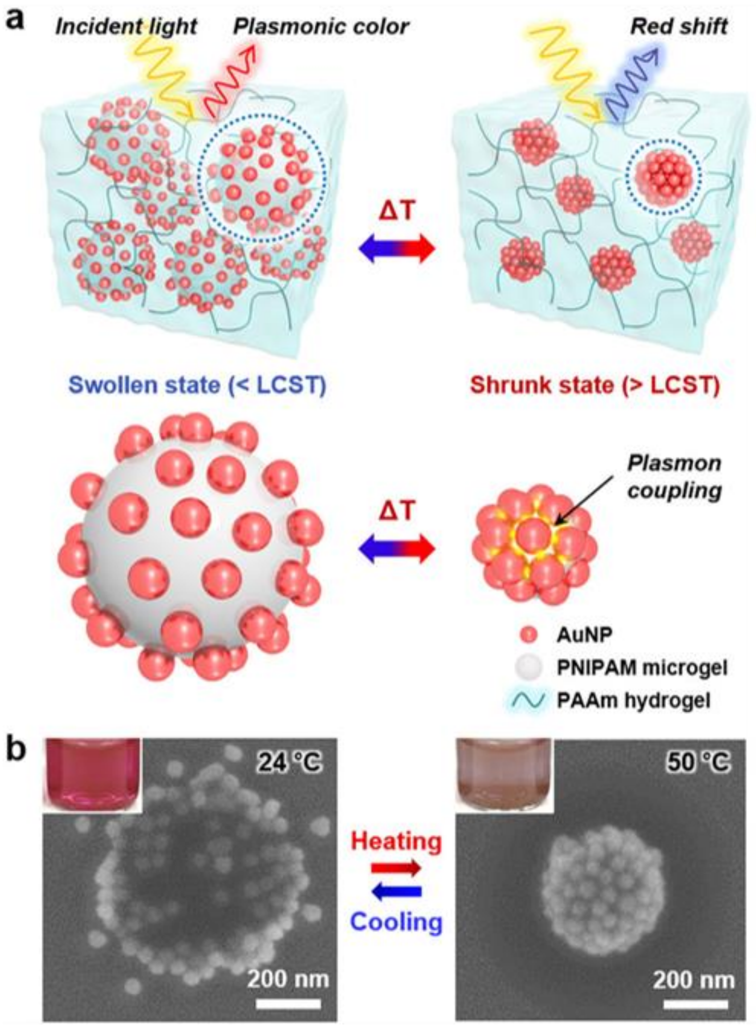

Figure 1.8 The operating principle of a thermo-responsive colorimetric sensor. (a) Schematic illustration of the plasmonic microgels in the PAAm hydrogel under swollen and shrunk states. (b) SEM images of the plasmonic microgels with 51 nm AuNPs under the swollen state at 24 °C (left) and under the shrunken state at 50 °C (right). The inset images show pictures of the plasmonic microgel dispersions under each condition. Reproduced from reference [59]. Copyright link: http://creativecommons. org/licenses/by/4.0.

Among many particle-polymer composite systems, the challenges include fabrication and control of the optical properties. In addition, many optical devices are based on nanostructures, which have low defect tolerance, putting additional constraint in fabrication. Nature has offered many optimized optical systems with high efficiency and defect tolerance from microstructures (see **Figure 1.9**). Tridacnid giant clam has evolved a very unique photonic system involving micron-scaled forward scatterers (**Figure 1.9a-d**) that spatially distribute the incident sunlight for efficient solar transformation and photosynthesis.[60] The photosymbiotic cells, algae, are densely organized into micro-sized vertical pillars to protect themselves from strong sunlight. The forward scatterers, so-called iridocytes, covering the clam tissue embedded with micropillars can act as lens-like cells scattering more of red and blue wavelengths of light in the forward direction to efficiently feed all algae packed in the micropillars sitting beneath iridocytes, thereby enhancing the photosynthetic reaction of algae. As another example, cephalopods including octopuses, squid, and cuttlefish offer interesting underwater camouflage. Their skin contains chromatophores that appear as barely visible dots when the muscle is in the relaxed state.[61] When exposed to UV light, the skin stretches, the embedded chromatophores expand, exhibiting highly visible red colors. When the external stimuli are removed, the chromatophores become punctate, allowing the skin looks transparent or colorless. The reversible transparency/color changes have attracted many interests to mimic cephalopod skins for color displays, mechano-responsive sensors, and smart window applications.[62-64] Inspired by these optical designs, we have developed several approaches to create highly efficient forward scatters and mechanoresponsive smart windows.[55, 56]

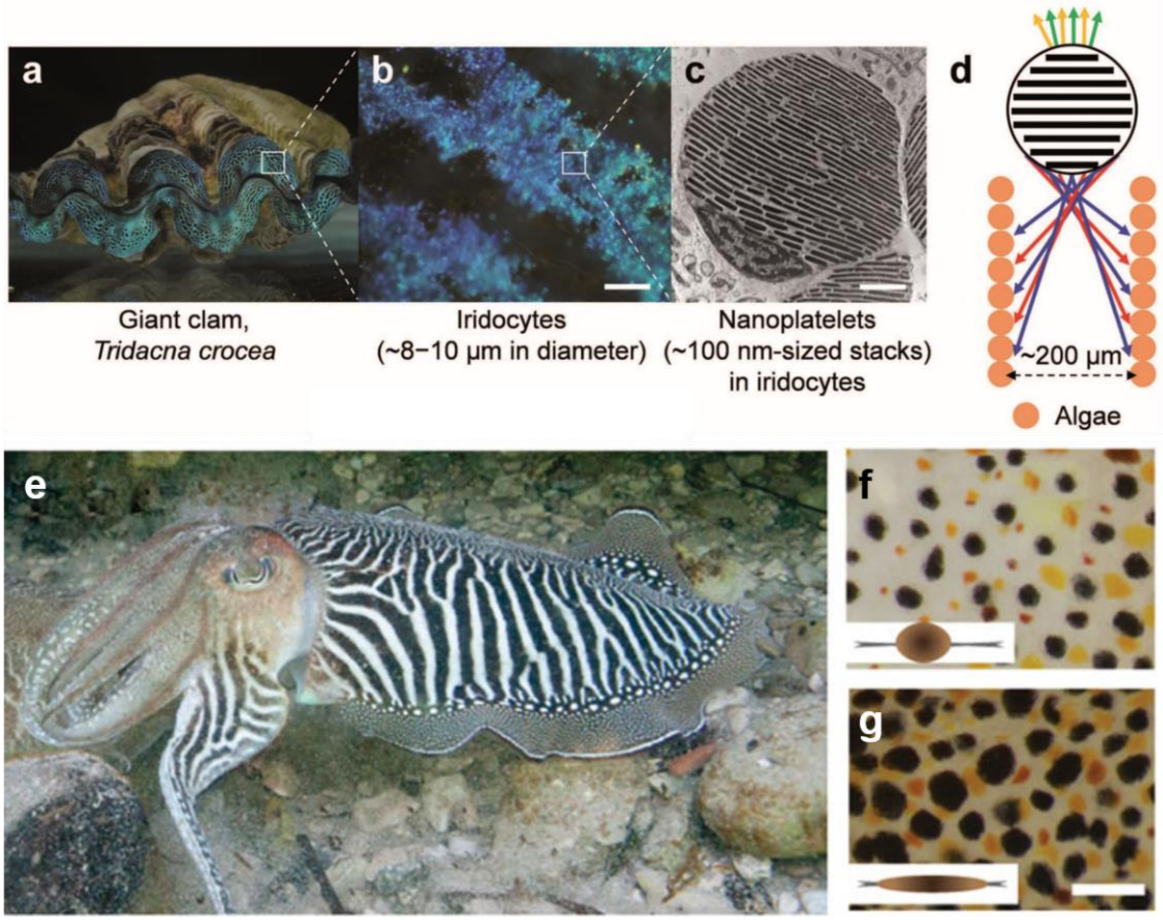

Figure 1.9 Biological creatures with optimized photonic systems. Photograph of giant clam, Tridacna crocea (shell length, ≈6–8 cm) (a), reflected light microscopy image of the clam iridocytes (scale bar: 200 μm) (b), TEM image of the clam iridocyte showing the nanoplatelets (scale bar: 2 μm) (c), and schematic illustration of the scattering behavior from a single iridocyte, which back scatters yellow and green wavelengths while forward-scattering blue and red wavelengths (d). Reproduced with permission from reference [60]. Copyright © 2017, John Wiley and Sons. Skin coloration in cephalopods. Hierarchy of dermal coloration in adult cuttlefish S. officinalis (e). When actuated, dorsal mantle chromatophores transition from a punctate (f) to an expanded (g) state in response to visual cues. Scale bar is 1 mm. Inset is a schematic of a punctate and expanded chromatophore in the plane perpendicular to (f) and (g), respectively. Reproduced with permission from reference [65]. Copyright 2014, The Royal Society Publishing.

Figure 1.10 is the overview of this thesis. We assemble silica NPs into ordered structures with different size, spacing, and microarrays. Then we embed them into polymer media, thereby achieving tunable scattering, reflectance, and transparency that are determined by both the assembly of NPs and the composition of polymer media. In the first part of this thesis, we assemble the constituent NPs into three-dimensional spheres using emulsion-based method. Then, by embedding them into gelatin films, we fabricate light distributing films scattering more of light in forward direction, which can be utilized in photobioreactor applications. In the second part, we use spray coating skills to assemble the nanoparticles into two-dimensional layers over the large area of substrate. By embedding 2D layered particles into stretchable polymers, we fabricate optically switching films and applied them in smart glazing window films.

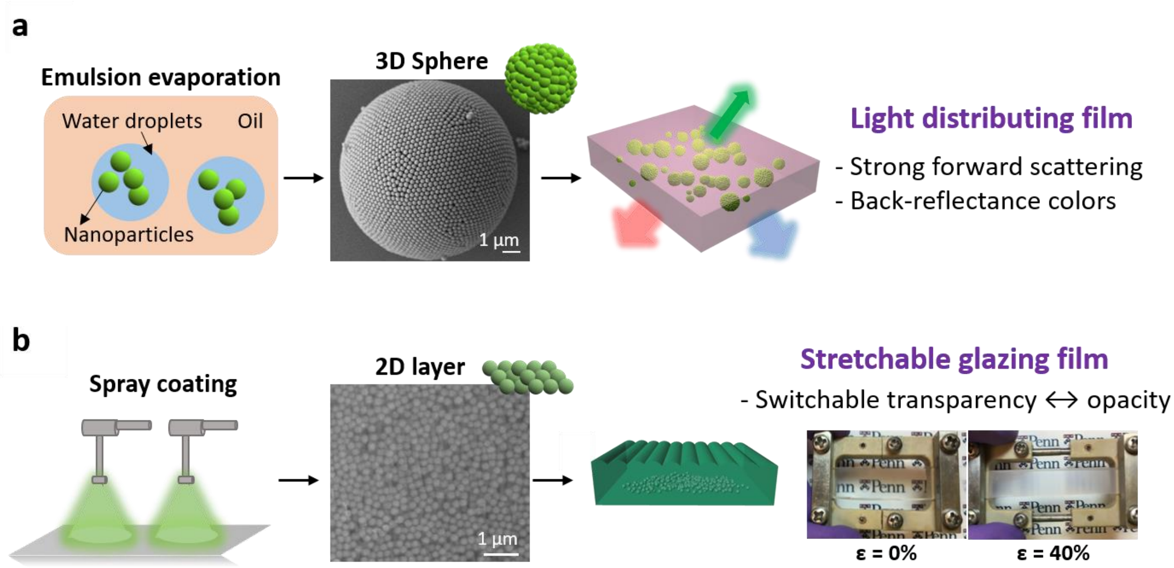

Figure 1.10 Overview of different NP/polymer systems reported in this thesis. (a) The design of forward scatters. Reproduced with permission from reference [60]. Copyright © 2017, John Wiley and Sons. b) The design of mechano-responsive smart windows. Reproduced with permission from reference [55]. Copyright © 2018, John Wiley and Sons.

Since the optical properties of particle-polymer composites can be affected by both the NPs and polymer matrix, either separately or in combination, here, I will briefly review the two separated aspects: 1) varying the size, shape, and chemistry of the NPs and 2) using stimuli-responsive NPs and/or stimuli-responsive polymer matrix. In Section 1.2, I will overview the underlying phenomena of light propagation in structured materials. In Section 1.3, I will discuss different approaches to fabricate multi-scaled structures from particle assembly and their resultant optical properties. In Section 1.4, the developments of stimuli-responsive particle-embedded polymer composites and the resulting tunable optical properties are discussed. In Section 1.5, the outline of this thesis is presented.

1.2 Principles of optical properties in structured materials

The optical properties of structured composite materials are determined by the interaction of incident light with each material component on the structure. For example, structural colors can be generated from the interference of visible light reflected from periodic lattices of high and low refractive index materials, in which the dimension of the lattice constants are on the order of visible wavelength. Depending on the lattice constants, structural symmetry, volume filling fraction, and refractive index contrast of the structured materials, the resulting light scattering, absorption, diffraction, and transmission can be modulated to control the directions and wavelengths of the propagated light,[66] leading to tunable colors, iridescence, and variable transparency or opacity. First, I will briefly review basic principles of optics.

1.2.1. Light scattering

Light scattering is a physical phenomenon where a beam of light is deviated from the original direction of propagation and redirected in many different directions. Unlike reflection, where light is bounced off a surface and deflected in a straight path, light scattering introduced by the interactions with molecules or particles (so-called scatterers) can occur in all directions. The interactions between light and matter can alter the appearance of the objects, which is mostly explained by the two physical processes: light scattering and absorption. Both processes remove energy from a beam of light passing through the medium, thereby attenuating the light intensity, which is called extinction of light.[67] Here we focus on the light scattering process that is governed by the physical interaction of light with structured materials consisting of scatterers and media with specific refractive index pairs, structural regularities, and length scales. The color, haziness, or gloss of structured materials are generated by the light scattering resulting from structural inhomogeneities and refractive index contrasts. For example, the whiteness of surfaces is attributed to the multiple scattering of light by internal or surface irregularity in the structures. Dull and matte colors come from the structures in which micro-scaled irregularities and certain refractive index contrast give rise to diffuse scattering instead of specular reflection. In contrast, the lack of surface scattering results in a glossy and shiny look, as with polished metal.

Scattering phase function, defined as the probability of scattered light at a given angle, is determined by the size of scatterer relative to the wavelength of light as well as the shape and the refractive index of the scatterer. The size parameter, 'x' is defined by the ratio of the characteristic dimension of the scatterer and the wavelength of the scattered light where 'r' is the radius of particle and 'λ' is the wavelength of the light (see Equation 1-1)).

$$x = \frac{2\pi r}{\lambda} \tag{1-1}$$

Light scattering by a particle with a diameter much less than the wavelength ($x \ll 1$) can be explained by Rayleigh scattering. In this case, a random collection of phases generated from randomly dispersed, a small particle governs the direction of scattered light, exhibiting more like isotropic scattering. Mie scattering, on the other hand, is light scattering by a spherical particle with larger diameter (micron-sized). It is responsible for more unselective scattering with wider angular distribution. For example, scattering by water droplets in clouds (diameter of particles: ≈20 μm) can be explained by Mie scattering, where all visible wavelengths are scattered more or less equally.

1.2.2 Mie theory and Mie scattering phase function

Single scattering by a homogeneous sphere of a given size parameter can be explained by the Mie theory, also known as Lorenz-Mie theory. Light scattering by a particle in an absorbing medium, however, cannot be directly explained by Mie theory. For this reason, far-field approximation has been typically used to modify Mie theory and thus to develop a proper theoretical model of light scattering by a particle embedded in an absorbing medium.[68] The angular distribution of scattered light intensity at large distance from the particle at a given wavelength can be represented by Mie scattering phase function.[68] When the angle (θ) between the direction of incoming light and scattered light is larger than π/2 as shown in **Figure 1.11**, it is called backward scattering. If the scattered light has the same direction as that of incident light or if θ is less than π/2, it is referred as forward scattering. This angular distribution of scattering is determined by the two key parameters, size parameter (x) and the refractive index of materials. In Mie scattering, larger particles likely generate more forward scattering than smaller particles do.

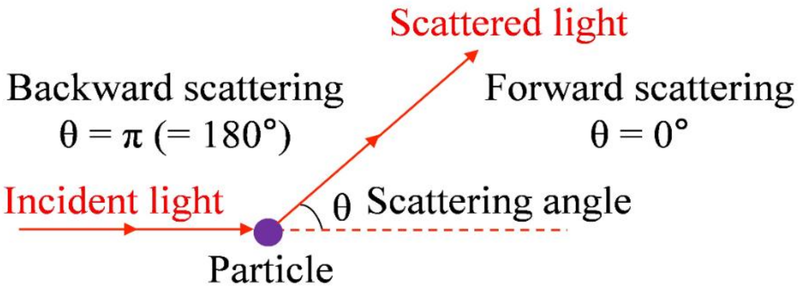

Figure 1.11 Forward and backward scattering of light.

The angular distribution of Mie scattering can be modeled by using Henyey–Greenstein function.[69] In Henyey–Greenstein function, asymmetry factor (‘g’), a mean cosine of the scattering angle, is a parameter showing the preferred scattering direction of light (see Equation 1-2). The angular distribution function, P (θ, g), represents the energy scattered per unit angle in a certain direction to the average energy scattered in all directions as defined as

$$g = \langle \cos(\theta) \rangle = \frac{\int p(u)\cos(u)du}{\int p(u)du} \tag{1-2}$$

$$P(\theta, g) = \frac{1-g^2}{[1+g^2-2g\cos(\theta)]^{\frac{3}{2}}} \tag{1-3}$$

When g approaches +1, more of light is scattered in the forward direction. When g approaches -1, backward scattering is dominant. Scattering with g = 0 is more like the isotropic scattering of light with evenly distributed scattering directions. For the spherical particle with a larger size, g is close to +1, exhibiting strong forward scattering. Based on this analysis, we calculate the optimized forward/backward scattering ratio for the spatial distribution of light in chapter 2.

1.2.3 Diffraction grating effect

Ordered optical structures with the periodicity such as parallel grooves or narrow slits can split and diffract the incident light into many beams with different directions. This periodic optical component acting as the dispersive element is called diffraction grating. The directions of the diffracted light beams are determined by the spacing between the grating units and the wavelength of the incident light. When the length scales of grating units are on the order of the visible wavelength, the sum of the interfering lights from each grating generates structural coloration. Because the phase of each beam varies depending on the optical path length from each slit, either constructive or destructive interference occurs at given wavelengths of light. As shown in **Figure 1.12** (a blazed grafting) and **Figure 1.13 (**a sinusoidal wave grating), the incident light is diffracted into several beams with the maxim incident angle at order m, θ_m. When the angle between the incident light beam and the normal surface is any arbitrary angle, θ_i, the diffraction grating is given by

$$d(sin\,\theta_i - sin\,\theta_m) = m\lambda, \tag{1-4}$$

where d is the period of the grating, λ is the wavelength of the incident light, and $\theta_m(\lambda)$ is the angle of diffraction in the order m.

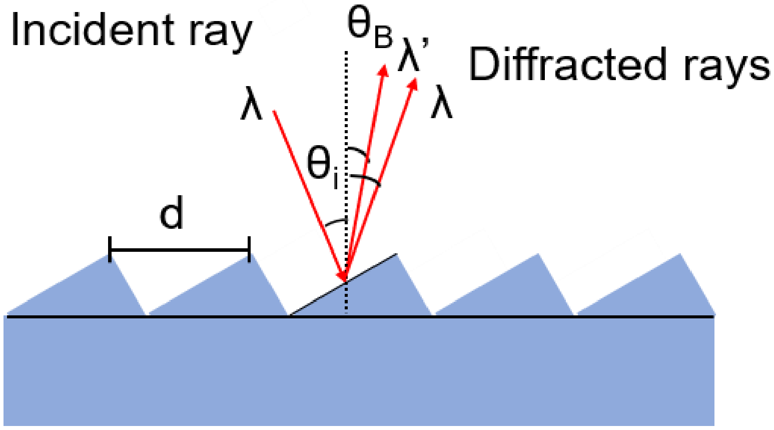

Figure 1.12 Illustration of diffraction from a blazed grating with sawtooth-shaped cross section.

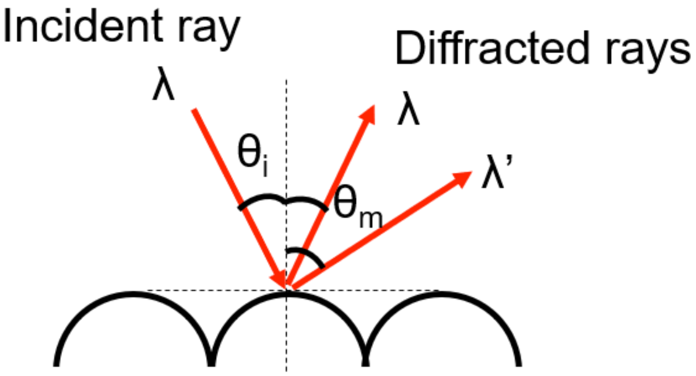

Figure 1.13 Illustration of diffraction from a grating with sinusoidal wave cross-section.

When $m = 0$, the incident beam is reflected from the grating corresponding to the direct specular reflection, referred to the zero order. Light beams diffracted at different angles are represented by non-zero integers, which can be positive or negative. On a highly ordered crystalline lattice, Bragg diffraction occurs when the incident beams are scattered in a specular fashion and undergoes constructive interference from different lattice planes. The difference between the lengths of the two ray paths (d) is proportional to an integer multiple of the wavelength, given by Bragg's law, $n\lambda = 2d\, sin\, \theta$, where θ is the scattering angle. In the case of opals, which are assembled from highly ordered arrays of colloidal particles, the brilliant iridescence is the result of angle-dependent Bragg diffraction in the visible wavelengths.

1.2.4 Thin-film interference

When the incident light arrives at the surface of a thin film, some light rays will be reflected at the top air/film interface at an angle, θ_1, while others will pass through the thin layer and be refracted at the next film/air interface at an angle, θ_2 (see **Figure 1.14**). These two reflected rays will interfere with each other, generating constructive or destructive interference by which the reflection of light is amplified or attenuated. Constructive interference takes place when the difference of the optical path (Case 1 in Figure 1.9),

$$2d\, n_2 \cos\theta_2 = m\lambda, \tag{1-5}$$

where d is the thickness of the film, n_2 is the refractive index of the film.

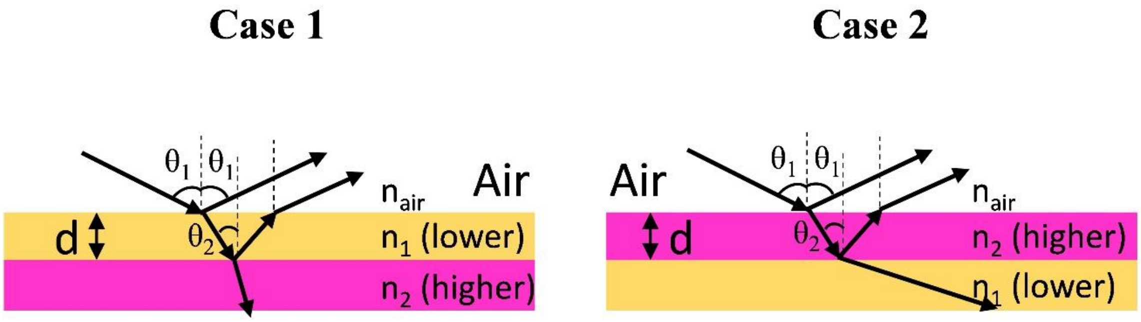

Figure 1.14 Thin film interference in two different systems

Cancellation of reflected waves from each interface occurs when the thickness of the film is an odd multiple of 1/4 λ, reducing the amount of reflected light and enforcing the amount of transmitted light. By this mechanism, the action of camera lenses or antireflection layers coated on glasses and can be explained. On the other hand, oil film has the different system in which the refractive index of material underneath the thin film is lower than that of the thin film. Thus, constructive interference occurs when the wavelength of reflectivity is (Case 2 in Figure 1.9):

$$2n_2d\ cos\ \theta_2(m-\frac{1}{2})\lambda \qquad (1\text{-}6)$$

Accordingly, selected wavelengths of light can be intensified while others are reduced, generating multiple colors.

1.3 Tunable optical properties from ordered nanostructures

Colors in nature, such as those displayed on opals, morpho butterflies,[70] sea shells,[71] soap bubbles,[72] or oil streak on asphalt surfaces, are known as structural colors as a result of light scattering, diffraction, and reflection on structured surfaces with periodicity comparable with visible wavelength of light. As seen in **Figure 1.15**,[73] opals, beetle scales, butterfly wings, and bird plumages have regular arrays of nanostructures with the length scale at a few hundreds of nanometers.[66, 73] The crystalline arrangement of silica (SiO_2) nanospheres in natural opals display angle-dependent, iridescent colors (**Figure 1.15a**). Jewelled Beetles (Chrysina gloriosa) and Pollia condensata fruit display circularly-polarized iridescence (**Figure 1.15b**) attributed to chiral assemblies of chitin (left micrograph) and nanocellulose (right micrograph) fibrils, respectively. In contrast, the scale of Morpho butterfly shown in **Figure 1.15c** is covered with ‘‘Christmas tree-like’’ ridges of different heights, exhibiting angle-independent structural colors. Plumage in the Eastern Bluebird also show uniform blue colors, originated from quasi-ordered β-keratin tubular nanostructures (**Figure 1.15d**). Likewise, peacock feathers (right image in **Figure 1.15d**) have 2D quasi-ordered arrays of melanin rods embedded in keratin, resulting in uniform colors.[73]

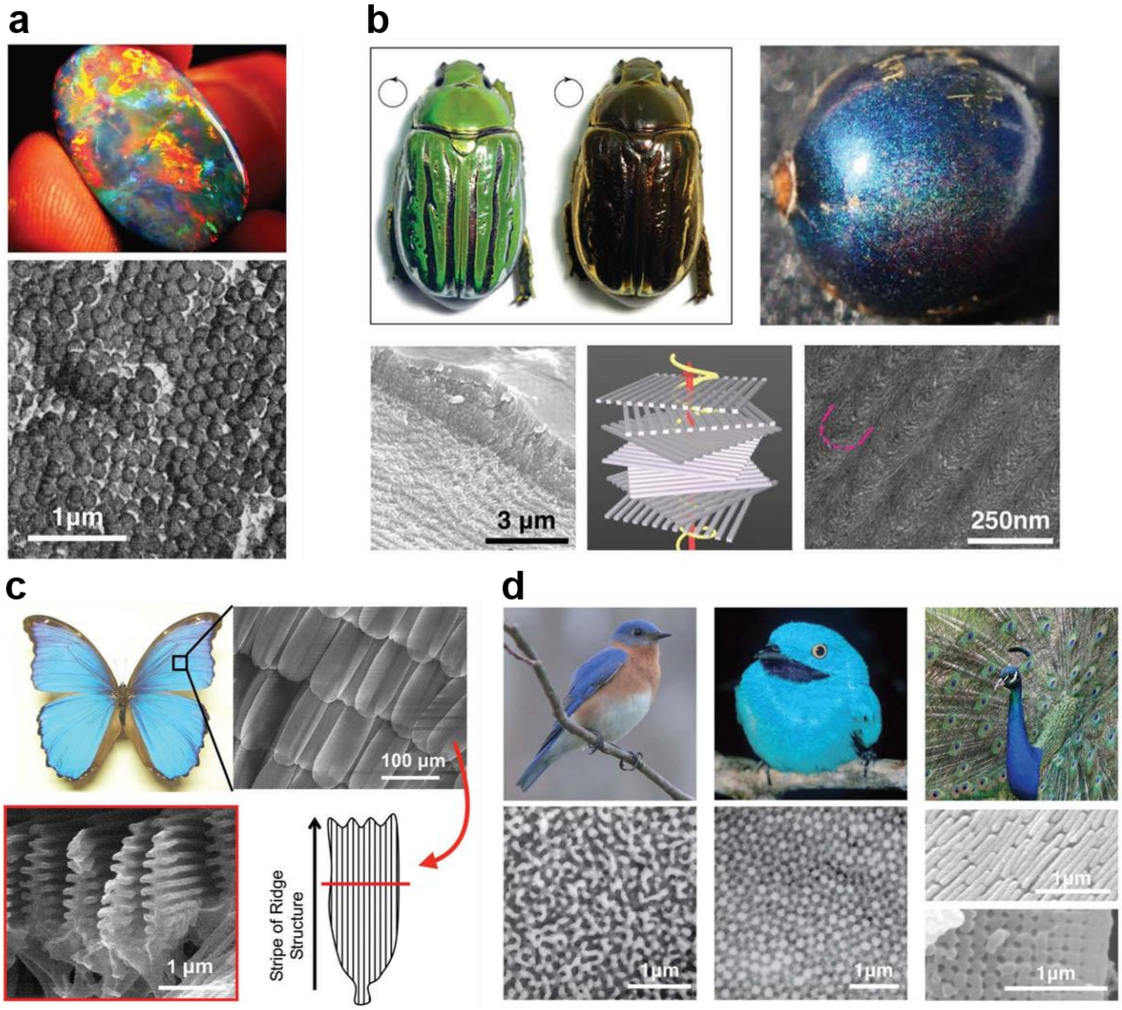
a
1µm
b
3 µm
250nm
c
100 µm
1 µm
Stripe of Ridge Structure
d
1µm
1µm
1µm
1µm

Figure 1.15 Structural colors in nature that have attracted significant biomimicry efforts.[73] Natural opals display iridescent colors because of the crystal arrangement of silica nanospheres (image: wikimedia commons; electron micrograph reproduced with permission from ref. [74], © 1964 Nature Publishing Group) (a). Jewelled Beetles (Chrysina gloriosa) and Pollia condensata fruit display circularly-polarized iridescence as a result of chiral assemblies of chitin (left) and nanocellulose (right) fibrils, respectively (adapted with permission from ref. [75], © 2009 American Association for the Advancement of Science, and from ref. [76], © 2012 National Academy of Sciences, USA) (b). Typical Morpho butterfly (Morpho didius) and SEM images of the scale, each covered with ridges whose lateral profile has the typical ‘‘Christmas tree’’ shape (adapted with permission from ref. [77], © 2006 Copyright Society of Photo Optical Instrumentation Engineers (SPIE)) (c). Structural colors of the plumage in the Eastern Bluebird (Sialia sialis, left) originate from quasi-order b-keratin tubular nanostructures, while in the Plum-throated Cotinga (Cotinga maynana, centre), the structures are spheres (reproduced with permission from ref. [78], © 2009 Royal Society of Chemistry; peacock feathers (right) show 2D arrays of melanin rods embedded in keratin (image of blue peacock Pavo cristatus: wikimedia commons; micrographs reproduced with permission from ref. [79], © 2003 National Academy of Sciences, USA) (d).

Inspired by the bio-photonic structures, researchers have investigated assemblies of synthetic colloids as photonic crystals for telecommunication, sensors, and structural colors.[80] [81-83] The wavelength of diffracted light can be simply changed by varying the particle size and spacing.[84] The colloidal assemblies can also be combined with top-down fabrication approaches to create microparticles consisting of NP arrays. In Section 1.3.1, different kinds of 2D and 3D colloidal crystals are introduced. In Sections 1.3.2 and 1.3.3, confinement of colloidal particles in photonic balls and quasi-amorphous arrays of NPs are introduced.

1.3.1 Colloidal crystals

Photonic crystals consisting of periodically arranged high and low refractive index materials in one dimension (1D), two dimensions (2D), and three dimensions (3D) have attracted much interests to modulate the transmission and reflection of light. Interference of the light scattered from the crystal leads to photonic band gaps (PBGs),[85] where propagation of light of a certain frequency range is completely blocked in 1D, 2D, or 3D. The location and width of the PBGs are determined by periodicity, porosity, and the refractive index contrast between the high and low dielectric materials.[86] The wavelength of light that can be transmitted is determined by the Bragg-Snell's law,

$$\lambda = 2d({n_{eff}}^2 - \cos^2\theta)^{1/2}, \tag{1-7}$$

where d is the lattice spacing, n_{eff} is the effective refractive index of the lattice, θ is the incident angle of light. 3D colloidal crystals can be fabricated via the directed self-assembly of particles driven by physical forces including surface tension,[87] evaporation,[88] and interface interaction.[89] Moreover, external fields such as electric and magnetic fields can also drive the colloidal assembly process. Further, chemical stimuli can give rise to the self-assembly process, changing the surface charge or creating binding sites using DNA functionalization.[90] Colloidal crystals with various geometries can be formed via different fabrication methods. The packing behaviors (e.g. close-packed, non-close-packed, quasi-amorphous arrays) can be manipulated by capillarity, convection, gravity, use of geometrical constraints on the system, or by tuning the surface chemistry of the spheres.[91] For example, fluidic deposition and droplet evaporation can provide the self-assembly process dominated by capillary forces and surface tension. As examples, spreading a dispersion of charged colloidal NPs or using Langmuir-Blodgett (LB) technique allows the self-assembly of NPs in a closely-packed arrays on substrates.[92] While colloidal crystals are typically assembled into face-centered cubic (fcc) structures, body-centered cubic (bcc) or diamond-like structures can also be generated by use of the external stimuli and physical confinement such as dynamic self-assembly in thermotropic LCs. Two common strategies to reconfigure the assembly of NPs are based on applying external stimuli to LC matrix or LC ligands, which results in the formation of body-centered cubic (bcc) lattice.[93] Crystallization of NPs into a diamond-like structure can also be induced by the screened electrostatic self-assembly of oppositely charged, where the each charged NP is surrounded by a layer of counterions.[94]

1.3.2 Photonic balls

Photonic balls[95-97] are colloidal assembly in the emulsion droplets.[98] The light scattered from the curved surface of micro-sized photonic balls can be programmable and angle-dependent based on Mie theory. The photonic balls act as Mie scatterers, of which the wavelength of reflected light and the intensity of scattered light can be determined by the size and shape of constituent particles, the effective refractive index, and the size and geometry of overall micro-structures. These features have attracted much attention as structured materials expanding the potential for specific optical applications, including sensors,[99] magnetically switchable colorants,[100, 101] pigments,[102, 103] and color-coded substrates for biomedical applications.[104, 105]

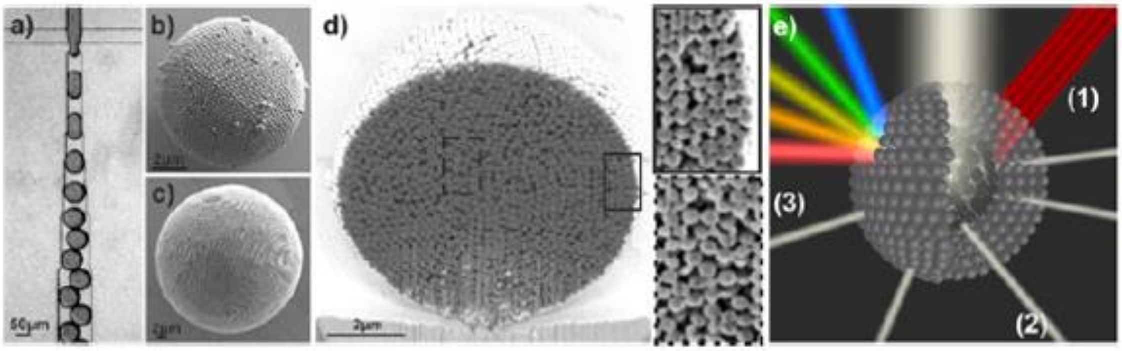

Figure 1.16 Photonic balls fabricated by colloidal self-assembly in a microfluidic device. (a) Optical microscope image of the cross-junction microfluidic device utilized to emulsify a particle-dispersed water phase into monodisperse droplets. (b and c) SEM images of photonic balls consisting of 250 nm-diameter colloidal NPs. The diameter of the photonic ball = 8 µm in b and 30 µm in c. (d) cross-sectional SEM of a photonic ball cut by Focused Ion Beam (FIB). Top Inset shows increasing order of NP assembly toward the air/particle interface. Bottom Inset shows increasing disorder toward the particle center). (e) Schematic illustration of multiple optical behaviors generated from the hierarchical self-assembly (1): Crystalline order results in Bragg reflection of light with a wavelength defined by the size of colloidal particles (2); The disorder in the particle assembly gives rise to unselective scattering of incident light (3); The periodic assembly of particles at the surface leads to grating diffraction effects, splitting white light into its spectral components (for colloid diameter > 400 nm). Reproduced with permission from reference [98].

Photonic balls can be fabricated by assembling colloidal NPs in water-in-oil emulsions, where colloidal NPs dispersed in water phase are emulsified in a continuous oil phase containing stabilizing agent (e.g., non-ionic surfactant) via a droplet-based microfluidic device or simply by agitation. In a microfluidic device, capillary tubes are designed to have an inner tube surrounded by an outer flow. The inner diameter of capillary tubes can be tuned (typically from tens of µm to hundreds of µm) to control the size of resultant emulsion droplets. For smaller particles, when control of size uniformity is not necessary, they can be synthesized simply by emulsion-evaporation method together with agitation.[106]

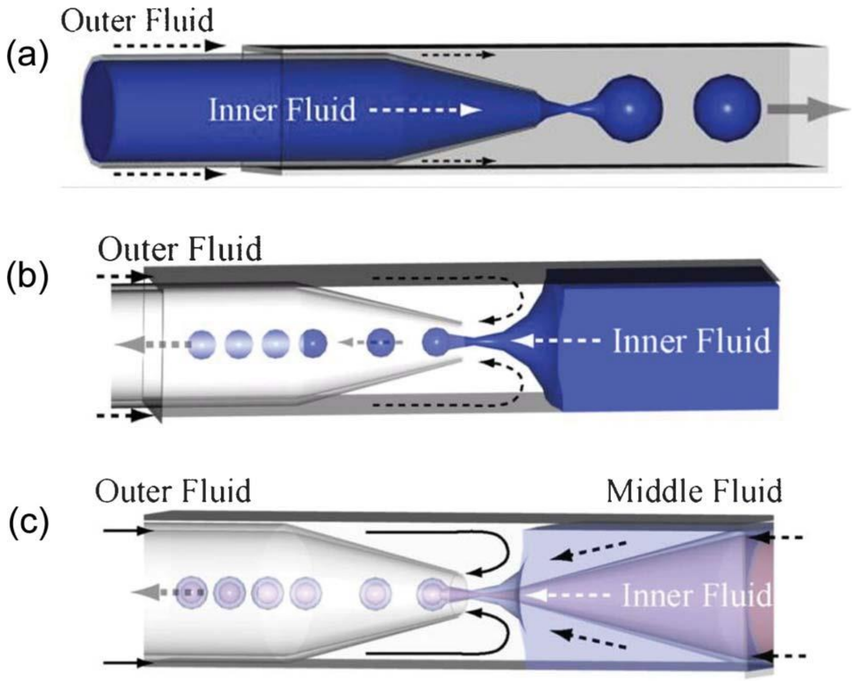

Figure 1.17 Schematic of a co-flow glass capillary device for making single emulsion droplets (a). Arrows indicate the flow direction of fluids and drops. Schematic of a flow-focusing capillary device for making single emulsion droplets (b). Schematic of a double emulsion capillary microfluidic device that combines co-flow and flow focusing (c). Reproduced from Ref. [107] with permission from The Royal Society of Chemistry.

Polydispersed emulsion droplets including small-sized droplets (diameter: 1-10 μm) can be formed in the oil phase while the aqueous particle suspension is emulsified. During the water evaporation step, NPs inside the water droplets slowly aggregate to minimize the surface tension at the water-oil interface. This shrinkage of the emulsion droplets drives the self-assembly of the colloids in their spherical confinement. This emulsion-based method is easy to set up and good for large-scale fabrication. The diameter of the generated photonic balls can be varied from < 10 μm to > 100 μm by tuning the initial concentration of colloids in the water phase and the size of the emulsion droplets.

In **Figure 1.16B** and **Figure 1.16C**, the surface morphologies of the photonic balls show regularly ordered polycrystalline structures with close-packed arrays. The curvature in the spherical confinement impedes the formation of a perfectly ordered crystal, resulting in geometric defects in assembled structures. In **Figure 1.16D**, the internal structure of the photonic ball was characterized by a focused ion beam (FIB) cross-sectioning, indicating a layered crystal structure with ordered arrays around the surface. **Figure 1.16E** shows that this curved crystal structure observed in the photonic balls can exhibit multiple optical properties originated from the multiscale self-assembly:

(1) Bragg reflection of light occurs at specific wavelengths depending on the nano-periodicity given by the size of the colloidal NPs.

(2) Unselective scattering of light is generated from the internal disorder of structures, which induces whitish appearance.

(3) Grating diffraction effects can occur at the surface of balls when the colloid sizes (diameters) are larger than 400 nm, generating a spectrum of colors.[98]

Hence, the color of the photonic balls could be changed from blue to green and then red as the size of colloidal particles varies from 180 nm to 250 nm due to the Bragg reflection of light.[98]

In highly ordered colloidal crystals, Bragg reflection dominates. The resulting structural color is typically angle-dependent, which causes limitation in its applications that require broad viewing angles, such as printed media, architectural skin, displays, optical devices and sensors.[108, 109] To generate uniform colors, less-ordered NPs are introduced. There has been active research in recent years to fabricate coatings with angle-independent structural color. Microcapsules containing amorphous arrays of core-shell colloidal particles have been developed to create "photonic pigments (see **Figure 1.18**),[110] exhibiting angle-independent structural colors.

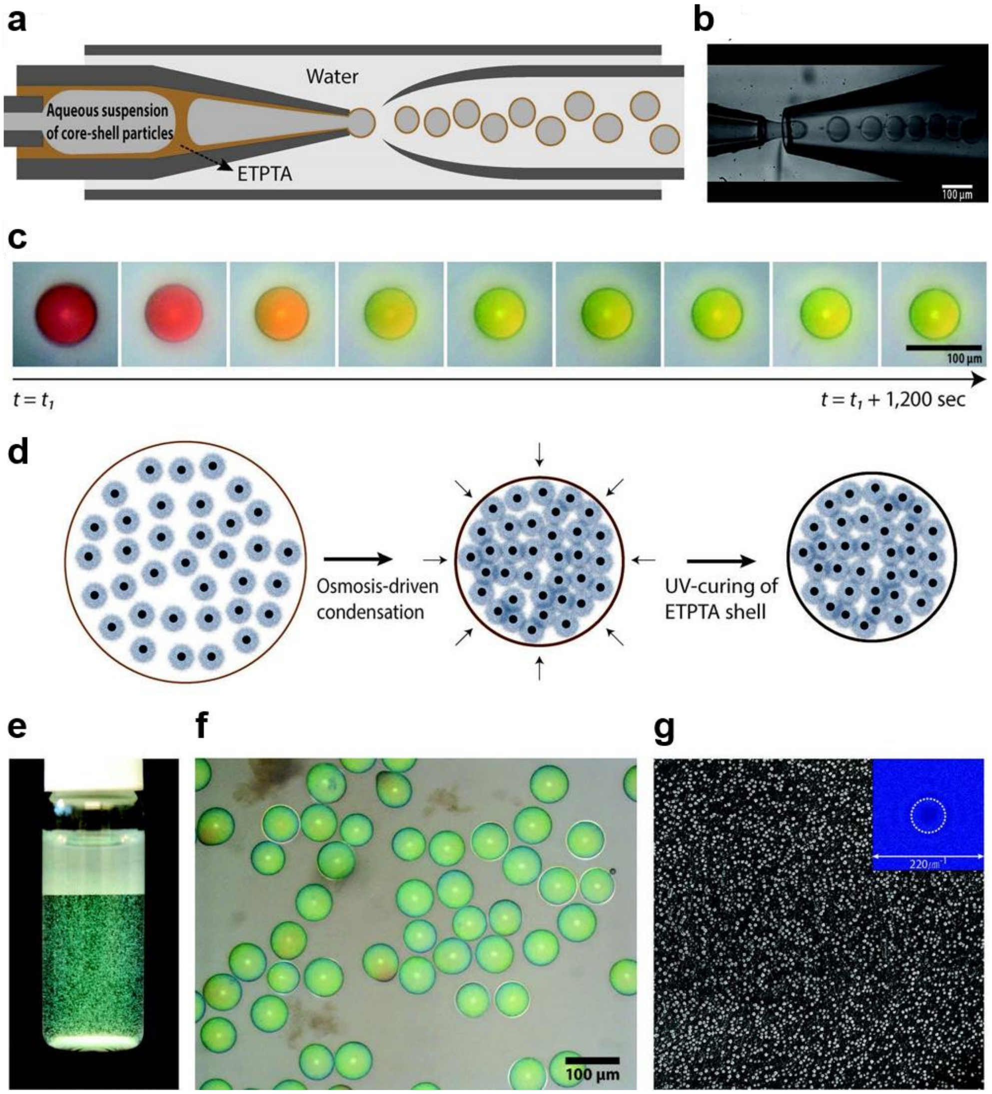

Figure 1.18 Fabrication of quasi-amorphous-structured photonic pigments. a) Schematic of a capillary microfluidic device for the production of water/oil/water double-emulsion droplets with a thin ethoxylated trimethylolpropane triacrylate (ETPTA) membrane. b) Optical micrograph showing generation of uniform water/oil/water droplets. The innermost phase contains an aqueous suspension of core–shell particles with a volume fraction ($f_{core–shell}$) of ca.0.28. c) Time-series optical micrographs of osmosis-driven condensation of droplets at 340 mOsmL^{-1}, where t_1, the elapsed time for microscope analysis, is ca. 5 min. d) Schematic of the structure of particles during osmosis-driven condensation. e,f) A photograph and an optical micrograph of the photonic pigments in water after UV-curing of the ETPTA shell. The sample is compressed at 440 mOsmL^{-1}. A few capsules show yellow spots due to local deformation of the polymer shell. g) Scanning electron micrograph of a cross-section of a cryogenically fractured photonic pigment microcapsule prepared under compression at 440 mOsmL^{-1}. The field of view is 20.0 μm wide. The inset in (g) is the two-dimensional Fourier power spectrum derived from (g). Reproduced with permission from reference [110]. Copyright © 2014, John Wiley and Sons.

1.3.3 Quasi-amorphous array of NPs for angle-independent optical properties

Quasi-amorphous arrays of NPs can be deployed to produce less angle-dependent or angle-independent optical properties. Core-shell NPs with a shell possessing low refractive index have been synthesized to tune the spacing between cores to achieve optimal scattering for non-iridescent colors (**Figure 1.18**). Droplet casting of a mixture of polystyrene NPs, adding electrolyte-like sodium chloride in colloidal solution, and spray coating of colloidal particles dispersed in highly volatile solvents can lead to formation of less-ordered colloidal assemblies. Among them, spray coating of monodispersed colloidal particles has attracted much interest due to its simplicity, low cost, and scalability over a large area on both planar and curved surfaces.[109]

Ge et al. have demonstrated angle-independent full-color films (see **Figure 1.19**) by spray coating monodispersed silica NPs of different sizes (100–340 nm in diameter) dispersed in ethanol or isopropanol. Because the evaporation is fast, quasi-amorphous arrays of NPs are formed on the substrate, leading to angle-independent colors attributed to the combination of constructive interference and Rayleigh scattering. [109]

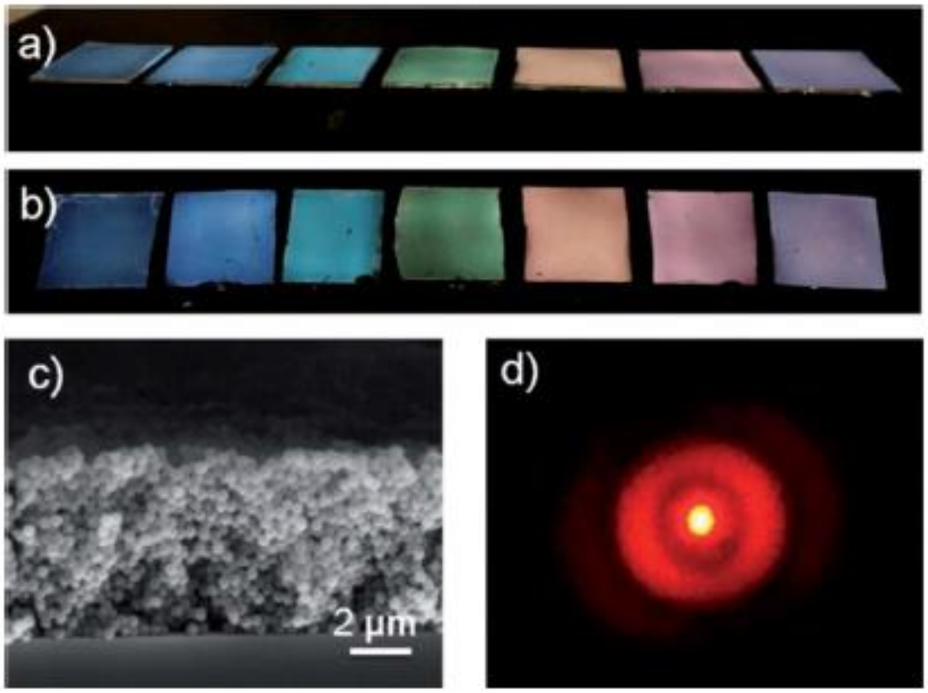

Figure 1.19 Angle-independent colors from the quasi-amorphous array of NPs. (a and b) Optical photographs of different color coatings on glass slides, sprayed from silica NPs with diameters of 100 nm, 185 nm, 230 nm, 255 nm, 290 nm, 310 nm and 340 nm (left to right) on black polypropylene (PP) film with different viewing angles under room lighting. A layer of water was injected in-between the glass slide and the black PP film. The angle between the sample surface and viewing direction was (a) 30° and (b) 70°. (c) SEM image of the magenta coating from 310 nm diameter silica NPs. (d) A diffraction pattern of the magenta coating using a 633 nm He–Ne laser. Reproduced from Ref. [109] with permission from The Royal Society of Chemistry.

1.4 Particle-embedded polymer composites for responsive optical properties

In the previous section, we discuss fine-tuning the optical properties in colloidal assemblies of NPs by control of their arrangement. In this section, we discuss dynamic tuning of the optical properties by embedding simple NPs (e.g. silica) in responsive polymers[111] or use thermochromic or electrochromic NPs.

1.4.1 Thermo-responsive particle-embedded polymer composites

Thermal responsive materials can change their properties, e.g., refractive index or the lattice constant, a function of temperature. A composite gel containing PNIPAAm and plasmonic NPs can generate plasmonic responses based on three kinds of mechanisms: 1) a change in coupling between the NPs according to the change of their distance of separation or 2) a change in the refractive index of the PNIPAAm surrounding the nanoparticle due to the expulsion and the replacement of the water during the volume phase transition or 3) both mechanisms.[112] For example, Karg et al. investigated composite materials consisting of Au nanorods adsorbed on PNIPAAm microgels.[113] In the case of Au nanorod, the plasmon resonance splits into two modes: a longitudinal mode parallel to the long axis of the rod and a transverse mode perpendicular to the that.[114] The thermally induced collapse of the polymer network inside the particles leads to a red shift of the longitudinal plasmon band of the gold rods by modulating the coupling of Au nanorods and neighboring ones.[113] Suzuki et al. investigated Au-NPs-incorporated PNIPAAm microgels with reversibly tunable brilliant colors.[115, 116] In this hybrid structure, the color of the dispersion of the composite microgels were altered when increasing temperature from room temperature to 40 °C.[117] Due to the collapse of the composite microgel above the LCST of PNIPAAm, Au NPs are concentrated, which causes a change in their SPR behaviors such as a red-shift of the absorption peak (from $\lambda = 712$ nm to $\lambda = 784$ nm).[115] Häntzschel and colleagues prepared and modified poly(N-vinylcaprolactam-*co*-glycidyl methacrylate) (PVCL/PGMA) copolymer with photoluminescent europium-doped lanthanum fluoride NPs (LaF3:Eu-AEP) to achieve thermally responsive luminescence in aqueous solution.[118] There have also been various approaches for modifying the thermochromic behavior of PNIPAAm composites for sensing applications.[119] Gotoh et al. investigated thermo-responsive core-shell particles using high-density polymer brushes of thermo-responsive PNIPAAm as shell layers and submicron-sized silica NPs as cores.[120] Here, amorphous arrays of PNIPAAm brush-incorporated silica particles could exhibit angle-independent thermo-responsive properties.[119, 120] The thermo-sensitivity of colloidal photonic crystals could be controlled by embedding photonic crystals in NIPAAm network with different mixing ratio of thermosensitive *N*-isopropylacrylamide (NIPAM) and non-thermosensitive *N*-methylolacrylamide (NMAM).[119, 121]

Vanadium dioxide (VO_2) is an important thermochromic material that undergoes metal-to-insulator transition (MIT) at ~ 68 °C, where a structural transformation from an insulating, low-temperature monoclinic phase VO_2 (M) to a high temperature rutile phase VO_2 (R) occurs, leading to a substantial change in near-infrared (NIR) optical properties.[35] Thus, there have been a variety of strategies for developing VO_2-incorporated polymer composites with thermo-responsive properties for practical light-modulating applications such as sensors, smart windows, displays, and biomedical devices. Especially, VO_2-containing smart window devices have attracted much attention because they can respond to environmental temperature and manipulate NIR irradiation, allowing reversible change of NIR transmittance (from a transparent state at low temperature to a NIR-reflective state at high temperature) responsive to temperature changes while maintaining visible transmittance. Conventionally, VO_2 nanopowders have been commonly spin-coated on glass and thus used in smart window films. Recently, development of a variety of polymer composites embedded with VO_2 has been extensively studied for improving the mechanical/chemical stability of VO_2. VO_2-incorporated polymer composites could provide not only the thermochromic behaviors generated by intrinsic properties of VO_2 NPs but also the increased visible transparency and the infrared modulation ability arises from the nanoscale and interface effects.[35] Gao et al. demonstrated thermo-sensitive and flexible VO_2 nanocomposite foils consisting of VO_2 NPs coated with a silica shell and polyurethane (PU). By coating the VO_2 NPs with a thin SiO_2 shell, they improved the stability of VO_2 NPs, which suppresses unwanted oxidation of VO_2 and thus allows development of transparent, stable and flexible VO_2-based composite films. Their films could provide UV-shielding properties and an excellent temperature-responsive thermochromism in the NIR region.[35] Zhou et. al. developed a novel VO_2-based smart window film by the dispersion of VO_2@SiO_2@TiO_2 core-shell-shell particles in PU.[18] Their smart window combines energy-saving and generation in one device, offering the potential to manipulate and harness solar radiation more efficiently. On the other hand, many approaches for lowering phase transition of VO_2 have been developed mostly by tungsten doping. The inherent phase transition temperature of VO_2 (~68 °C) can be modulated even close to room temperature by doping them with tungsten. For example, Xiao and colleagues developed the films consisting of 1.3 at% tungsten doped VO_2 and demonstrated that the composite films are still able to show efficient transmission modulation of about 26.4% at 2000 nm.[122]

1.4.2 Magnetic-responsive particle-embedded polymer composites

Magnetic NPs made of iron, nickel, and cobalt offer non-invasive, remote control of the heat generation. Therefore, they have potential uses in the biomedical,[123-125] environmental,[126] and optical sensor applications for the detection of antibiotics,[127] detection of cations,[128] and visual inspection of defects.[129] According to their activation modes, there are three categories of magnetic responsive polymer composite materials: 1) Mechanical deformation (film stretched, bent, or rotated) is generated in response to magnetic fields. 2) Particles are pulled to a targeted area guided by magnetic fields, which is particularly interesting for biomedical applications. 3) Magnetic induction or photothermal effect of magnetic NPs can be used to actuate other types of responsive polymer materials, which has attracted much attention for the applications in controlled drug release and shape memory devices.[130]

Ge et al. have fabricated a chloride salt solution-responsive photonic paper by photopolymerizing the mixture of magnetically assembled Fe_3O_4@SiO_2 colloids and poly(ethylene glycol) diacrylate (PEGDA) oligomers. The new type of photonic paper has been prepared through the magnetic field-induced self-assembly of Fe_3O_4@SiO_2 colloids, followed by a simultaneous UV curing process to fix the photonic structures inside the PEGDA matrix. With the salt solution ink, the photonic paper could not only keep its color for a much longer time but also show different color contrasts according to the concentration of the salt in ink. The salt solution could also be used to tune the stop-band of multilayer photonic materials.[131]

Lee et al. demonstrated stimuli-responsive properties under magnetic- and electric-fields, enabling reflective color-changes in a liquid medium by preparing and modifying silica coated-iron oxide core-shell NPs ($Fe_3O_4@SiO_2$) with two different types of silane coupling agents. By mixing surface modified $Fe_3O_4@SiO_2$-F_x (x = 0 and 13) core-shell NPs and a dispersing agent in a low dielectric medium, a responsive magneto- and electro-chromatic ink was prepared. They confirmed the magneto-chromatic/ electro-chromatic stimuli-responsive properties and demonstrated that the hydrophobic surface modified magnetite NPs are promising candidates for reflective display applications.[132]

1.4.3 Mechano-responsive particle-embedded polymer composites

The mechano-chromic materials are of interests as stress-sensors where a low mechanical strain can be visually detected.[119] Mechano-chromic materials can be prepared by embedding assembled colloidal particles in elastomers[56, 119] and hydrogels.[133, 134] We and others have developed particle-embedded polymer composites that can switch optical transparency depending stretching strains.[56]

Bioinspired mechano-chromic composites have been developed from soft and rigid bilayers with low-cost materials (TiO_2, PDMS, PVA, and laponite) [119, 135] to modulate optical properties such as transparency, luminescence, and color-alteration. Strain-responsive structural colored elastomers have been prepared by fixing colloidal crystals in polymer composite matrices.[136] For the colloidal assembly, monodispersed colloidal particles of a cross-linked random copolymer of methyl methacrylate and ethyl acrylate were used. The colloidal crystal film can provide structural colors when it is swollen with ethyl acrylate monomer. For fabrication of the particle-elastomer composite film, the polymer matrix was cured by heating at 60 °C for 24 h. In other cases, metal NPs with a variety of shapes and lattice spacing have been embedded in flexible polymers such as PDMS[137], exhibiting mechano-responsive LSPR which is a surface plasmon from a NP of size comparable to or smaller than the wavelength of light.[138] However, the mechanical robustness of hydrogels or elastomers remains to be improved for practical applications.

1.4.4 Electromechano-responsive particle-embedded polymer composites

Compared to mechanical and magnetic actuation, electric field offers fast switching speeds and good spatial control, and the possibility to couple with the electronic devices.[139, 140] When the electrically responsive particles are embedded in stretchable or deformable elastomers, it is possible to achieve electromechano-responsive properties for sensors and flexible devices. Electro-mechanochemically responsive films have been prepared by using fluorescent patterns under an electric field, or adaptive optoelectronic camouflage systems. For example, Rossiter et al. used an electroactive polymer actuator to mimic the cephalopods' radial expansion/contraction of chromatophores. Wang et al. demonstrated the cephalopod-inspired design of electromechano-chemically responsive elastomers by covalently attaching mechano-chromic molecules (spiropyrans) to PDMS. Under an electrical field, a large deformation of various fluorescent patterns (line, circles, and letters with the size of ≈100 μm) is generated.[141] stretchable transparent electrodes based on graphene[142], polyethylene-dioxythiophene: polystyrene-sulfonate (PEDOT:PSS)[143] or carbon nanotubes (CNTs) [144] have been used as electrochromic materials in mechano-sensitive electronic skins based on flexible polymer substrates, shape memory polymer (SMP) membranes, or stretchable active matrix.[145]

1.4.5 Patterned polymer composites for stimuli-responsive optical properties

Besides colloidal crystals and inverse opals, periodic structures including microhole arrays,[146] micropyramids,[147] wrinkles,[148] or micro-/nanopillar arrays[149, 150] have also been widely exploited for tuning the optical properties.[151-153] By taking advantage of mechanical instability in SMP membranes consisting of a hexagonal array of micron-sized circular holes, our group previously demonstrate color switching via pattern transformation actuated by applied strain.[146] When hot-pressed, the circular holes were deformed to an array of ellipses, and further to featureless as the applied strain increases, therefore, switching the film with diffraction color to a transparent state (see **Figure 1.20**). Upon heating, the SMP remembers the original polymer configuration, therefore, the deformed state can return to recover the original color state.

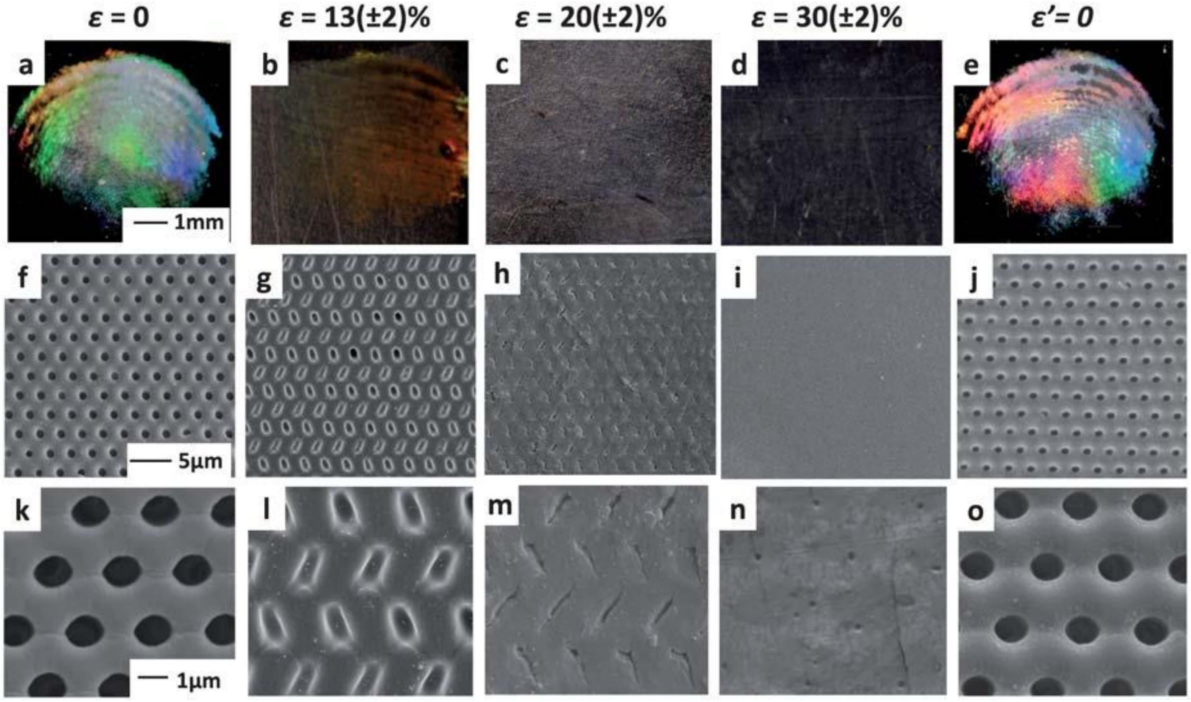

Figure 1.20 Pattern transformation and recovery in a 2D SMP membrane. Optical images of the: original (a); partially deformed, strain (ε) ~13±2% (b) and ε ~20±2% (c); completely deformed, ε ~30±2% (d); and recovered SMP membranes (e). (f–j) Corresponding SEM images of the SMP membranes shown in (a–e). (k–o) Higher magnification SEM images of (f–j). Reproduced from Ref. [146] with permission from The Royal Society of Chemistry.

As another type of deformable patterns, surface wrinkles with different wavelength and amplitude can be created by buckling of a bilayer elastomer with a hard skin layer as a result of mechanical instability. They have been explored for reversible optical properties,[154] adhesion,[155] wetting,[156] for applications including microlens arrays,[153, 157] flexible electronic devices,[158, 159] pressure sensors,[160] and smart windows.[56, 149] For example, Li et al. demonstrated NIR-responsive dynamic wrinkle patterns with reversibility and high sensitivity by embedding CNTs in PDMS . In this composite, the applied strain can be modulated by NIR-induced thermal expansion of the CNT-PDMS substrate, due to the efficient photon-to-thermal energy conversion of CNTs.[148] Therefore, the wrinkle patterns can be generated in situ for dynamic tuning of the surface properties.[148]

1.5 Thesis outline

This thesis considers the design, fabrication, and characterization of particle-embedded polymer composite films that can potentially play an important role in sustainable light-modulating applications.

In the previous designs of particle-polymer composites, they often require precise control of the particle size and shape at the nanoscale, which causes low defect-tolerance in optical devices, making them expensive and not scalable. Thus, it is highly desired to simplify the process and lower the production costs for fabrication of large-area composite films with tunable optical properties. Therefore, here we develop simple ways of fabricating particle-embedded polymer composites by using a cost-effective material, for example, silica NPs. Silica has been widely used in fabricating structural, optical materials because they are chemically stable and commonly found in nature. Spherical colloidal silica of uniform size from 10's nm to 2 μm can be synthesized by the modified Stöber chemistry.[161] Embedding silica NPs in the polymer matrix will also increase the elasticity, mechanical strength, and heat resistance.[162]

Hence, here we use silica NPs and demonstrate optimized optical properties by assembling the NPs in ordered or quasi-ordered structures and/or embedding them in appropriate polymer matrices. In the first part, we develop optimized designs of composite films by assembling silica NPs into micro-sized photonic ball structures and embedding them in refractive-index-optimized media to modulate the scattering, reflectance, and transmittance of light for their potential use in sustainable light-utilizing applications such as photovoltaics and photobioreactors. In the second part, we focus on the stimuli-dependent light scattering and resulting on-demand optical transmittance to be modulated in solar-integrated smart windows. We take advantage of 'mechano-responsive type' composites to produce energy-efficient, mechanically driven smart window films. We embed quasi-ordered arrays of silica NPs into the stretchable polymer, PDMS, to achieve nano-scaled deformation in structural arrays of NPs upon stretching. Then, we decorate strain-dependent micropatterns on the surface of PDMS, thereby obtaining fine-tuned light scattering and reflectance from the micro-scaled geometry and nano-scaled periodicity.

In Chapter 2, we develop multiscale photonic structures inspired by the unique light-distribution systems discovered in Tridacnid giant clams. To mimic the salient forward scattering behavior of micro-scaled scatterers in clams, we designed colored, a semi-transparent light distributing film scattering more of light in the forward direction, which can be utilized in photobioreactor applications. We assemble constituent silica NPs into three-dimensional spheres using an emulsion-based method. Then, by embedding them in gelatin, we fabricate forward scattering film from optimized optical and material designs. Our method is simple yet scalable, cost-effective, and environmentally benign, which inspires new designs for small-footprint and defect-tolerant biofuel applications.

In Chapter 3, we report the optical characterization of synthetic scattering films we developed in Chapter 2. We investigate the light-distributing behavior of the films via test methods including angular distribution of scattering, intra-film radiometry.

In Chapter 4, we design mechano-responsive wrinkled silica NPs-polymer film as smart window films and characterize their switchable and tunable optical transmittance. By using spray coating, we assemble the NPs into two-dimensional layers over the large area of a substrate and, we embed the layered particles at the bottom of stretchable polymers (elastomers). To achieve tunable and controllable optical transmittance, we decorate wrinkling patterns with various geometries on the top surface of polymer film, thereby further controlling the optically switching and applying them in smart window films responsive to the mechanical strain.

In Chapter 5, we design mechano-responsive films with tunable optical transmittance by fabricating wrinkles on the particle-embedded surface of a polymer film. We control the geometries of wrinkles and thus tuned diffraction grating effects from the wrinkles.

The dissertation is summarized in Chapter 6, where the outlook and extension of the current work are discussed.

1.6 References

[1] T. Hasobe, H. Imahori, P. V. Kamat, T. K. Ahn, S. K. Kim, D. Kim, A. Fujimoto, T. Hirakawa, S. Fukuzumi, *Journal of the American Chemical Society* **2005**, 127, 1216.

[2] G. M. Kim, T. Tatsuma, *Sci Rep* **2017**, 7, 10699.

[3] C. Hägglund, B. Kasemo, *Optics Express* **2009**, 17, 11944.

[4] Y. Ke, C. Zhou, Y. Zhou, S. Wang, S. H. Chan, Y. Long, *Adv. Funct. Mater.* **2018**, 28, 1800113.

[5] F. Bella, G. Leftheriotis, G. Griffini, G. Syrrokostas, S. Turri, M. Grätzel, C. Gerbaldi, *Adv. Funct. Mater.* **2015**, 26, 1127.

[6] L. Wu, J. He, W. Shang, T. Deng, J. Gu, H. Su, Q. Liu, W. Zhang, D. Zhang, *Adv. Opt. Mater.* **2015**, 4, 195.

[7] N. G. Khlebtsov, L. A. Dykman, *Journal of Quantitative Spectroscopy and Radiative Transfer* **2010**, 111, 1.

[8] E. Townsend, G. W. Bryant, *Nano Lett.* **2012**, 12, 429.

[9] C. Noguez, *The Journal of Physical Chemistry C* **2007**, 111, 3806.

[10] P. M. Bendix, L. Jauffred, K. Norregaard, L. B. Oddershede, *IEEE Journal of Selected Topics in Quantum Electronics* **2014**, 20, 15.

[11] A. M. Smith, S. Nie, *Analyst* **2004**, 129, 672.

[12] X. Huang, M. A. El-Sayed, *Journal of Advanced Research* **2010**, 1, 13.

[13] D. T. Gillaspie, R. C. Tenent, A. C. Dillon, *Journal of Materials Chemistry* **2010**, 20, 9585.

[14] C. G. Granqvist, *Solar Energy Materials and Solar Cells* **2000**, 60, 201.

[15] T. He, Y. Ma, Y. Cao, X. Hu, H. Liu, G. Zhang, W. Yang, J. Yao, *The Journal of Physical Chemistry B* **2002**, 106, 12670.

[16] A. Kaushal, N. Choudhary, N. Kaur, D. Kaur, *Applied Surface Science* **2011**, 257, 8937.

[17] R. Arezou, H. Ali, N. Abdolrahman, *Journal of Physics D: Applied Physics* **2018**, 51, 375102.

[18] J. Zhou, Y. Gao, Z. Zhang, H. Luo, C. Cao, Z. Chen, L. Dai, X. Liu, *Sci Rep* **2013**, 3, 3029.

[19] O. A. Savchuk, J. J. Carvajal, C. Cascales, J. Massons, M. Aguiló, F. Díaz, *J. Mater. Chem. C* **2016**, 4, 6602.

[20] W. N. Harrington, M. R. Haji, E. I. Galanzha, D. A. Nedosekin, Z. A. Nima, F. Watanabe, A. Ghosh, A. S. Biris, V. P. Zharov, *Sci Rep* **2016**, 6, 36417.

[21] G. Schmidt, M. M. Malwitz, *Current Opinion in Colloid & Interface Science* **2003**, 8, 103.

[22] S. Porel, S. Singh, S. S. Harsha, D. N. Rao, T. Radhakrishnan, *Chemistry of Materials* **2005**, 17, 9.

[23] S. Porel, S. Singh, T. P. Radhakrishnan, *Chemical Communications* **2005**, 2387.

[24] D. K. Avasthi, Y. K. Mishra, D. Kabiraj, N. P. Lalla, J. C. Pivin, *Nanotechnology* **2007**, 18, 125604.

[25] C. M. G. Henríquez, G. d. C. P. Guerra, M. A. S. Vallejos, S. D. R. de la Fuente, M. T. U. Flores, L. M. R. Jimenez, *Journal of Nanostructure in Chemistry* **2014**, 4, 119.

[26] C. Minnai, P. Milani, *Appl. Phys. Lett.* **2015**, 107, 073106.

[27] A. C. Manikas, G. Romeo, A. Papa, P. A. Netti, *Langmuir* **2014**, 30, 3869.

[28] A. Choe, J. Yeom, R. Shanker, M. P. Kim, S. Kang, H. Ko, *NPG Asia Materials* **2018**, 10, 912.

[29] A. Convertino, G. Leo, M. Tamborra, C. Sciancalepore, M. Striccoli, M. L. Curri, A. Agostiano, *Sensors and Actuators B: Chemical* **2007**, 126, 138.

[30] W. Suthabanditpong, C. Takai, M. Fuji, R. Buntem, T. Shirai, *Physical Chemistry Chemical Physics* **2016**, 18, 16293.

[31] O. Polonskyi, M. Drabik, A. Choukourov, D. Slavinska, H. Biederman, *WDS '07 Proceedings of Contributed Papers, Part* **2007**, 3, 100.

[32] J. Lee, V. C. Sundar, J. R. Heine, M. G. Bawendi, K. F. Jensen, *Advanced Materials* **2000**, 12, 1102.

[33] C. Lü, C. Guan, Y. Liu, Y. Cheng, B. Yang, *Chemistry of Materials* **2005**, 17, 2448.

[34] Q. Zhou, Z. Bai, W.-g. Lu, Y. Wang, B. Zou, H. Zhong, *Advanced Materials* **2016**, 28, 9163.

[35] Y. Gao, S. Wang, H. Luo, L. Dai, C. Cao, Y. Liu, Z. Chen, M. Kanehira, *Energy & Environmental Science* **2012**, 5, 6104.

[36] N. A. Fleer, K. E. Pelcher, J. Zou, K. Nieto, L. D. Douglas, D. G. Sellers, S. Banerjee, *ACS Appl. Mater. Interfaces* **2017**, 9, 38887.

[37] S. Yano, K. Kurita, K. Iwata, T. Furukawa, M. Kodomari, *Polymer* **2003**, 44, 3515.

[38] K. Zeranska-Chudek, A. Lapinska, A. Wroblewska, J. Judek, A. Duzynska, M. Pawlowski, A. M. Witowski, M. Zdrojek, *Sci Rep* **2018**, 8, 9132.

[39] D. H. Kim, Y. S. Song, *Carbohydrate Polymers* **2015**, 130, 448.

[40] M. Ghanipour, D. Dorranian, *Journal of Nanomaterials* **2013**, 2013, 2.

[41] H.-H. Jeong, M. Alarcón-Correa, A. G. Mark, K. Son, T.-C. Lee, P. Fischer, *Advanced Science* **2017**, 4, 1700234.

[42] C. Lincheneau, M. Amelia, M. Oszajca, A. Boccia, F. D'Orazi, M. Madrigale, R. Zanoni, R. Mazzaro, L. Ortolani, V. Morandi, S. Silvi, K. Szaciłowski, A. Credi, *J. Mater. Chem. C* **2014**, 2, 2877.

[43] K. R. Deepti, B. Karthikeyan, "Frequency and temperature dependent dielectric properties of CuO-Polyvinyl alcohol polymer films", presented at *2012 International Conference on Emerging Electronics*, 15-17 Dec. 2012, 2012.

[44] V. K. Rao, T. P. Radhakrishnan, *ACS Appl. Mater. Interfaces* **2015**, 7, 12767.

[45] W. Cha, H.-J. Kim, S. Lee, J. Kim, *J. Mater. Chem. C* **2017**, 5, 6667.

[46] L. McKeen, in *The Effect of Sterilization on Plastics and Elastomers (Third Edition)*, (Ed: L. McKeen), William Andrew Publishing, Boston 2012, 169.

[47] W.-C. Liaw, Y.-L. Cheng, Y.-S. Liao, C.-S. Chen, S.-M. Lai, *Polymer journal* **2011**, 43, 249.

[48] H. Divya, L. L. Naik, B. Yogesha, *Int. J. Eng. Res. General Sci* **2016**, 4, 357.

[49] S. Maeda, M. Fujita, N. Idota, K. Matsukawa, Y. Sugahara, *ACS Appl. Mater. Interfaces* **2016**, 8, 34762.

[50] S. Wiederseiner, N. Andreini, G. Epely-Chauvin, C. Ancey, *Experiments in Fluids* **2011**, 50, 1183.

[51] G. HÄNel, *Tellus* **1968**, 20, 371.

[52] T. Higashihara, M. Ueda, *Macromolecules* **2015**, 48, 1915.

[53] A. I. Safonov, V. S. Sulyaeva, N. I. Timoshenko, K. V. Kubrak, S. V. Starinskiy, *Physics Letters A* **2016**, 380, 3919.

[54] R. M. Cole, S. Mahajan, J. J. Baumberg, *Appl. Phys. Lett.* **2009**, 95, 154103.

[55] H.-N. Kim, D. Ge, E. Lee, S. Yang, *Advanced Materials* **2018**, 30, 1803847.

[56] D. Ge, E. Lee, L. Yang, Y. Cho, M. Li, D. S. Gianola, S. Yang, *Advanced Materials* **2015**, 27, 2489.

[57] S. S. Hassouneh, A. E. Daugaard, A. L. Skov, *Macromolecular Materials and Engineering* **2015**, 300, 542.

[58] H. Gehan, L. Fillaud, M. M. Chehimi, J. Aubard, A. Hohenau, N. Felidj, C. Mangeney, *ACS Nano* **2010**, 4, 6491.

[59] A. Choe, J. Yeom, R. Shanker, M. P. Kim, S. Kang, H. Ko, *NPG Asia Materials* **2018**, 10, 912.

[60] H. N. Kim, S. Vahidinia, A. L. Holt, A. M. Sweeney, S. Yang, *Advanced Materials* **2017**, 29, 1702922.

[61] L. M. Mäthger, R. T. Hanlon, *Cell and Tissue Research* **2007**, 329, 179.

[62] *Nature* **2014**, 513, 463.

[63] C. Xu, G. T. Stiubianu, A. A. Gorodetsky, *Science* **2018**, 359, 1495.

[64] L. Phan, R. Kautz, E. M. Leung, K. L. Naughton, Y. Van Dyke, A. A. Gorodetsky, *Chemistry of Materials* **2016**, 28, 6804.

[65] L. F. Deravi, A. P. Magyar, S. P. Sheehy, G. R. R. Bell, L. M. Mäthger, S. L. Senft, T. J. Wardill, W. S. Lane, A. M. Kuzirian, R. T. Hanlon, E. L. Hu, K. K. Parker, *Journal of The Royal Society Interface* **2014**, 11, 20130942.

[66] Y. Zhao, Z. Xie, H. Gu, C. Zhu, Z. Gu, *Chem. Soc. Rev.* **2012**, 41, 3297.

[67] H. C. v. d. Hulst, *Light scattering by small particles*, Wiley, New York : **1957**.

[68] Q. Fu, W. Sun, *Applied Optics* **2001**, 40, 1354.

[69] D. Toublanc, *Applied Optics* **1996**, 35, 3270.

[70] M. A. Giraldo, D. G. Stavenga, *Journal of Comparative Physiology A* **2016**, 202, 381.

[71] P. U. P. A. Gilbert, K. D. Bergmann, C. E. Myers, M. A. Marcus, R. T. DeVol, C.-Y. Sun, A. Z. Blonsky, E. Tamre, J. Zhao, E. A. Karan, N. Tamura, S. Lemer, A. J. Giuffre, G. Giribet, J. M. Eiler, A. H. Knoll, *Earth and Planetary Science Letters* **2017**, 460, 281.

[72] S. M. Doucet, M. G. Meadows, *Journal of The Royal Society Interface* **2009**, 6, S115.

[73] A. G. Dumanli, T. Savin, *Chem. Soc. Rev.* **2016**, 45, 6698.

[74] J. V. Sanders, *Nature* **1964**, 204, 1151.

[75] V. Sharma, M. Crne, J. O. Park, M. Srinivasarao, *Science* **2009**, 325, 449.

[76] S. Vignolini, P. J. Rudall, A. V. Rowland, A. Reed, E. Moyroud, R. B. Faden, J. J. Baumberg, B. J. Glover, U. Steiner, *Proceedings of the National Academy of Sciences* **2012**, 109, 15712.

[77] A. Saito, M. Nakajima, Y. Miyamura, K. Sogo, Y. Ishikawa, Y. Hirai, "Morpho blue reproduced by nanocasting lithography", presented at *SPIE Optics + Photonics*, 2006, 6327, 63270Z

[78] E. R. Dufresne, H. Noh, V. Saranathan, S. G. J. Mochrie, H. Cao, R. O. Prum, *Soft Matter* **2009**, 5, 1792.

[79] J. Zi, X. Yu, Y. Li, X. Hu, C. Xu, X. Wang, X. Liu, R. Fu, *Proceedings of the National Academy of Sciences* **2003**, 100, 12576.

[80] K. Katagiri, Y. Tanaka, K. Uemura, K. Inumaru, T. Seki, Y. Takeoka, *Npg Asia Materials* **2017**, 9, e355.

[81] W. Wang, B. Tang, W. Ma, J. Zhang, B. Ju, S. Zhang, *Journal of the Optical Society of America A* **2015**, 32, 1109.

[82] H. Fudouzi, Y. Xia, *Langmuir* **2003**, 19, 9653.

[83] C. Chen, Z.-Q. Dong, J.-H. Shen, H.-W. Chen, Y.-H. Zhu, Z.-G. Zhu, *ACS Omega* **2018**, 3, 3211.

[84] A. Pucci, R. Bizzarri, G. Ruggeri, *Soft Matter* **2011**, 7, 3689.

[85] G. Liu, L. Zhou, G. Zhang, Y. Li, L. Chai, Q. Fan, J. Shao, *Materials & Design* **2017**, 114, 10.

[86] J. D. Joannopoulos, S. G. Johnson, J. N. Winn, R. D. Meade, *Photonic Crystals: Molding the Flow of Light - Second Edition*, Princeton University Press, **2011**.

[87] R. R. A. Syms, E. M. Yeatman, V. M. Bright, G. M. Whitesides, *Journal of Microelectromechanical Systems* **2003**, 12, 387.

[88] C. J. Brinker, Y. Lu, A. Sellinger, H. Fan, *Advanced Materials* **1999**, 11, 579.

[89] L. Hu, M. Chen, X. Fang, L. Wu, *Chem. Soc. Rev.* **2012**, 41, 1350.

[90] R. van Dommelen, P. Fanzio, L. Sasso, *Advances in Colloid and Interface Science* **2018**, 251, 97.

[91] B. A. Parviz, D. Ryan, G. M. Whitesides, *IEEE Transactions on Advanced Packaging* **2003**, 26, 233.

[92] E.-J. Cabrera, L. M. Jaller, R. Amade, S. M. Portal, E. Pascual, E. Bertran, *Nanoscience and Nanotechnology Letters* **2013**, 5, 41.

[93] M. Bagiński, A. Szmurło, A. Andruszkiewicz, M. Wójcik, W. Lewandowski, *Liquid Crystals* **2016**, 43, 2391.

[94] A. M. Kalsin, M. Fialkowski, M. Paszewski, S. K. Smoukov, K. J. M. Bishop, B. A. Grzybowski, *Science* **2006**, 312, 420.

[95] G. R. Yi, V. N. Manoharan, S. Klein, K. R. Brzezinska, D. J. Pine, F. F. Lange, S. M. Yang, *Advanced Materials* **2002**, 14, 1137.

[96] O. D. Velev, A. M. Lenhoff, E. W. Kaler, *Science* **2000**, 287, 2240.

[97] T. Brugarolas, F. Tu, D. Lee, *Soft Matter* **2013**, 9, 9046.

[98] N. Vogel, S. Utech, G. T. England, T. Shirman, K. R. Phillips, N. Koay, I. B. Burgess, M. Kolle, D. A. Weitz, J. Aizenberg, *Proceedings of the National Academy of Sciences* **2015**, 112, 10845.

[99] Z. Xie, K. Cao, Y. Zhao, L. Bai, H. Gu, H. Xu, Z.-Z. Gu, *Advanced Materials* **2013**, 26, 2413.

[100] Z. Yu, C.-F. Wang, L. Ling, L. Chen, S. Chen, *Angewandte Chemie International Edition* **2012**, 51, 2375.

[101] J. Kim, Y. Song, L. He, H. Kim, H. Lee, W. Park, Y. Yin, S. Kwon, *Small* **2011**, 7, 1163.

[102] S.-H. Kim, S.-J. Jeon, S.-M. Yang, *Journal of the American Chemical Society* **2008**, 130, 6040.

[103] S.-H. Kim, S. Y. Lee, G.-R. Yi, D. J. Pine, S.-M. Yang, *Journal of the American Chemical Society* **2006**, 128, 10897.

[104] X. Zhao, Y. Cao, F. Ito, H.-H. Chen, K. Nagai, Y.-H. Zhao, Z.-Z. Gu, *Angewandte Chemie International Edition* **2006**, 45, 6835.

[105] W. Liu, L. Shang, F. Zheng, J. Lu, J. Qian, Y. Zhao, Z. Gu, *Small* **2013**, 10, 88.

[106] P. Zhu, T. Kong, Z. Kang, X. Tian, L. Wang, *Sci Rep* **2015**, 5, 11102.

[107] W. J. Duncanson, T. Lin, A. R. Abate, S. Seiffert, R. K. Shah, D. A. Weitz, *Lab on a Chip* **2012**, 12, 2135.

[108] K. Chung, S. Yu, C.-J. Heo, J. W. Shim, S.-M. Yang, M. G. Han, H.-S. Lee, Y. Jin, S. Y. Lee, N. Park, J. H. Shin, *Advanced Materials* **2012**, 24, 2375.

[109] D. Ge, L. Yang, G. Wu, S. Yang, *J. Mater. Chem. C* **2014**, 2, 4395.

[110] J.-G. Park, S.-H. Kim, S. Magkiriadou, T. M. Choi, Y.-S. Kim, V. N. Manoharan, *Angewandte Chemie International Edition* **2014**, 53, 2899.

[111] C. G. Schäfer, M. Gallei, J. T. Zahn, J. Engelhardt, G. P. Hellmann, M. Rehahn, *Chemistry of Materials* **2013**, 25, 2309.

[112] F. Han, A. H. Soeriyadi, S. R. C. Vivekchand, J. J. Gooding, *ACS Macro Letters* **2016**, 5, 626.

[113] M. Karg, I. Pastoriza-Santos, J. Pérez-Juste, T. Hellweg, L. M. Liz-Marzán, *Small* **2007**, 3, 1222.

[114] T. A. El-Brolossy, T. Abdallah, M. B. Mohamed, S. Abdallah, K. Easawi, S. Negm, H. Talaat, *The European Physical Journal Special Topics* **2008**, 153, 361.

[115] D. Suzuki, H. Kawaguchi, *Langmuir* **2006**, 22, 3818.

[116] D. Suzuki, H. Kawaguchi, *Colloid and Polymer Science* **2006**, 284, 1443.

[117] H. Kawaguchi, *Polymer International* **2013**, 63, 925.

[118] N. Häntzschel, F. Zhang, F. Eckert, A. Pich, M. A. Winnik, *Langmuir* **2007**, 23, 10793.

[119] G. Isapour, M. Lattuada, *Advanced Materials* **2018**, 30, 1707069.

[120] Y. Gotoh, H. Suzuki, N. Kumano, T. Seki, K. Katagiri, Y. Takeoka, *New Journal of Chemistry* **2012**, 36, 2171.

[121] H. Sugiyama, T. Sawada, H. Yano, T. Kanai, *J. Mater. Chem. C* **2013**, 1, 6103.

[122] X. Xiao, H. Zhang, G. Chai, Y. Sun, T. Yang, H. Cheng, L. Chen, L. Miao, G. Xu, *Materials Research Bulletin* **2014**, 51, 6.

[123] M. Arruebo, R. Fernández-Pacheco, M. R. Ibarra, J. Santamaría, *Nano Today* **2007**, 2, 22.

[124] N. Tran, T. J. Webster, *Journal of Materials Chemistry* **2010**, 20, 8760.

[125] S. Moraes Silva, R. Tavallaie, L. Sandiford, R. D. Tilley, J. J. Gooding, *Chemical Communications* **2016**, 52, 7528.

[126] L. Mohammed, H. G. Gomaa, D. Ragab, J. Zhu, *Particuology* **2017**, 30, 1.

[127] C. Cristea, M. Tertis, R. Galatus, *Nanomaterials* **2017**, 7, 119.

[128] V. Mahendran, J. Philip, *Appl. Phys. Lett.* **2013**, 102, 063107.

[129] V. Mahendran, J. Philip, *Appl. Phys. Lett.* **2012**, 100, 073104.

[130] J. Thévenot, H. Oliveira, O. Sandre, S. Lecommandoux, *Chem. Soc. Rev.* **2013**, 42, 7099.

[131] J. Ge, J. Goebl, L. He, Z. Lu, Y. Yin, *Advanced Materials* **2009**, 21, 4259.

[132] S. Lee, J. Y. Kim, S. Cheon, S. Kim, D. Kim, H. Ryu, *RSC Advances* **2017**, 7, 6988.

[133] X. Du, T. Li, L. Li, Z. Zhang, T. Wu, *J. Mater. Chem. C* **2015**, 3, 3542.

[134] G. H. Lee, T. M. Choi, B. Kim, S. H. Han, J. M. Lee, S.-H. Kim, *ACS Nano* **2017**, 11, 11350.

[135] S. Zeng, D. Zhang, W. Huang, Z. Wang, S. G. Freire, X. Yu, A. T. Smith, E. Y. Huang, H. Nguon, L. Sun, *Nat. Commun.* **2016**, 7, 11802.

[136] T. Ito, C. Katsura, H. Sugimoto, E. Nakanishi, K. Inomata, *Langmuir* **2013**, 29, 13951.

[137] J.-H. Choi, Y.-S. No, J.-P. So, J. M. Lee, K.-H. Kim, M.-S. Hwang, S.-H. Kwon, H.-G. Park, *Nat. Commun.* **2016**, 7, 11569.

[138] L.-S. Fu, W.-S. Wang, C.-Y. Xu, Y. Li, L. Zhen, *Sci Rep* **2017**, 7, 1676.

[139] E. L. Runnerstrom, A. Llordés, S. D. Lounis, D. J. Milliron, *Chemical Communications* **2014**, 50, 10555.

[140] Q. Liu, Z. Xu, W. Qiu, C. Hou, Y. Wang, P. Yao, R. Yu, W. Guo, X. Y. Liu, *RSC Advances* **2018**, 8, 18690.

[141] Q. Wang, G. R. Gossweiler, S. L. Craig, X. Zhao, *Nat. Commun.* **2014**, 5, 4899.

[142] T.-H. Han, Y. Lee, M.-R. Choi, S.-H. Woo, S.-H. Bae, B. H. Hong, J.-H. Ahn, T.-W. Lee, *Nature Photonics* **2012**, 6, 105.

[143] M. S. White, M. Kaltenbrunner, E. D. Głowacki, K. Gutnichenko, G. Kettlgruber, I. Graz, S. Aazou, C. Ulbricht, D. A. M. Egbe, M. C. Miron, Z. Major, M. C. Scharber, T. Sekitani, T. Someya, S. Bauer, N. S. Sariciftci, *Nature Photonics* **2013**, 7, 811.

[144] M. K. Shin, J. Oh, M. Lima, M. E. Kozlov, S. J. Kim, R. H. Baughman, *Advanced Materials* **2010**, 22, 2663.

[145] C. Larson, B. Peele, S. Li, S. Robinson, M. Totaro, L. Beccai, B. Mazzolai, R. Shepherd, *Science* **2016**, 351, 1071+.

[146] J. Li, J. Shim, J. Deng, J. T. B. Overvelde, X. Zhu, K. Bertoldi, S. Yang, *Soft Matter* **2012**, 8, 10322.

[147] Z. Xu, X. Wang, K. Han, S. Li, G. L. Liu, *Journal of the Optical Society of America A* **2013**, 30, 2466.

[148] F. Li, H. Hou, J. Yin, X. Jiang, *Science Advances* **2018**, 4, eaar5762

[149] E. Lee, M. Zhang, Y. Cho, Y. Cui, J. Van der Spiegel, N. Engheta, S. Yang, *Advanced Materials* **2014**, 26, 4127.

[150] S. G. Lee, D. Y. Lee, H. S. Lim, D. H. Lee, S. Lee, K. Cho, *Advanced Materials* **2010**, 22, 5013.

[151] B. Grzybowski, D. Qin, R. Haag, G. M. Whitesides, *Sensors and Actuators A: Physical* **2000**, 86, 81.

[152] F. Fu, Z. Chen, Z. Zhao, H. Wang, L. Shang, Z. Gu, Y. Zhao, *Proceedings of the National Academy of Sciences* **2017**, 114, 5900.

[153] Z. Li, J. Xiao, *Extreme Mechanics Letters* **2015**, 4, 118.

[154] P. Kim, Y. Hu, J. Alvarenga, M. Kolle, Z. Suo, J. Aizenberg, *Adv. Opt. Mater.* **2013**, 1, 381.

[155] P.-C. Lin, S. Vajpayee, A. Jagota, C.-Y. Hui, S. Yang, *Soft Matter* **2008**, 4, 1830.

[156] P.-C. Lin, S. Yang, *Soft Matter* **2009**, 5, 1011.

[157] D. Chandra, S. Yang, P.-C. Lin, *Appl. Phys. Lett.* **2007**, 91, 251912.

[158] J. Tang, H. Guo, M. Zhao, J. Yang, D. Tsoukalas, B. Zhang, J. Liu, C. Xue, W. Zhang, *Sci Rep* **2015**, 5, 16527.

[159] H. Guo, J. Tang, M. Zhao, W. Zhang, J. Yang, B. Zhang, X. Chou, J. Liu, C. Xue, W. Zhang, *Nanoscale Res. Lett.* **2016**, 11, 112.

[160] J. Cui, B. Zhang, J. Duan, H. Guo, J. Tang, *Sensors* **2016**, 16, 2131.

[161] K. Nozawa, H. Gailhanou, L. Raison, P. Panizza, H. Ushiki, E. Sellier, J. P. Delville, M. H. Delville, *Langmuir* **2005**, 21, 1516.

[162] T. Ribeiro, C. Baleizão, P. J. Farinha, *Materials* **2014**, 7, 3881.

CHAPTER 2. Bio-inspired design and fabrication of forward scattering composite films embedded with multiscale particles for optimally efficient solar transformers

Adapted from:

Kim, H.-N., Vahidinia, S., Holt, A. L., Sweeney, A. M.*, and Yang, S.* (2017), Geometric Design of Scalable Forward-Scatterers for Optimally Efficient Solar Transformers. Adv. Mater., 2017, 29, 1702922.[1] Reproduced with permission.

2.1 Introduction

Solar energy is the most abundant energy source on earth, and also the ultimate source of all hydrocarbon fossil fuels that are currently the major source of energy in human economies. Accordingly, contemporary solar energy can also be utilized to produce other modes of renewable energy.[2, 3] Therefore, there has been significant effort to develop various solar harvesting materials, devices and concepts,[4] including photovoltaics,[4-9] solar-integrated architectural designs,[10] and artificial photosynthetic cells for chemical and biofuel production.[11, 12] Photobioreactors, or closed, engineered systems for growing lipid-rich algae, use solar energy to create biofuel via photosynthesis, with no requirement for additional reagents such as sugar or lipids.[13] Despite many attempts to engineer photobioreactors,[2, 14, 15] one of the major hurdles of this technology in practice is the poor efficiency of utilizing direct incoming solar flux: algae at the surface of the system must have small absorption cross-sections and utilize non-photochemical mechanisms to quench light to avoid photodamage, while the growth of cells deep in the system is light-limited.[16]

The greater the potential solar resource present in a given location, the more severe this fundamental obstacle to efficient resource utilization in these systems becomes.

What if it were possible to deliver equal, optimally efficient “doses” of sunlight to all the cells in a photobioreactor system, while simultaneously using all the solar radiance available in the environment for photochemistry? Such a strategy would amount to a "solar transformer", loosely analogous to an electromagnetic transformer in the electrical grid distribution system. In previous attempts to realize similar strategies of “dosing” the amount of light per algal cell via “light dilution”, investigators have designed waveguides that direct light deep into the background of culture,[14] and used monochromatic light to reduce photoinhibition and increase photosynthetic efficiency of microalgae.[17] These attempts manage to reduce the amount of light reaching each cell, avoiding photodamage, but in general, disregard how efficiently the solar resource is utilized as a whole. Another class of earlier material strategy for light dilution involves making particles for forward-scattering and/or non-uniform microstructures for uniform surface scattering. These efforts include plasmonic nanoparticles,[18] core-shell nanoparticles,[19] and ellipsoidal dielectric nanoparticles.[20, 21] However, these approaches require top-down fabrication, precise control of the particle size and shape in the nanoscale, and use of high refractive index materials. Thus, they are expensive and not scalable for production and implementation in biofuel reactors. Furthermore, little is known about their wavelength selectivity, optical loss, or uniformity of illumination of a deep channel.

2.2 Optimized photonic system in giant clams

Giant clams are evolved photobioreactors, in that they harbor photosynthetic dinoflagellate symbionts (*Symbiodinium*) that transfer solar energy to the clam via small sugars diffusing from the algae into the clam tissue.[22] These clams do this with optically active cells called "iridocytes" at the surface of their mantle tissue.[23] We previously have shown that the clams organize *Symbiodinium* algae into micropillars with a layer of iridocytes over the surface; the iridocytes function to deliver controlled doses of light to individual cells within the system of algal pillars, as outlined above (see **Figure 2.1**).[24] The giant clams exhibit a near-constant intensity of illumination along the vertical algal pillars of ≈85 μmol quanta $m^{-2}s^{-1}$, which is just under the flux at which nonphotochemical quenching mechanisms are stimulated in *Symbiodinium* (≈100 μmol quanta $m^{-2}s^{-1}$).

Iridocytes are roughly spherical cells (average diameter, 8–10 μm, **Figure 2.1c**) containing stacks of proteinaceous, high-refractive-index 100-nm-thick platelets ($n \approx 1.55$) separated by ~100-nm-thick low-refractive-index cytoplasm ($n \approx 1.33$). Although they can be visually striking, their evolved role within the photosymbiosis is visually inconspicuous: they function to forward-scatter photosynthetically efficient blue and red light into a 15°-wide cone directed along the long axis of the algal micropillars. This cone evenly illuminates the vertical sides of the micropillars, delivering an equal "dose" of sunlight to each algal cell within (see schematic in **Figure 2.1d**), thereby creating a complex surface, rather than a simple plane, for exposing the algal cells to sunlight. The spatial distribution and aspect ratio of the absorbing pillars is such that absorbance of the system is near 100%, while each cell within the system is individually absorbing at a similar flux that allows near-quantum efficiency of photochemistry. Reproducing these properties in devices and materials would provide a new micron-scaled paradigm for small-footprint, defect-tolerant photovoltaics, and for unstirred, evenly illuminated biofuel algal culture.[25, 26]

2.3 Experimental methods

2.3.1 Discrete dipole approximation (DDA) calculation

Target objects are constructed from a lattice of polarizable dipoles with size smaller than a wavelength (λ) so that the target mimics a homogeneous dielectric material. The dipole polarizability can be adjusted to represent the complex refractive indices (m) of different materials, and hence targets can be heterogeneous in composition and designed with internal structure. The dipole size is restricted by the criterion $mkd < 1$, where $k = 2\pi r/\lambda$ is the wavenumber and d is the dipole spacing so that the optical path length $2\pi md$ is less than the wavelength and the dipoles act as point scatterers. We modeled synthetic iridocytes by constructing a cluster of hexagonally packed NPs with a radius r placed within a spherical envelope of size R representing the overall size of the iridocyte cell. The NP cluster is then populated with a lattice of individual polarizable dipoles with size as stipulated by the criterion above and polarizability set to represent the refractive index of desired materials. In the case of targets embedded in a medium, the refractive index is defined relative to the refractive index of the medium (n_{medium}) and to simulate the clam iridocyte environment the relative indices ($n/n_{medium} = 1.17$) was used. Experimentally, the gelatin films containing the microbeads were tuned close to the clam environment refractive index value as discussed in section 2.3. The total number of dipoles (N_d) is defined by the effective size of an equivalent mass sphere a_{eff} as defined in DDA such that $N_d = (4\pi/3)\ (a_{eff}/d)^3$ and $a_{eff} = N_m\ (4\pi r^3/3)$, where N_m is the number of NPs. The filling factor of the cluster is defined as ff = (a_{eff}/R^3), which is approximately 0.7–0.74 for the hexagonally packed clusters we generated. For the calculation of scattered radiation, the target is illuminated by a plane wave, and the response of all dipoles within the target to the incident beam and to all other dipoles is calculated iteratively until convergence is obtained. The scattered intensity as a function of scattering angle and planes are obtained from DDA and normalized to the calculated phase function. The DDA generated composite structures were run for a range of sizes (diameter = 5 μm, 7 μm, and 8.8 μm) and wavelengths (299 nm–900 nm).

2.3.2 Preparation of composite particles

Silica NPs (density = 2.1–2.2 g/cm^3) with various sizes (diameter = 120 nm, 200 nm, 250 nm, and 300 nm, respectively) were purchased from General Engineering & Research (San Diego, CA, USA) and dispersed in deionized (DI) water (32–35 wt%) in a sonication bath for 1 h. For the water-in-oil emulsion system, the outer oil phase was prepared by adding a non-ionic polymeric surfactant, Hypermer™ 2296 (1 wt%) (kindly supplied by Croda, New Castle, DE, USA), to hexadecane (ReagentPlus, 99%, Sigma-Aldrich). 200 μL of pre-dispersed silica NPs aqueous solution was added dropwise to 3 mL of the oil phase. The water-in-oil emulsion droplets were prepared by vigorously shaking the mixture on a vortex mixer (Type 16700 Mixer, Thermolyne) for 30 min and then poured into a custom-built Teflon bath (inner diameter = 7.4 cm, height = 2.5 cm), followed by drying in an oven at 65 °C for 20 h. The resultant hierarchical composite particles appeared in various colors (white, blue, green, and red) in hexadecane depending on the size of the constituent silica NPs. After rinsing the emulsion with hexane three times, the remaining hexane was removed under vacuum in a desiccator for 15 min. The average size of the composite particles could be controlled by the vortexing time and the initial concentration of NPs in the water phase. To improve the robustness of the particles for the subsequent manipulations, they were sintered in a porcelain evaporating dish at 700 °C for 3 h.

2.3.3 Preparation of synthetic iridocytes films and silica NPs embedded in gelatin films

In a typical experiment, the sintered composite microparticles (0.001 g) were added to DI water (2 mL), followed by addition of gelatin powder (0.179 g) (Knox® Gelatine). The weight percent of the composite microparticles in gelatin film was maintained consistent for all single-scattering samples. We estimated the number of the composite particles embedded at a 1mm-distance in gelatin films as 1–2. For multiple synthetic iridocytes film, 0.06 g of the composite particles were used. The mixture was then heated in an oven at 65 °C for 30 min to melt the gelatin. This procedure did not result in appreciable aggregation of the particles, as confirmed by an inspection of the samples under an optical microscope. After removing air bubbles, we cast the mixture (250 μL) on a flat polydimethylsiloxane (PDMS) (Sylgard 184 Elastomer Kit, Dow Corning Corp. Midland, MI) substrate, which was prepared by mixing the prepolymer with the curing agent in 10:1 weight ratio and poured into the petri dish, followed by curing at 65 °C for 4 h. Using a glass slide (2 mm thick) as the spacer and another PDMS flat film as the top substrate, the mixture was sandwiched and gelled at room temperature. 30 min later, the two PDMS substrates were carefully detached from the gelatin film. To create a film sample of standard geometry, we punched the composite particles-embedded gelatin film with a glass pipette in a diameter of 5 mm.

To test whether the optical properties of these films was due to the presence of silica NPs alone, or their aggregates, we also prepared gelatin films embedded with the same amount of dispersed silica NPs. The weight percent of silica NPs in gelatin film was the same as that in synthetic iridocytes films and was maintained constant for all samples. These films were prepared as above, with the additional step of pre-dispersing the silica NPs in water by sonication for 1 h prior to mixing with gelatin.

2.3.4 Characterization

The colors of the synthetic iridocyte films were observed under the Olympus BX61 motorized optical microscope with white light using CellSens software. FEI Quanta 600 Environmental Scanning Electron Microscope (ESEM), JEOL 7500F Scanning Electron Microscope (SEM), and FEI Strata DB235 Focus Ion Beam (FIB) were used in 20 kV, 5 kV, and 10 kV, respectively, to characterize the morphology and the inner structure of composite silica particles and dispersed silica NPs embedded in gelatin film. Humidity in ESEM was maintained at 70% to observe the cross-sectional morphology of synthetic iridocyte films in still-hydrated gelatin.

2.4 Clam-mimicked design and fabrication of synthetic iridocytes

To realize the photonic properties of this solar transformer strategy in a synthetic material, we designed and fabricated synthetic iridocytes by embedding micron-sized “composite particles” assembled from silica NPs in lower refractive index gelatin film (**Figure 2.1e-f**). There have been attempts to create microspheres with internal lamellar morphology via evaporation-induced co-assembly of diblock copolymers with surfactants or triblock copolymers confined in oil-in-water droplets.[27, 28] However, particles prepared in this manner are either too small (on the order of 100’s nm in diameter) or too large (> 20 µm in diameter) in comparison with the clam iridocytes. Similarly, the size of the lamellae formed from block copolymers are typically on the order of 10 nm, and upon solvent evaporation, the particles tend to collapse. Another common strategy to create microspheres is by microfluidic technology.[29, 30] Indeed, micron-sized colloidal assemblies (typically in the range of 10s–100s µm) have been fabricated by microfluidic devices and used to explore the Bragg-like backscattering resulting from the ordered nanostructures for structural color and biosensing.[29, 31, 32] None of these studies investigated forward scattering from these particles, or the resulting redistribution of light for potential applications in photobioreactors.

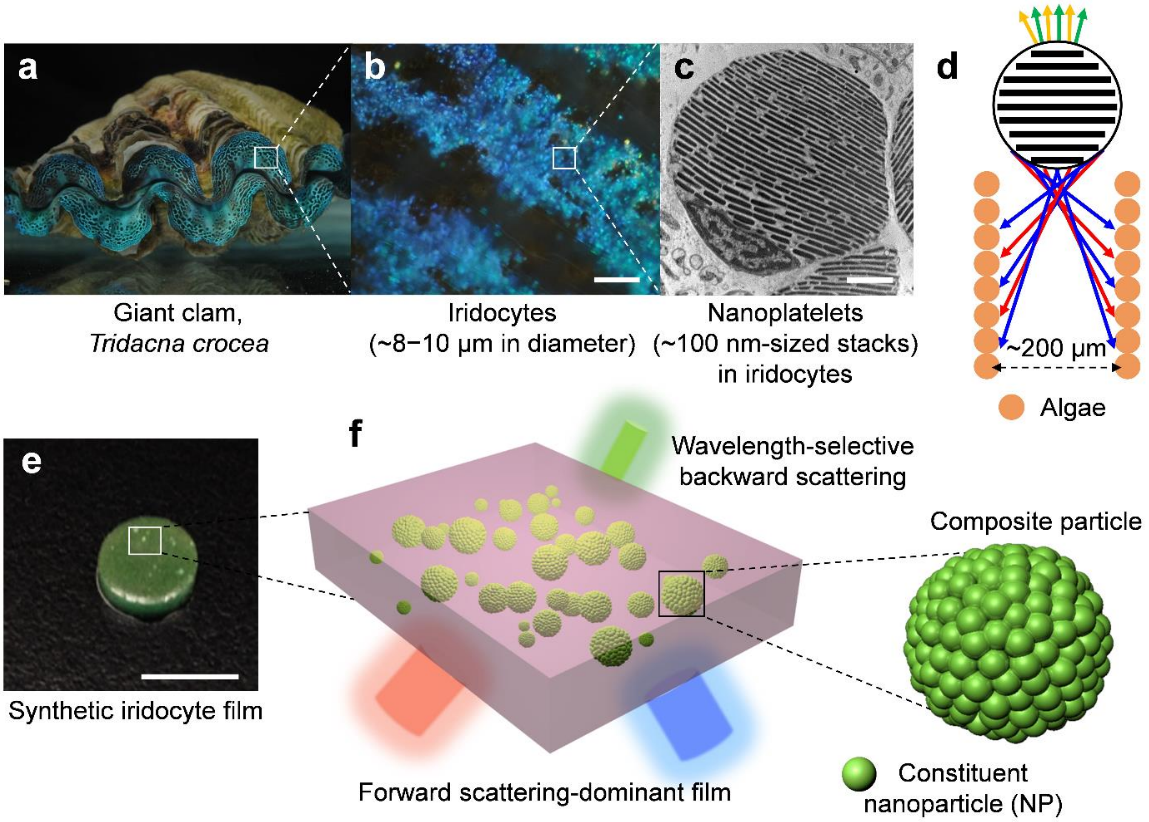

Figure 2.1 Overview of the scattering behavior of tridacnid giant clam iridocytes and design of the synthetic iridocyte film. a) Photograph of giant clam, *Tridacna crocea* (shell length, ≈6–8 cm). b) Reflected light micrograph of the clam iridocytes (scale bar: 200 μm). c) TEM image of the clam iridocyte showing the nanoplatelets (scale bar: 2 μm). d) Schematic illustration of the scattering behavior from a single iridocyte, which back-scatters yellow and green wavelengths while forward-scattering blue and red wavelengths. e) Photograph of a synthetic iridocyte film prepared by embedding silica composite particles in gelatin (scale bar: 5 mm). The size of the constituent silica NPs for this sample is 250 nm, leading to green reflected color. f) Schematic illustration of the scattering behavior from a synthetic iridocyte film. Green: composite particles, pink: gelatin film.

In the giant clam system, the size of iridocytes is on average 8–10 μm in diameter but not completely uniform. Therefore, we initially attempted to synthesize these composite particles with a standard microfluidic strategy, resulting in particles with a minimum diameter of ≈20 μm. However, the scattering behavior resulting from these particles was a poor match to that of clam iridocytes. Our numerical analysis of scattering suggests (see below) that both the size of the microparticles and the scale of the internal structure are critical to achieving the narrow forward distribution of scattering required for solar transformer function. Therefore, we shifted to a classic emulsification-evaporation strategy (see **Figure 2.2a**), which offered a simple yet scalable approach to mass-produce micron-sized spheres better resembling the size of giant clam iridocytes via vigorous vortexing, followed by solvent evaporation.

Meanwhile, the presence of nanostructure into microspheres affords control over the angular distribution of light in the forward direction, allowing for even illumination of vertical pillars in a way not afforded by simple microlenses. However, this nanostructure also inevitably introduces some loss from the system in the backward direction. Therefore, control over the size of the silica NPs used to build the micron-scale spheres allows us to tune the wavelengths of light unavoidably backscattered and lost from the system.[33] This NP-size design parameter could allow for further gains in photo-conversion efficiency since this loss to backscatter could in principle be engineered to occur at wavelengths that are inefficiently utilized by a given solar conversion technology. Our optical modeling shows that using NP assemblies rather than parallel nanoplatelets, as observed in the clam, offer an effective way to mimic the clam iridocytes in both the forward and back directions.

As seen from the scanning electron microscopy (SEM) images shown in **Figure 2.2b-c**, silica NPs were assembled into a nearly close-packed hexagonal array within the microsphere, in agreement with literature.[32, 34] **Figure 2.2d-f** shows visible-light reflected-light micrographs of composite particles with blue, green, and red colors assembled from silica NPs with a diameter of 200 nm, 250 nm, and 300 nm, respectively (see **Figure 2.3** for the SEM images of these particles). By embedding these composite particles (refractive index, $n \approx 1.45$) in a gelatin film ($n \approx 1.33$) at a density consistent with single-scattering through the film, we completed a synthetic version of the clam's forward-scattering tissue.

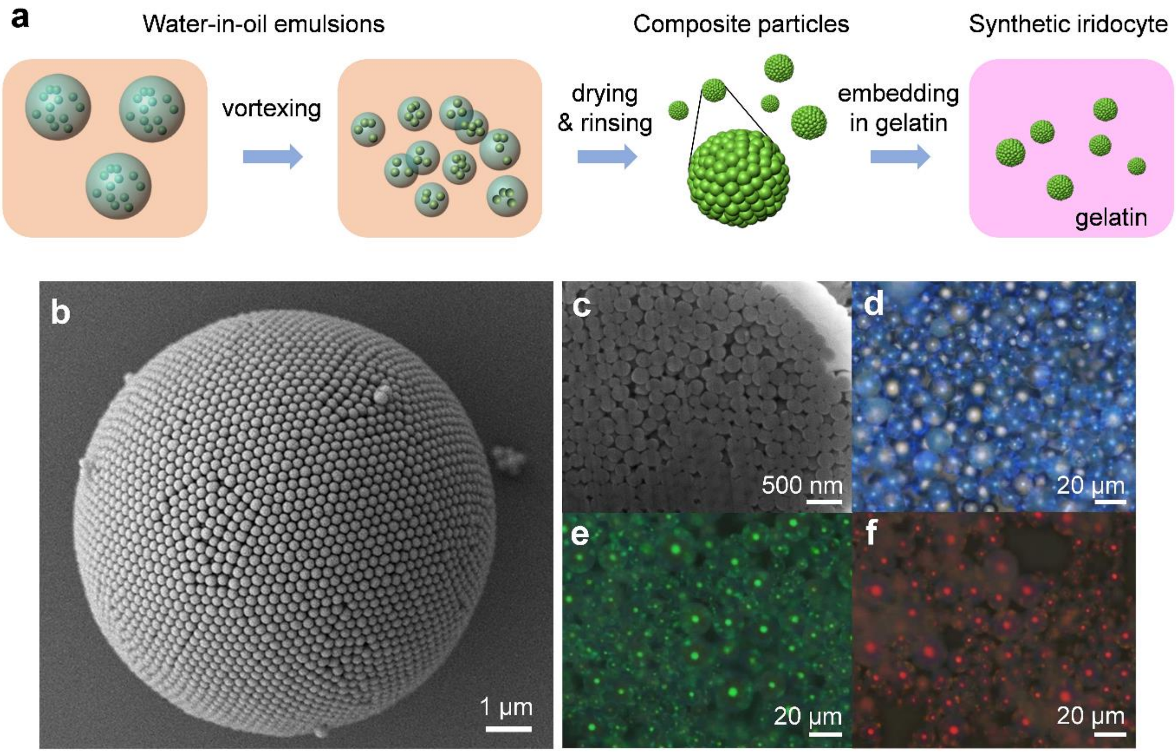

Figure 2.2 Synthetic iridocytes. a) Schematic illustration of the procedure to prepare the synthetic iridocyte film. The composite particles are prepared by the emulsification-evaporation process, followed by embedding in gelatin. b-c) SEM images of the composite particles from 250 nm-sized silica NPs. The cross-section is revealed by cutting the microsphere using focused ion beam (FIB). Optical microscope images of light reflected from the composite particles prepared from silica NPs with diameters of 200 nm (d), 250 nm (e), and 300 nm (f), respectively.

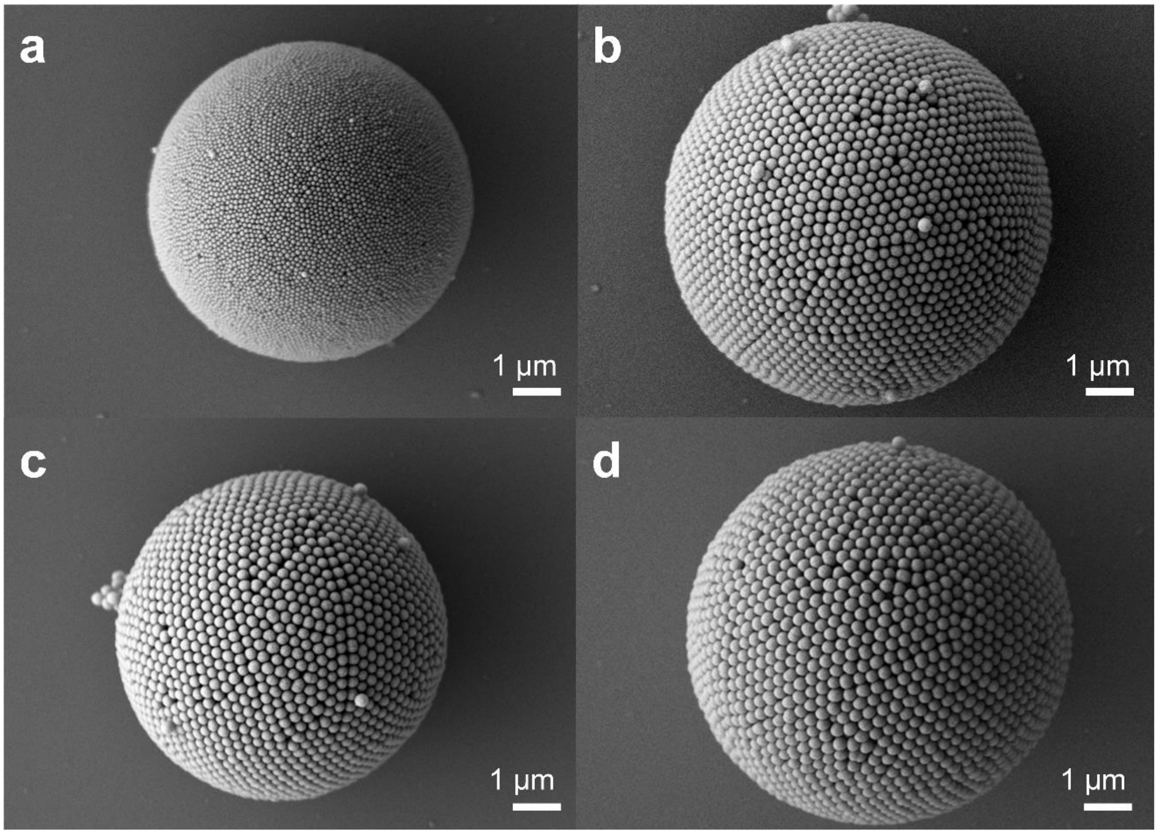

Figure 2.3 SEM images of composite particles fabricated from different sizes of silica NPs. 120 nm a), 200 nm b), 250 nm c), and 300 nm d). When the size of constituent NPs is 120 nm, the packing of NPs was not that regular due to the small size of NPs relative to the overall size of the composite particle (a few microns). The composite particles composed of 200 nm, 250 nm, and 300 nm-sized NPs, respectively, show fairly ordered crystalline structures with hexagonal arrays of close-packed NPs.

2.5 Numerical calculation for geometrical design

Given the flexibility of the emulsion strategy, we first needed to analytically identify structural parameters that would recapitulate the optical properties of the clam iridocytes using NPs rather than nanoplatelets. To this end, we thoroughly analyzed the system *in silico* using Mie theory and the Discrete-Dipole Approximation (DDA) approach.[35] The key control parameters for light scattering are the size parameter (χ) of the scatterer (assuming a spherical particle) and the complex refractive index (n) of the material.[36-38] The size parameter, $\chi = 2\pi r/\lambda$, is determined by the wavelength (λ) of the incident light and the radius (r) of the particle.[36] Because we intended to engineer the spatial distribution of light radiating from the micron-sized scatterers given a single direction of incident illumination, we focused on the scattering phase function, or the probability of light scattered in any given angle relative to a fixed angle of incidence. A comparison of the phase function of the clam's platelet-based iridocyte to our calculations for a simple microsphere and a composite NP-based microsphere then guided the choice of materials and parameters of the synthetic iridocytes, including final microparticle size, internal structure, and the refractive index contrast between the NPs and the surrounding medium. First, using Mie theory, we investigated simple microspheres (without NPs), providing insight into the interplay between size and composition of the microsphere before fine-tuning the internal nanostructures.[39, 40] **Figure 2.4a** shows damping or loss of incident light through the microsphere as a function of the imaginary part of the refractive index (n_i) and χ. As expected, the greater n_i of the particle, the more absorption; however, this damping effect is non-trivially complex with χ and becomes more pronounced with larger particles, or larger χ, in agreement with literature.[38] Therefore, to find the size of microparticle that would both minimize loss from absorption and also exhibit the desired forward scattering behavior, we also considered the asymmetry factor (g) or the mean cosine of scattering angle (θ) weighted by the phase function[41] for pairs of high and low refractive indices (**Figure 2.4b**). A particle with asymmetry parameter $g = 1$ scatters incident light mostly into the forward hemisphere, whereas a particle with $g = -1$ scatters light backward; $g = 0$ is completely isotropic scattering. Forward scattering particles are advantageous for our application since they result in more internal scattering within the medium and reducing loss in the backward direction, thereby increasing chances of absorption by the photosynthetic algae. **Figure 2.4a-b** shows that g generally increases as a function of χ, and is maximized for large, low index-contrast microspheres. For all particles considered, it is close to a maximum around $\chi = 40$. Therefore, for visible light of 400–700 nm, the optimum size of a synthetic iridocyte for efficient forward scattering is 5.1–8.9 μm, similar to the evolved size of clam iridocytes. This analysis also allows us to understand the optimal ratio of the real part of the refractive index of the two materials, the scatterer and the surrounding media (n_1/n_2), to reduce loss from backscattering. In general, low index contrast systems will be more efficient forward scatterers. Given the refractive index pair in giant clam iridocytes, $n_1/n_2 = 1.55/1.33 = \approx 1.17$, and our goal of designing scalable particles, we chose silica ($n_1 = 1.45$) as the high refractive index material and gelatin ($n_2 \approx 1.33$) as the low refractive index medium, resulting in an experimental $n_1/n_2 = \approx 1.09$.

We then explored how the presence of internal structure affects the scattering behavior of synthetic iridocytes vs. that of giant clam iridocytes. We used the DDA method,[35] which calculates the scattering and absorption of the electromagnetic waves by an object of arbitrary structure (see details in section 2.6), to calculate the phase functions (normalized scattering intensity per angle) for 1) a microsphere with no internal structure; 2) an isolated 100-nm NP; 3) an isolated 200-nm NP; 4) a 9-μm microparticle composed of 200 nm NPs (a "synthetic iridocyte") and 5) a 9-μm clam iridocyte (see **Figure 2.4c**). These calculations show that the simple microsphere, the synthetic iridocyte, and the clam iridocyte all exhibit strong forward scattering behaviors, confirming the primary roles of the overall size, shape, and refractive index contrast of these microspheres. More detailed examination in the angular range of θ = 0°–10° (**Figure 2.4d**) reveals that the forward scattering behaviors of a synthetic iridocyte and a clam iridocyte are more similar to each other than either is to the simple sphere. Both iridocyte particles exhibit a forward-scattering intensity a little higher than that of the simple sphere without internal structure and with the angular distribution of the forward scattering somewhat broader than that of a simple microlens. Correlated with this reshaping of the angular distribution and increase in the intensity of the forward scattering from the iridocyte particles, the internal structures of the iridocytes also lead to wavelength-selective backscattering of light. In the clam system, this backscatter from the internal particle structure is unavoidably tied to the optimal angular distribution in the forward direction, and so is tuned wavelength that is least absorbed by the algae. We sought to recapitulate this wavelength-tuned backscatter in our synthetic iridocyte system by tuning the size of the constituent NPs.

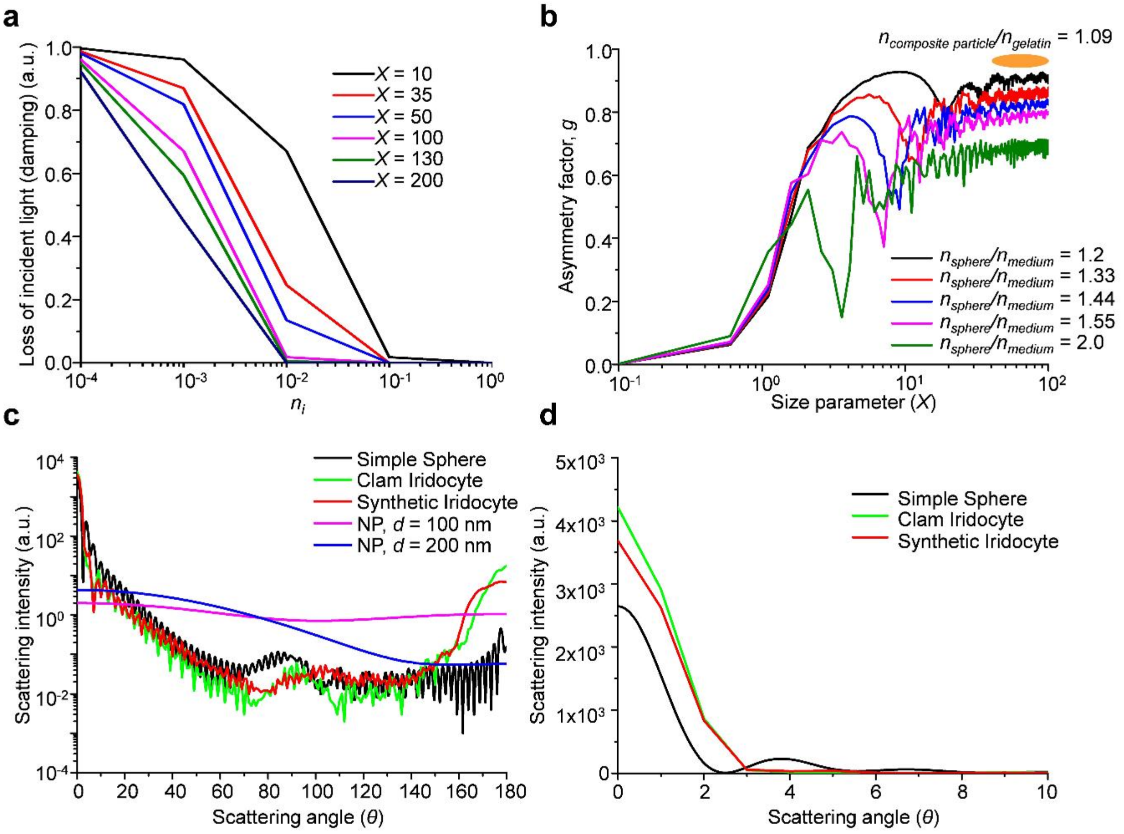

Figure 2.4 Calculated and modeled geometrical design for the synthetic iridocyte system comparable to the clam iridocyte system. a) Calculated damping plots of $exp(-4\chi n_i)$ as a function of n_i, of the light transmitted through an individual simple microsphere for different values of the size parameter χ. b) Asymmetry factor (g) calculated for an individual simple microsphere as a function of size parameter (χ) with different refractive index pairs n_{sphere}/n_{medium}. The optimum range for the size parameter and the refractive index pair of our synthetic iridocyte is shown as an orange-colored area. c) DDA calculation of the integral-normalized phase function for a synthetic iridocyte composed of 200 nm NPs, a simple sphere with the same diameter of 9 μm, and a single silica NP (diameters, 100 nm and 200 nm) in comparison with a giant clam iridocyte. All calculations assumed the same refractive index pair as the clam iridocyte system. Scattering angle (θ = 0°) means the scattered light is in the same direction as the incident light, i.e., forward scattering. θ = 180° means the scattered light is in the opposite direction of the incident light, i.e., backward scattering. d) The linear plot for c in the range of θ = 0°–10°. The illumination wavelength was λ = 509 nm.

Since the size of the synthetic iridocytes prepared by the emulsification-evaporation process is not uniform, we also performed a calculation to estimate the effect of a distribution of particle diameters (**Figure 2.5**). When the scattering from a distribution of sizes is averaged, the interference fringes observed from a single sized iridocyte are smoothed out, otherwise, the scattering intensity is nearly identical to that of the single-sized iridocyte in the range of $\theta \approx 10°–165°$ scattering angles for the narrow size distribution (5.1–8.9 μm). The phase function resulted from the averaged particles has a broader lobe in the forward direction ($\theta \approx 0°–10°$) and less relative intensity in the back direction ($\theta \approx 165°–180°$) compared to that from a single sized microparticle (note **Figure 2.5** is on a log scale). Therefore, we treat the distribution in particle size obtained by the emulsification-evaporation process approach as a “feature not a bug” in engineering these particles for potential solar energy applications.

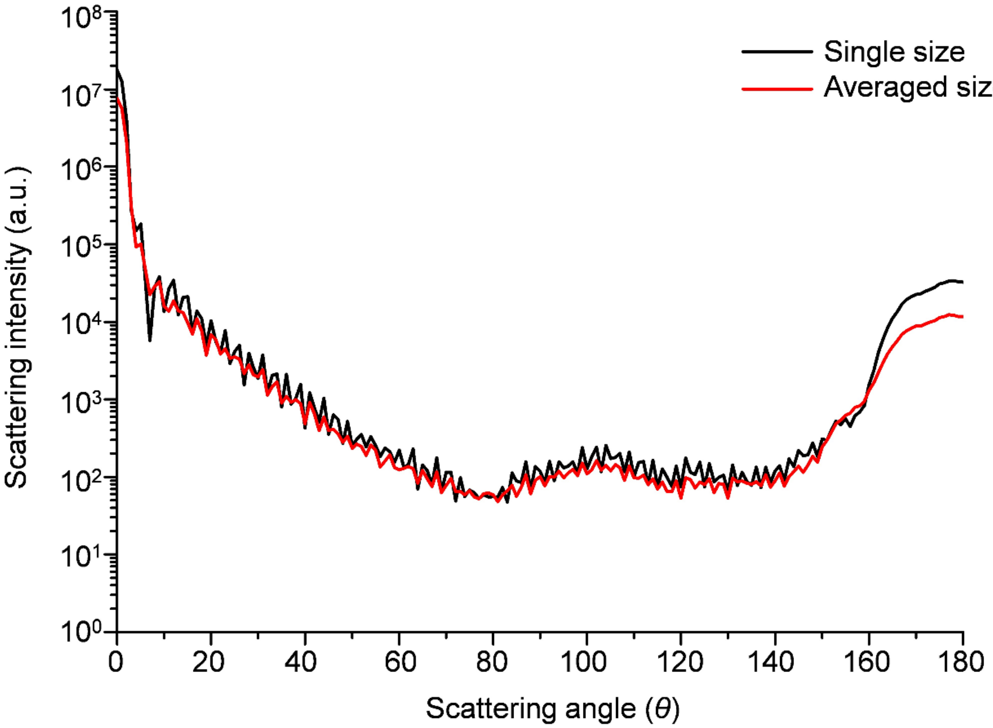

Figure 2.5 Calculated size distribution of synthetic iridocytes barely affects the scattered intensity. Modeled scattered light from a synthetic iridocyte with a diameter of 8.8 μm compared to the scattered light averaged over synthetic iridocytes with diameters of 5 μm, 7 μm, and 8.8 μm, respectively. All constituent NPs are 200 nm in diameter and the illumination wavelength, λ is 509 nm.

Our models also predicted how constituent NP size would alter the wavelength-selective behavior of light reflected from the system in the backward direction. As shown in **Figure 2.6**, at a fixed wavelength of 509 nm, synthetic iridocytes with smaller constituent NPs (100–150 nm in diameter) generate less back-scattering, while those with larger NPs (200–300 nm in diameter) show somewhat stronger backward-scattering at specific wavelengths attributed to the Bragg reflection from the periodic arrangement of the silica NPs.

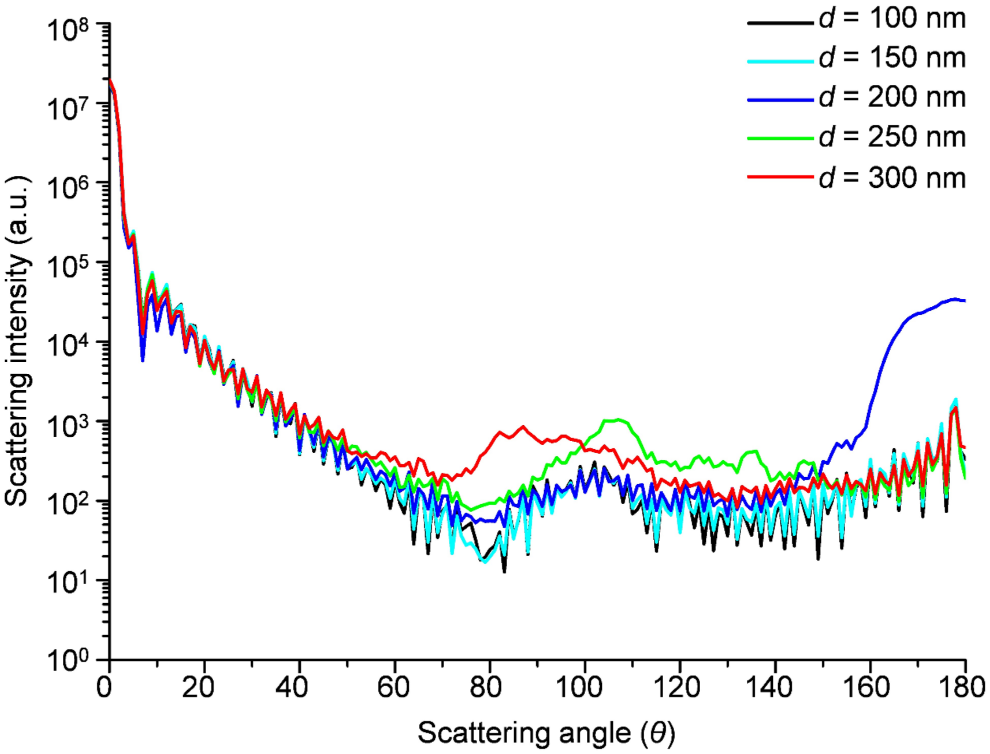

Figure 2.6 Calculated scattering behaviors of the synthetic iridocytes composed of silica NPs with different diameters as a function of the scattering angle. Varying the diameter of the NP is a way to change the backscattering of light for the desired wavelength. The diameter of synthetic iridocytes is kept as 8.8 μm and the illumination wavelength, $\lambda = 509$ nm.

2.6 Fabrication

Guided by the predicted scattering behavior from a single synthetic iridocyte, we fabricated synthetic iridocytes from different sizes of silica NPs (average diameter of the iridocyte: ≈5.93 ± 2.89 μm) and embedded them in gelatin (see **Figure 2.7a-d**) for optical characterization. We refer to them here according to the size of the constituent silica NP, e.g., "120 nm Synthetic Iridocytes". For comparison, we also prepared gelatin films with the same total mass per volume of randomly dispersed silica NPs (see **Figure 2.7e-h**), referred to by the constituent NP size, e.g., "120 nm NPs". **Figure 2.8** shows environmental SEM (ESEM) images of the cross-sections of these films. As seen in **Figure 2.8a-d**, the composite microparticles are randomly dispersed in the gelatin films with little aggregation. The films containing NPs also show the random distribution with little aggregation, with the exception of 120 nm NPs (see **Figure 2.8e-h**), which probably aggregated in the solution prior to mixing in gelatin.

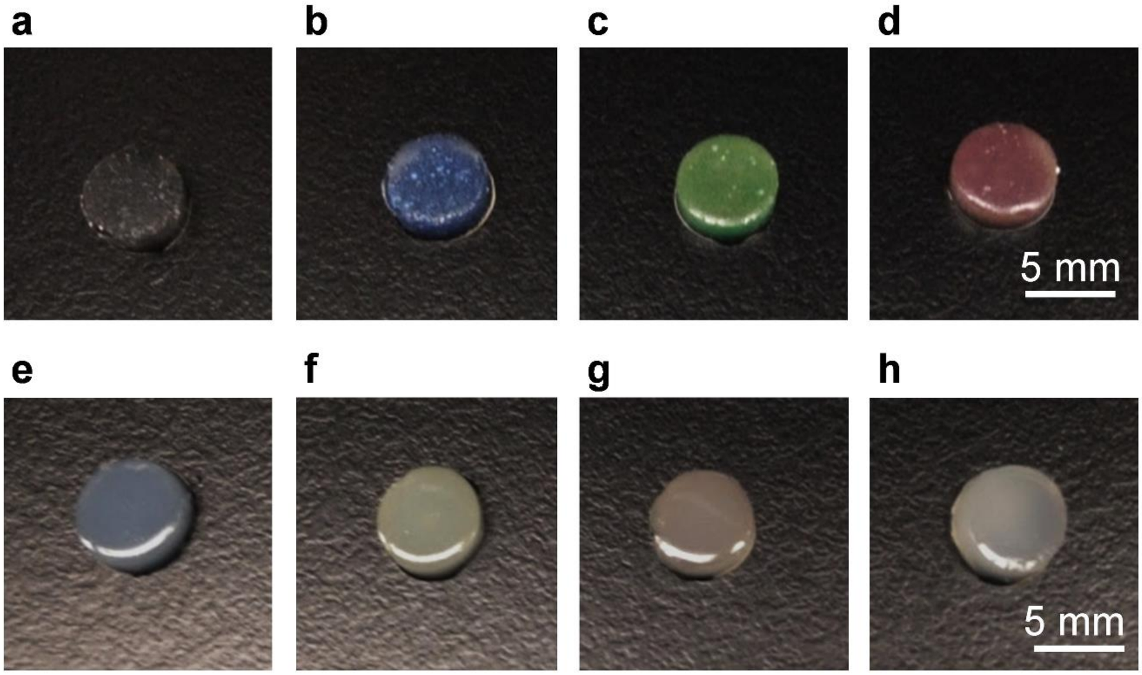

Figure 2.7 Photographs of the synthetic iridocyte films consisting of different sizes of silica NPs (a-d) and silica NPs-embedded gelatin films for each size of NPs (e-h). a-d) Synthetic Iridocytes 120 nm (a), 200 nm (b), 250 nm (c), and 300 nm (d). e-h) NPs 120 nm (e), 200 nm (f), 250 nm (g), and 300 nm (h).

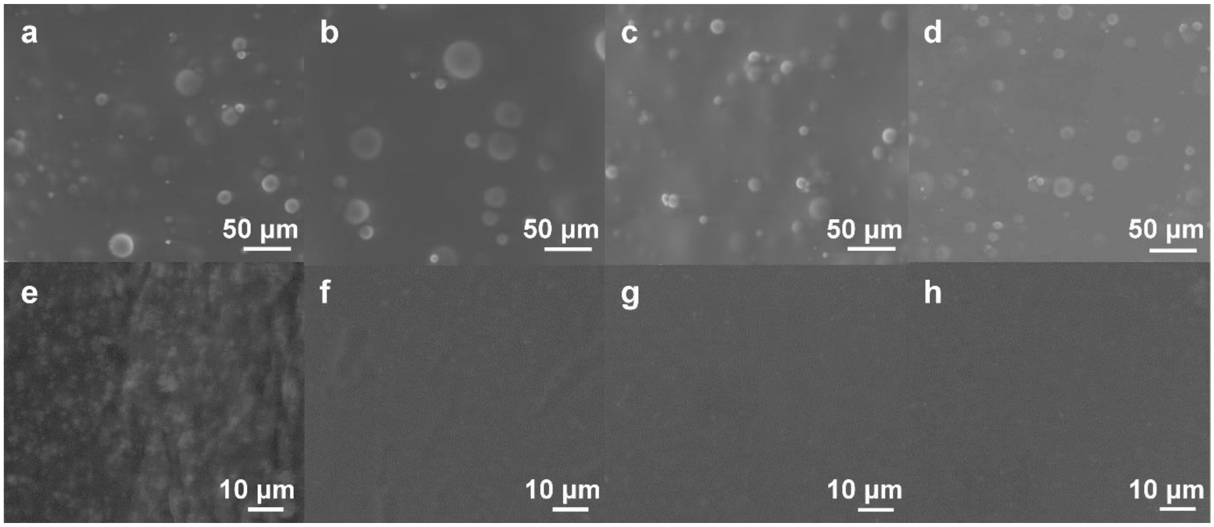

Figure 2.8 Cross-sectional ESEM images of the gelatin films. a-d) Embedded with composite particles consisting of silica NPs of different diameters. 120 nm (a), 200 nm (b), 250 nm (c), 300 nm (d). e-h) Embedded with the corresponding silica NPs only of the same weight as that in synthetic iridocytes films.

2.7 Conclusions

In conclusion, we designed and fabricated synthetic iridocytes by embedding composite particles consisting of silica NPs in a low refractive index gelatin medium. The synthetic iridocytes are expected to be highly forward scattering with light distributed within a narrow angular range (15°-wide cone), which ultimately leads to an even illumination of the sides of micron-spaced high aspect-ratio micropillars within the medium. Crucially, this internal structure ensures that most or all of the incident light is redirected along the sides of the pillars rather than traveling unaltered out the back of the system, as would be the case for simple micron-scale microlens-like particles. Both factors, the narrow but angularly tuned forward scattering, and higher forward-scattering efficiency, will be required in a system able to utilize the solar resource optimally. Importantly, our calculation suggests that while the shape and size range of the forward scatters are critical to the forward scattering behaviors, particle size uniformity is not essential, allowing us to use a simple vortexing method to mass produce the composite microparticles that are near-exact mimics of the optical functions of giant clam’s iridocytes. This analysis and related synthetic particles will inspire new geometric designs for intelligent and sustainable optical systems to better harvest solar energy with smaller footprints, and higher yield, and to design more efficient photobioreactors for clean energy, e.g., algal-based biofuel production.

2.8 References

[1] H.-N. Kim, S. Vahidinia, A. L. Holt, A. M. Sweeney, S. Yang, *Advanced Materials* **2017**, *29*, 1702922.

[2] C. Y. Chen, G. D. Saratale, C. M. Lee, P. C. Chen, J. S. Chang, *Int. J. Hydrogen Energy* **2008**, *33*, 6886.

[3] D. Gust, T. A. Moore, A. L. Moore, *Acc. Chem. Res.* **2009**, *42*, 1890.

[4] P. V. Kamat, *J. Phys. Chem. C* **2007**, *111*, 2834.

[5] A. Hagfeldt, M. Gratzel, *Acc. Chem. Res.* **2000**, *33*, 269.

[6] M. Gratzel, *Nature* **2001**, *414*, 338.

[7] F. C. Krebs, *Sol. Energ. Mat. Sol. C.* **2009**, *93*, 394.

[8] P. Wang, Y. Guo, S. Yuan, C. Yan, J. Lin, Z. Liu, Y. Lu, C. Bai, Q. Lu, S. Dai, C. Cai, *Res. Chem. Intermed.* **2016**, *42*, 625.

[9] Amirreza Kiani, Brandon R. Sutherland, Younghoon Kim, Olivier Ouellette, Larissa Levina, Grant Walters, Cao-Thang Dinh, Mengxia Liu, Oleksandr Voznyy, Xinzheng Lan, Andre J. Labelle, Alexander H. Ip, Andrew Proppe, Ghada H. Ahmed, Omar F. Mohammed, Sjoerd Hoogland, E. H. Sargent, *Appl. Phys. Lett.* **2016**, *109*, 183105.

[10] J. Kanters, M. C. Dubois, M. Wall, *Arch. Sci. Rev.* **2013**, *56*, 141.

[11] D. Kim, K. K. Sakimoto, D. C. Hong, P. D. Yang, *Angew. Chem. Int. Ed.* **2015**, *54*, 3259.

[12] C. Liu, N. P. Dasgupta, P. D. Yang, *Chem. Mater.* **2014**, *26*, 415.

[13] P. M. Schenk, S. R. Thomas-Hall, E. Stephens, U. C. Marx, J. H. Mussgnug, C. Posten, O. Kruse, B. Hankamer, *Bioenergy Res.* **2008**, *1*, 20.

[14] D. Dye, J. Muhs, B. Wood, R. Sims, *J. Sol. Energy Eng. Trans. ASME* **2011**, *133*, 7.

[15] B. Kong, R. D. Vigil, *Bioresource Technol.* **2014**, *158*, 141.

[16] B. B. Fischer, M. Wiesendanger, R. I. L. Eggen, *Plant Cell Physiol.* **2006**, *47*, 1135.

[17] M. D. Ooms, P. J. Graham, B. Nguyen, E. H. Sargent, D. Sinton, *Biotechnol. Bioeng.* **2017**, 114, 1160.

[18] S. W. Baek, J. Noh, C. H. Lee, B. Kim, M. K. Seo, J. Y. Lee, *Sci. Rep.* **2013**, *3*, 1726.

[19] W. Liu, J. F. Zhang, B. Lei, H. T. Ma, W. K. Xie, H. J. Hu, *Opt. Express* **2014**, *22*, 16178.

[20] Z. H. Wang, N. An, F. Shen, H. P. Zhou, Y. X. Sun, Z. N. Jiang, Y. H. Han, Y. Li, Z. Y. Guo, *Nanoscale Res. Lett.* **2017**, *12*, 8.

[21] S. S. Ahsan, B. Pereyra, E. E. Jung, D. Erickson, *Opt. Express* **2014**, *22*, A1526.

[22] D. W. Klumpp, B. L. Bayne,, *J. Exp. Mar. Eco.* **1992**, *155*, 105.

[23] D. J. Griffiths, H. Winsor, T. Luong-Van, *Austr. J. Zoo.* **1992**, *40*, 319.

[24] A. L. Holt, S. Vahidinia, Y. L. Gagnon, D. E. Morse, A. M. Sweeney, *J. R. Soc. Interface* **2014**, *11*, 20140678.

[25] J. Cornet, *Chem. Eng. Sci.* **2010**, *65*, 985.

[26] Z. Csőgör, M. Herrenbauer, K. Schmidt, C. Posten, *J. Appl. Phycology* **2001**, *13*, 325.

[27] J. W. Shim, S.-H. Kim, S.-J. Jeon, S.-M. Yang, G.-R. Yi, *Chem. Mater.* **2010**, *22*, 5593.

[28] L. A. Connal, N. A. Lynd, M. J. Robb, K. A. See, S. G. Jang, J. M. Spruell, C. J. Hawker, *Chem. Mater.* **2012**, *24*, 4036.

[29] G. R. Yi, T. Thorsen, V. N. Manoharan, M. J. Hwang, S. J. Jeon, D. J. Pine, S. R. Quake, S. M. Yang, *Adv. Mater.* **2003**, *15*, 1300.

[30] A. S. Utada, E. Lorenceau, D. R. Link, P. D. Kaplan, H. A. Stone, D. A. Weitz, *Science* **2005**, *308*, 537.

[31] S. H. Kim, J. W. Shim, S. M. Yang, *Angew. Chem. Int. Ed.* **2011**, *50*, 1171.

[32] S. H. Kim, S. Y. Lee, S. M. Yang, G. R. Yi, *NPG Asia Mater.* **2011**, *3*, 25.

[33] P. Jiang, J. F. Bertone, K. S. Hwang, V. L. Colvin, *Chem. Mater.* **1999**, *11*, 2132.

[34] J. G. Park, S. H. Kim, S. Magkiriadou, T. M. Choi, Y. S. Kim, V. N. Manoharan, *Angew. Chem. Int. Ed.* **2014**, *53*, 2899.

[35] B. T. Draine, P. J. Flatau, *J. Opt. Soc. Am. A* **1994**, *11*, 1491.

[36] P. Chylek, V. Ramaswamy, A. Ashkin, J. M. Dziedzic, *Appl. Opt.* **1983**, *22*, 2302.

[37] M. Mikrenska, P. Koulev, *J. Quant. Spectrosc. RA* **2009**, *110*, 1411.

[38] H. T. Yu, J. Q. Shen, Y. H. Wei, *J. Quant. Spectrosc. RA* **2009**, *110*, 1178.

[39] H. C. van de Hulst, *Light Scattering by Small Particles*, Dover Publications, New York **1957**.

[40] J. E. Hansen, L. D. Travis, *Space Sci. Rev.* **1974**, *16*, 527.

[41] K. N. Liou, Y. Takano, P. Yang, *J. Quant. Spectrosc. RA* **2010**, *111*, 1980.

CHAPTER 3. Optical characterization of light scattering and distribution in composite films embedded with multiscale particles

Adapted from:

Kim, H.-N., Vahidinia, S., Holt, A. L., Sweeney, A. M.*, and Yang, S.* (2017), Geometric Design of Scalable Forward-Scatterers for Optimally Efficient Solar Transformers. Adv. Mater., 2017, 29, 1702922.[1] Reproduced with permission.

3.1 Introduction

In this section, we show how we characterized the optical properties of as-prepared synthetic iridocyte films and compared them with those of real clam iridocyte layers. Further, here we demonstrate the detailed characterization methods for measuring the angular distribution of scattering and intra-film radiometry of films. Our experimental results on the scattered light intensity show how these synthetic iridocytes have an optimized angular distribution of scattering in the forward direction such as those in clam iridocyte systems. Moreover, we characterize light distribution in our synthetic clam system via intra-film radiometry measurement.

3.2 Experimental methods

3.2.1 Measurement of film phase function

Scattering intensity as a function of angle for both types of gelatin films embedded with composite particles and the dispersed NPs was measured using a custom-built device (see the setup in **Figure 3.1**). In this setup, a collimated beam from a tungsten-halogen light source was directed perpendicular to the film sample that was mounted on a glass slide. A detector optical fiber was mounted on a pivoting arm, allowing it to rotate in a plane around the sample. The sample was oriented such that the beam was incident on the glass slide, and the detector had an unobstructed view of the film, thereby reducing any angular aberrations introduced by having an extra layer of glass in the setup. The direction of incoming light (tungsten-halogen light source) was fixed to be perpendicular to the sample film and the angle between the sample substrate, and the detector rotated to positions of 0°–50° and 110°–165° relative to the incident beam. The detector fiber was coupled to a tungsten-halogen light source and a USB2000-FL fiber optic spectrometer operated with SpectraSuite software (Ocean Optics, Dunedin, FL, USA). An initial reference measurement was defined using the amount of light transmitted through an empty glass slide measured at 0°. With the film sample in place, the detector arm then rotated in increments of 5° within the angle ranges listed above, and the integration time was adjusted appropriately for each measurement. Scattered intensity at each angle with respect to the film was divided by integration time and then normalized by the measurement of initial beam intensity transmitted through a glass slide. Scattering from the gelatin film alone was quite similar to that from gelatin embedded with well-dispersed NPs, making measurements normalized by a blank gelatin film too noisy to report. For this reason, we normalized all data using the glass slide alone, and report the gelatin scattering data in Figure 4 along with our sample data.

3.2.2 Construction of optical microprobe setup

Optical microprobes were constructed according to our previous study (see **Figure 3.5**).[2] One end of a 200 μm silica-core fiber optic assembly (Ocean Optics, Dunedin, FL, USA) was removed. Then the stripped fiber end was heated with a butane torch and pulled, narrowing the diameter to 50 μm. The sides of the uncovered fiber were painted with a film-opaquing pen to prevent stray light from entering the fiber, leaving a small transparent opening only at the tip. To create a probe sensitive to spectral scalar irradiance, we created a small light-scattering microsphere at the end of the fiber using a high-viscosity UV-curable resin impregnated with titanium dioxide (DELO Industrie Klebstoffe, Windach, Germany). This spherical fiber tip had a diameter 3–4 times of the fiber diameter. The sphere was cured at room temperature for 5 h using a UV lamp (Compact Hand Held, 4 Watt, Short Wave and Long Wave Ultraviolet Lamp, Fischer Scientific). All measurements reported here used the same probe to minimize the effect due to variations in probe diameter.

3.2.3 Intra-film radiometry measurement

This fiber optic probe was then coupled to the tungsten-halogen light source and the USB2000-FL fiber optic spectrometer with SpectraSuite software (Ocean Optics) and mounted vertically, with the probe tip pointing up. The gelatin film (diameter, 1 cm and thickness, 2 mm) containing either the composite particles or the dispersed silica NPs was mounted in a petri dish with a 5 mm-diameter aperture in the bottom surface of the dish. Here, we used two-time concentrated gelatin (0.358 g in 2 mL of water) to prevent the film from being ruptured by the optical probe during sample manipulation. The petri dish with film sample was then placed on a vertically translating stage and positioned with the aperture's center over the fiber optic probe tip. We then lowered the petri dish in 150 μm increments over the fixed optical probe, pushing the probe through the gelatin film. The measurement was completed when the probe tip became visible at the top surface of the film and in contact with air, which was noticeable by a sharp decrease of light intensity detected by the probe due to the loss of light refracting into the probe tip from the gelatin film. Here we report data from a depth of 1 mm below the surface of the film to the top of the film and normalized by the light intensity measured at the top surface of each sample.

3.3 Optical characterizations

3.3.1 Angular distribution of scattering

We characterized the phase functions of 250 nm synthetic iridocytes and 250 nm NPs in the visible wavelengths (450–750 nm) (see the setup in **Figure 3.1**). For the 250 nm synthetic iridocytes, the number density of microparticles was chosen such that there were only 1–2 microparticles in a 1D path through the film, ensuring that the film was single-scattering. For the 250 NPs, we used the same total mass of silica as was present in 250 nm synthetic iridocytes. The resulting film's phase functions at angular ranges of θ = 0°–50° and θ = 110°–165° were measured using a fiber-optic spectrometer coupled to a goniometer, then integral-normalized. The log-scaled radial plot in **Figure 3.2a** clearly shows that a synthetic iridocyte (green line) scatters incident light mostly into forward angles ($\theta = \approx 0°–15°$) and scatters less than 0.01% of incident light into backward angles, similar to the DDA-calculated results on both synthetic iridocyte and clam iridocyte with nanoplatelet structures at 509 nm. For all systems except for the multiple-scattering film, the large majority of the scattered light intensity is accounted for in the forward angles of 0°–5° (the phase function at 5º is less than 1% of the intensity at 0°). At the narrow forward angles (θ = 0°–5°) where most of the incident light is scattered, both the calculations and experimental measurements of the synthetic iridocytes and clam iridocytes show a wider angular distribution compared to the much sharper angular distribution of the isolated NPs film (cyan line, **Figure 3.2b**). Therefore, experimentally measured scattering from our single synthetic iridocyte film closely matched our calculations of both the same synthetic iridocyte film and the real structure of the clam iridocyte. We also measured a film with a larger number of synthetic iridocytes (≈55 beads in a path through the 1 mm thick film). In this case, the film shows more isotropic scattering rather than forward-dominant scattering due to multiple scattering events within the synthetic iridocyte film as the light passes through, broadening both the forward and backward scattering peaks. A similar trend is observed across the visible wavelength range: NP films have a sharp decrease as the forward angle increases while the synthetic iridocyte films have a wide angular distribution in the forward angles. (**Figure 3.3**). As predicted, the backscattered wavelengths could be tuned by the constituent NP size; we observed peaks at ≈560–570 nm and ≈660–670 nm from the 250 nm NP and 300 nm NP synthetic iridocyte films, respectively (**Figure 3.4**). This result is fairly consistent with the Bragg's law, $\lambda = 2dn_{eff}$, where d is the lattice spacing, and n_{eff} is the effective refractive index.

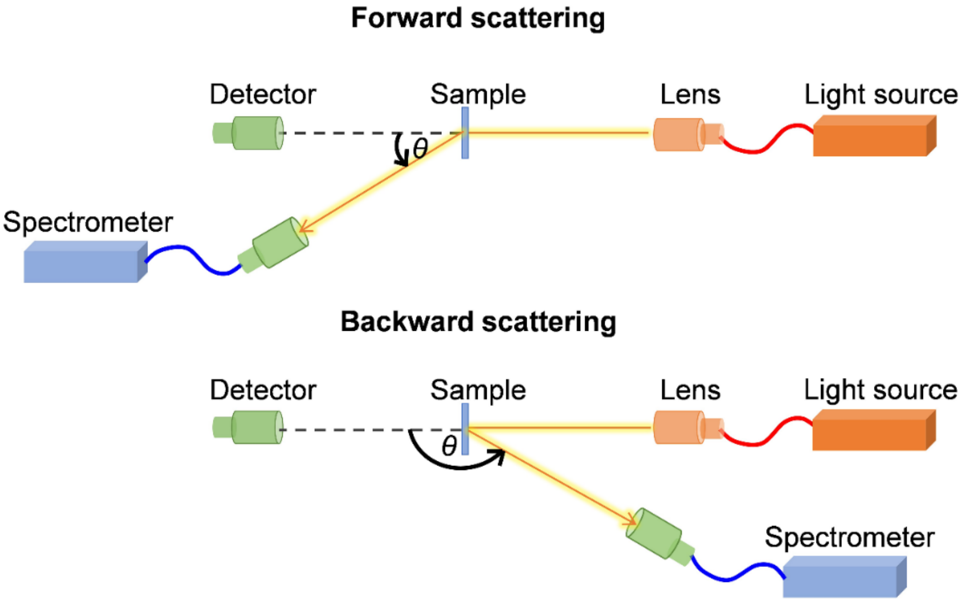

Figure 3.1 Optical setup for measuring the angular distribution of the forward- and backward scattering. With the film sample located perpendicular to the direction of incident light, the detector arm was rotated in increments of 5° within the angle ranges listed above. The transmitted light intensity (*T*) at the forward angles (0°–50°) and the backward angles (110°–165°) were measured. All *T* were normalized by each integration time and the light intensity measured from an empty glass slide.

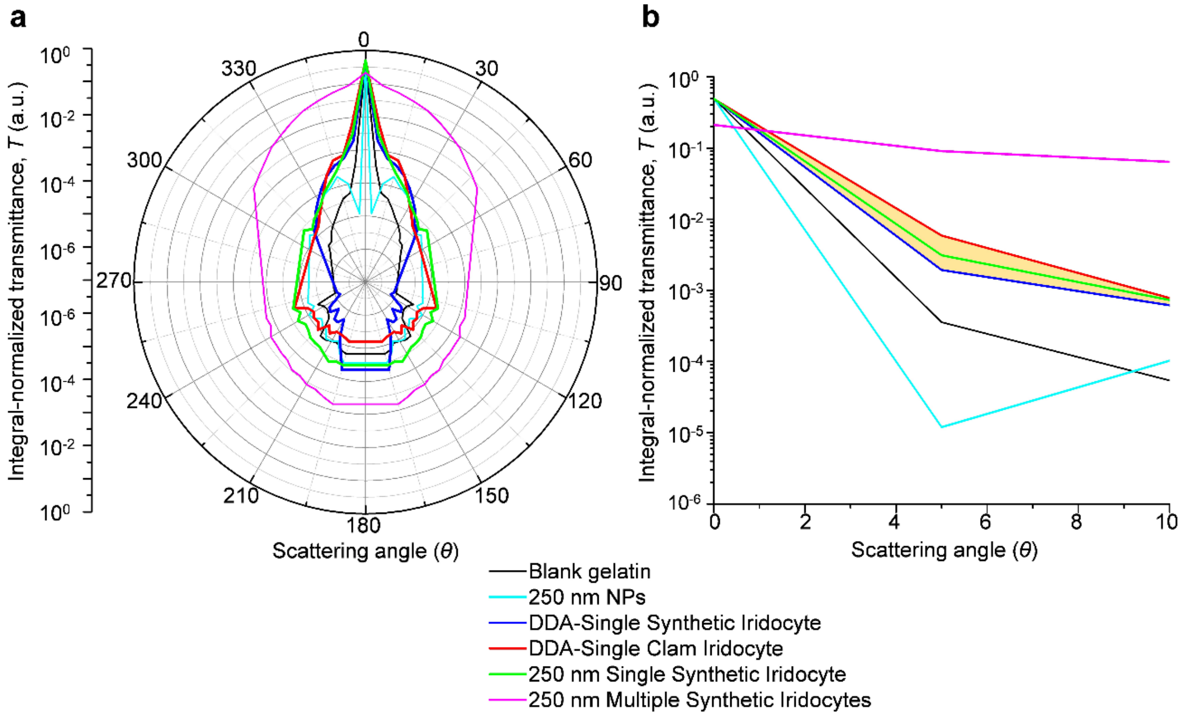

Figure 3.2 Angular distribution of forward- and backward scattering measured from the synthetic iridocyte films vs. silica NPs film and the comparison of them with the DDA-calculated results. a) Experimentally characterized phase functions (*T*) at a fixed wavelength of 509 nm for the angular range of θ = 0°–50° and θ = 110°–165°. For the radial plot, the light intensities for the angular range restricted from measurement by our experimental geometry (50°–110° and 165°–180°) were extrapolated from measured data (the unmeasured data points were replaced by straight lines) because intensities in this range were so low compared to the intensity at the forward peak. b) The integral-normalized transmitted light intensities at narrow forward angles (θ = 0°–10°). The yellow-shaded area shows that the scattering behavior of synthetic iridocyte is well-matched to the DDA-calculated results on a single synthetic iridocyte and a single clam iridocyte.

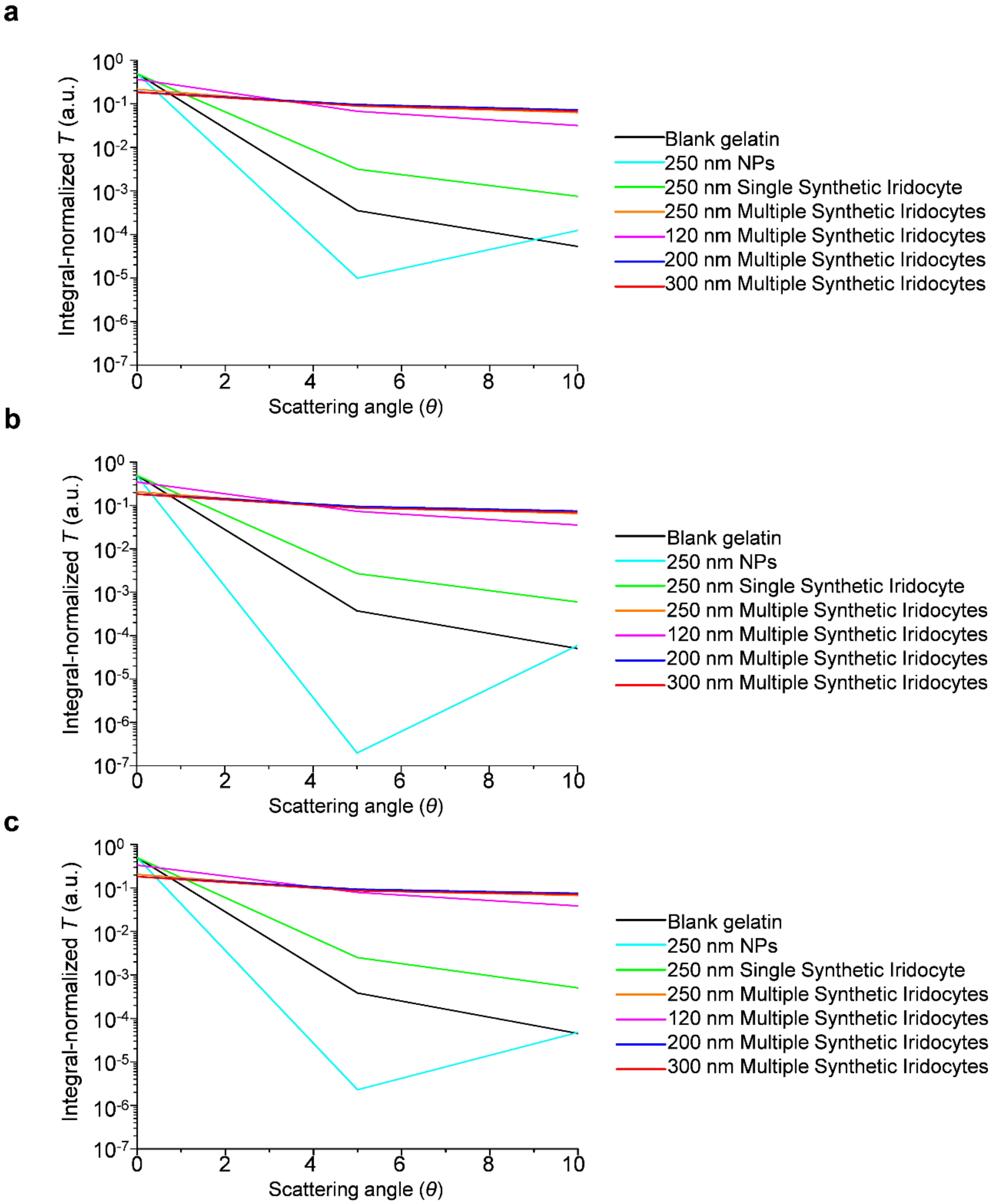

Figure 3.3 Angular distribution of the forward scattering measured from the synthetic iridocyte films and silica NP films. The integral-normalized transmitted light intensities only at the narrow forward angles ($\theta = 0°–10°$) at a fixed wavelength of 500 nm (a), 600 nm (b), and 700 nm (c), respectively.

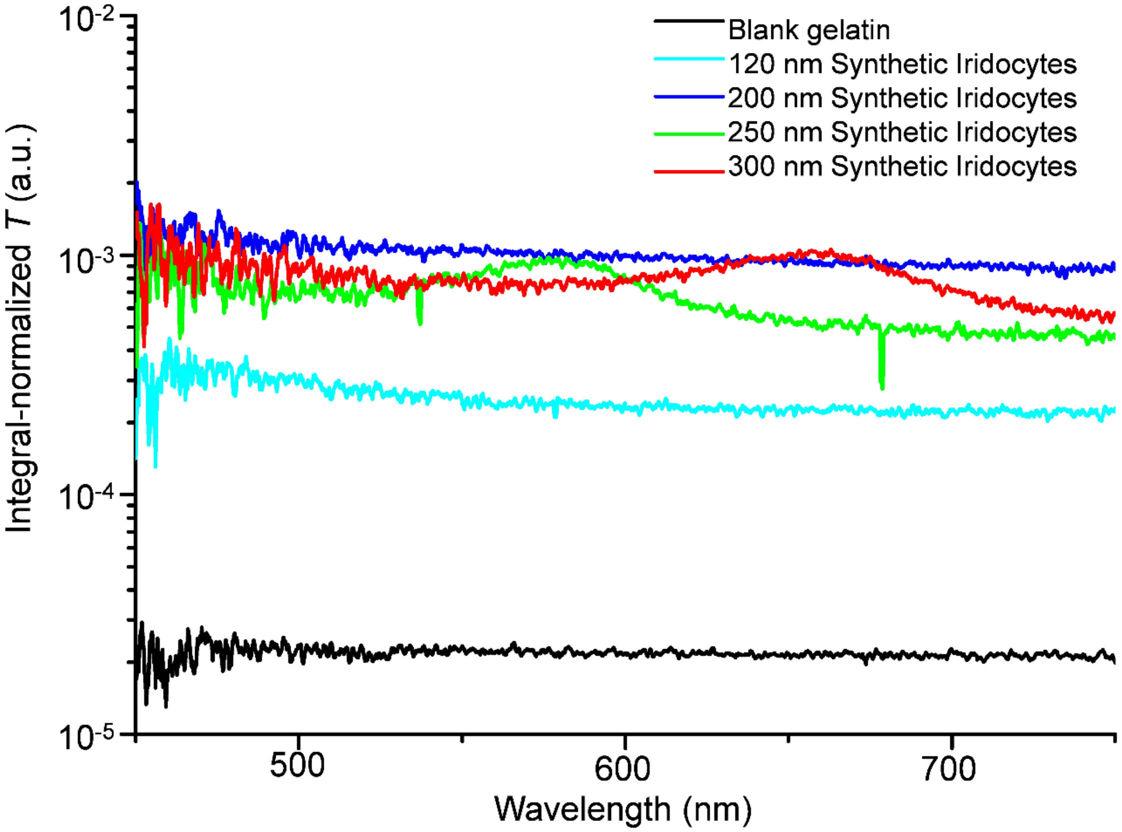

Figure 3.4 The integral-normalized transmittance (*T*) for the blank gelatin and synthetic iridocytes consisting of silica NPs of different diameters at the fixed backward scattering angle ($\theta = 165°$).

3.3.2 Intra-film radiometry

The optimal shape of the phase function in the forward direction for a given application will depend on the spatial arrangement of the underlying absorbers in that system. In the giant clam, the function of these structured particles is to shape the angular distribution of scattered light in the forward direction, evenly illuminating the algae organized in micropillars that are located there. If there were simple spheres present in the clam, the narrow forward scattering would mean that much of the incident light would exit out the back of the system, missing the sides of the pillars. To prove light distribution within a layer of our iridocytes, similar to the geometry of the clam system (see the optical setup in **Figure 3.5**), we measured light within a gelatin film with a high number density of synthetic iridocytes. We constructed the optical probes with high refractive index TiO_2 scattering ball at the end of an optical fiber,[2] and illuminated a horizontal film from the top surface. The probe was pushed into the film from the bottom to the top surface at increments of 150 µm, thereby measuring the scalar irradiance as a function of distance from the top surface of the film, where the number of scatterers present between the probe and the light source increases (**Figure 3.6a**).

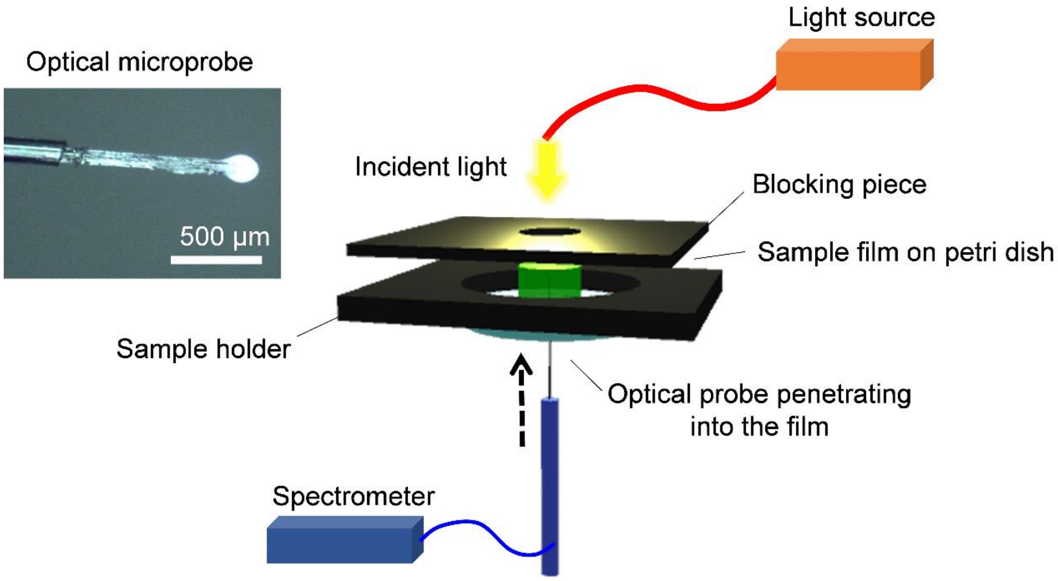

Figure 3.5 Optical setup for intra-film radiometry measurement. Schematic illustration of the experimental setup. Inset: optical microscopy image of the probe with high refractive index TiO_2 scattering ball at the end of the optical fiber.

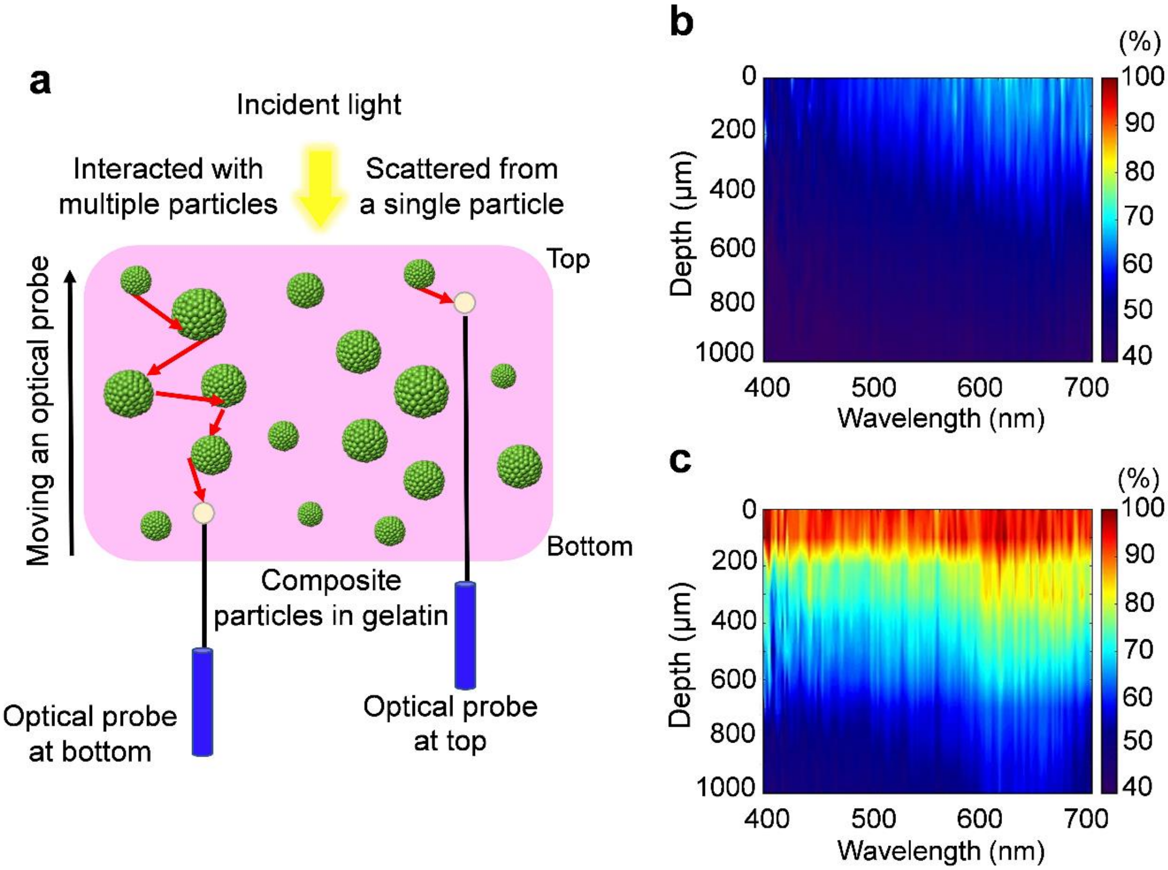

Figure 3.6 Measured intra-film radiometry data. a) Schematic illustration of the effect of vertical probe position on the number of particle scattering events contributing to the scalar irradiance detected by the probe. b-c), The scalar irradiance intensity as a percentage of the film surface scalar irradiance for a film containing isolated silica NPs (b) and for a film containing composite particles (c). Constituent NPs are 250 nm in both films.

Within films containing disaggregated NPs, scalar irradiance is low compared to the surface at all points, and greater than 50% of the surface irradiance only within ≈200 µm of the surface. These films of isolated NPs also show a marked wavelength dependence, with greater attenuation of short wavelengths within the film compared to long wavelengths. In comparison, in films with synthetic iridocytes, in-film irradiance remains very close to the surface irradiance to a depth of 200 µm and from there, decreases gradually to 50–60% of the surface irradiance at a depth of about 800 µm. There is also less wavelength dependence within films with synthetic iridocytes compared to those with isolated NPs.

In the synthetic iridocyte films, there were about 55 particles present per 1 mm depth of the film, such that the region of the film with scalar irradiance of about 90% of the surface irradiance represented interactions with 5–10 synthetic particles, in good agreement with observations about iridocyte numbers and number density in the natural clam system. Therefore, in addition to replicating the single-scattering behavior of individual natural iridocytes, our synthetic iridocytes also seem to reproduce the salient features of the natural system in layers where a few scattering events are possible. This effect was also observed in films with synthetic iridocytes made of constituent NPs of different sizes (**Figure 3.7**).

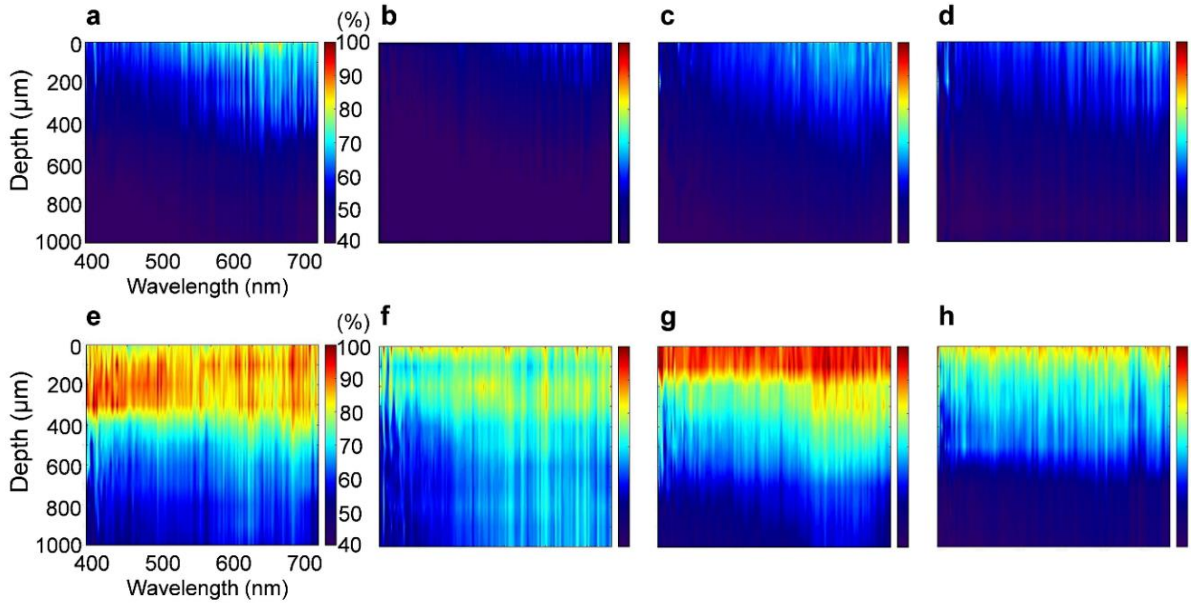

Figure 3.7 Measured intra-film radiometry data. The ratio of the scalar irradiance intensity at various depths from silica NPs (a-d) and synthetic iridocytes (e-h), all embedded in the gelatin films. Silica NPs are 120 nm (a, e), 200 nm (b, f), 250 nm (c, g), and 300 nm (d, h), respectively. All data were normalized by the intensity measured at the top surface of each sample.

3.4 Conclusions

Experimental characterizations of the particle phase functions and transmittance showed that these synthetic iridocytes had a somewhat broader angular distribution of scattering in the forward direction than that of the isolated nanoparticles, but the scattering was less broad than a multiple-scattering film consisting of the same particles. The back-scattering intensity was reduced to less than ≈0.01 % of the forward-scattered intensity, such that there would be little loss of light from these particles when incorporated into a photo-conversion technology, which is not possible by other types of forward scatters reported in the literatures.[3-5] The NPs assembled within the composite microspheres showed color in the backscattered direction dependent on the size of the constituent NPs, such that in a device, loss to the backscatter direction could be minimized by tuning it to regions where the photo-conversion technology is otherwise inefficient, as seen in the giant clams.[2] Further, our intra-film radiometry data showed that in a diffuse layer, a few scattering events from our synthetic particles recreated the forward redistribution of light observed within the clams among the organized pillars of microalgae. Our study including Chapter 2 and Chapter 3 presents a theoretically grounded engineering approach and experimental realization of optical components that allow efficient control and distribution of flux entering devices for solar photoconversion.

3.5 References

[1] H.-N. Kim, S. Vahidinia, A. L. Holt, A. M. Sweeney, S. Yang, *Advanced Materials* **2017**, *29*, 1702922.

[2] A. L. Holt, S. Vahidinia, Y. L. Gagnon, D. E. Morse, A. M. Sweeney, *J. R. Soc. Interface* **2014**, *11*, 20140678.

[3] S. W. Baek, J. Noh, C. H. Lee, B. Kim, M. K. Seo, J. Y. Lee, *Sci. Rep.* **2013**, *3*, 1726.

[4] W. Liu, J. F. Zhang, B. Lei, H. T. Ma, W. K. Xie, H. J. Hu, *Opt. Express* **2014**, *22*, 16178.

[5] Z. H. Wang, N. An, F. Shen, H. P. Zhou, Y. X. Sun, Z. N. Jiang, Y. H. Han, Y. Li, Z. Y. Guo, *Nanoscale Res. Lett.* **2017**, *12*, 8.

CHAPTER 4. Design and fabrication of wrinkle-silica composite films for multi-state and on-demand optical transmittance in smart window applications

Adapted from:

Kim, H.-N., Ge, D., Lee, E., and Yang, S.* (2018), Multistate and On-Demand Smart Windows. Adv. Mater., 2018, 30, 1803847.[1] Reproduced with permission.

4.1 Introduction

Windows play important roles in buildings, displays, and automobiles, determining light illumination, thermal insulation, aesthetics, noise insulation, and natural ventilation.[2-4] When there is excess solar gain or loss through the windows, energy consumption for heating, cooling, and lighting will also increase.[5, 6] As reported in 2012, heating and cooling in buildings account for approximately 14% of the total U.S. energy use.[7] Calculations suggest that more than 50% of the energy use for heating, cooling, and lighting could be reduced by deploying optimized glazing window systems.[7, 8] Hence, there has been much effort to develop dynamic (or active) "smart windows" that can be switched between transparent and opaque states through dynamic actuation of optically active materials. Switchable and tunable transparency is also very useful to other applications, e.g., flexible solar cells with patterned photoelectrodes,[9] wearable biosensors, or bendable medical devices. Smart windows include polymer dispersed liquid crystals (PDLCs),[10-12] suspended particles,[13] and chromogenic materials,[14-16] which switch in response to electrical,[17, 18] thermal,[19] chemical changes,[20] and light.[21] Recently, dynamic dimming windows based on reversible metal electrodeposition has been shown to have high contrast and excellent durability.[22] Nanocomposites from arrays of electrochromic tungsten oxide nanocrystals and amorphous niobium oxide glass show rapid, spectrally-selective tuning of light transmittance.[23] Nevertheless, active responsive windows often require complex processing steps, and more importantly, extra energy to automate the systems,[24, 25] thus lowering the overall energy efficiency of buildings. Therefore, new designs based on simple and low-cost materials are highly desirable.

Mechano-responsive smart windows composed of micro-wrinkles from elastomeric polymers[26-29] and particle embedded elastomer composites[30-32] with strain-dependent optical properties have been demonstrated, switching from a highly transparent state (> 90% transmittance in the visible region) to an opaque state (≤ 40% transmittance in the visible region).[26, 29] However, it typically requires the application of an appreciable mechanical strain (≥ 30%).

On-demand transmittance change (e.g., ≈50% in the visible wavelengths)[33] at a small strain (preferably 10% or less) is highly desired for window applications in vehicles, buildings, and roofing. Meanwhile, depending upon climate zones and window placement within a given built environment, end users will have the different preference for light transmittance or reflectance at the different time. In the case of office windows, the initial state should be transparent to let light in for illumination unless it becomes scorching hot inside or when privacy is needed. However, a resting opaque state would be preferred for a car window in a hot climate region to prevent overheating of cars in a parking lot, where temperatures could rise very quickly above 40 ˚C within a few minutes, leading to the hot-car causality of children.[34] When the vehicle is on the road, the opaque window should quickly turn into the transparent state, where ≈70-85% light transmittance in the visible region is considered sufficient.[33, 35]

4.2 Design of on-demand smart window films

In this study, we present a new strategy to create an on-demand smart window by harnessing the synergetic optical effects from the tunable geometry of wrinkles and nanovoids formed surrounding the silica particles embedded in a poly(dimethylsiloxane) (PDMS) film. By fine-tuning wrinkle formation, we can achieve different initial states: moderately transparent from 10% pre-strain film and highly opaque from 20% pre-strain film. By stretching the film above the pre-strain level by additional 10% and 30% strain, we observe ≈40% and ≈79.8% drop of transmittance at 550 nm, respectively.

It is known that wrinkles can be reversibly flattened and reinstated upon mechanical stretching and releasing. Wrinkled elastomers have been exploited for applications,[26, 27, 36, 37] including stretchable electrodes,[38] and tunable wetting and adhesion.[28, 29] Specifically, when the wrinkle wavelength is manipulated in the (sub)micron range, wrinkles act as Bragg gratings that reflect and scatter visible wavelength of light, thereby lowering the total amount of light transmitted through the substrates.[27] Wrinkles can be fabricated, for example, via oxygen plasma treatment of a pre-stretched elastomer film.[39] With the goal of decreasing the mechanical strain while maximizing the change of light transmittance in the visible to NIR region, we prepared a PDMS composite film, where a thin layer of quasi-amorphous array of silica NPs was embedded at the bottom of the film and wrinkles were created on the top of the film (see schematic in **Figure 4.1a-b**).

4.3 Experimental methods

4.3.1 Materials

Silica NPs (density = 2.1–2.2 g cm^{-3}) with various sizes (diameter = 200 nm, 250 nm, and 300 nm with coefficient of variation: < 10%, respectively) were purchased from General Engineering & Research (San Diego, CA, USA). 500 nm (in diameter) silica particles (density = 2.1–2.2 g cm^{-3}, 99.9%) and silica microparticles (diameter = 4080 nm, 1.8 g cc^{-1} with coefficient of variation = 2.7%) were purchased from Alfa Aesar (Haverhill, MA, USA) and Cospheric LLC (Santa Barbara, CA, USA), respectively. Sylgard 184 Elastomer Kit (Dow Corning Corp. Midland, MI) was used for preparing stretchable poly(dimethylsiloxane) (PDMS) composite films.

4.3.2 Preparation of PDMS-silica particle composite film

Silica NPs were dispersed in isopropyl alcohol (99.8%, Fisher Scientific, Inc.) at 10 wt% in a sonication bath (Bransonic™ CPX Series Ultrasonic Bath, Branson Ultrasonics) for 2 h. The NP solution was loaded into an airbrush with a nozzle size of 0.2 mm (Master Airbrush Model G44), and the operating pressure was 40 kPa.[32] The solution was sprayed for 20 s on the polystyrene (PS) petri dish at a spray distance of 10 cm and a moving speed of $\approx$ 10 cm s^{-1}. PDMS precursor solution was prepared by mixing Sylgard 184 silicone elastomer with a curing agent at a weight ratio of 10:1. The mixture was degassed in a vacuum desiccator for 40 min to remove air bubbles. The PDMS precursor mixture was then cast on the silica NPs-coated substrate and back-filled into the voids between the silica NPs. The overall thickness of the PDMS film was controlled to be 1 mm by adding 7 g of precursor solution into a petri dish (diameter of 10 cm). The whole sample was then cured in an oven at 65 °C for 4 h. Finally, the composite film was carefully peeled from the petri dish to prepare a stretchable free-stranding film.

4.3.3 Fabrication of wrinkled PDMS films

The free-standing PDMS films were cut into 4 cm x 1 cm rectangle, then loaded onto the custom-built stretcher. The films were pre-stretched by 10 or 20% of mechanical strain (pre-strain) depending on samples and placed into Technics Series 800 RIE (Oxygen Plasma Asher) at the fixed distance (≈ 7 cm) for 1 min (power: 50 W, O_2 pressure: 0.2 Torr) to generate a thin hard SiOx layer on the surface. Upon gentle releasing of film, wrinkle patterns were created on the surface. The wavelength and amplitude of the wrinkles were varied by using different oxygen plasma conditions and pre-strains.

4.3.4 Characterization

SEM images of PDMS film surfaces under various applied strains were imaged by FEI Quanta 600 environmental scanning electron microscope (ESEM) at an acceleration voltage of 5-10 kV coupled with the custom-built stretcher. Surface morphologies and height profiles of wrinkle-silica composite films were measured by using atomic force microscopy (AFM) (Bruker Icon) in tapping mode. The normal and the angle-dependent transmittance of the smart windows at various strains were measured using the Cary 5000 UV–vis–NIR spectrophotometer (Agilent Technologies) coupled with the custom-built stretcher. Fujifilm INSTAX Mini 8 Instant Camera (Fujifilm) was used for the polaroid photo images. The same custom-built stretcher was used to stretch the films and the whole setup, including the stretcher and the film, was attached to the camera lens in parallel. The particle-embedded surface of the film was facing towards the camera lens. We used a polaroid camera at a constant light condition (i.e., indoor light mode on the camera) to take the images without using any additional light source.

4.4 Fabrication of on-demand smart window films

First, silica NPs dispersed in isopropyl alcohol were spray coated onto a polystyrene substrate (thickness of silica layer, ≈5 μm) according to literature,[32] followed by infiltration of PDMS precursor and curing, thereby creating a free-standing NPs-embedded film (overall film thickness, ≈1 mm). The film was then pre-stretched to a certain level, followed by oxygen plasma with different powers. When the film was gently released,[40, 41] wrinkles were generated as shown in scanning electron microscopy (SEM) images, **Figure 4.1b** (left), with a wavelength of a few microns and an amplitude of hundreds of nanometers (**Figure 4.1c**) as measured by atomic force microscopy (AFM). The right image in Figure 1b shows that the NPs embedded in PDMS were packed in a quasi-amorphous array with short-range ordering in agreement with our previous observation.[32] Since the refractive index of PDMS (1.425 at 632.8 nm)[42] is very close to that of silica (1.457 at 632.8 nm),[43] the silica NPs-embedded PDMS film (wrinkle-free) is highly transparent in the visible wavelength range. In the case of the wrinkle-silica nanoparticle (NP) composite film, the optical transmittance of the initial, non-stretched state is dominated by the diffraction of light from the wrinkled surface. The film in the left image of **Figure 4.1d** shows rather high transparency from wrinkles prepared from a small pre-strain (10%). Upon stretching, the wrinkle is flattened, and the film becomes thinner and more transparent when the stretching strain is approaching the pre-strain. However, further stretching the composite film beyond the pre-strain make the film opaque. At 40% strain, the film becomes completely opaque.

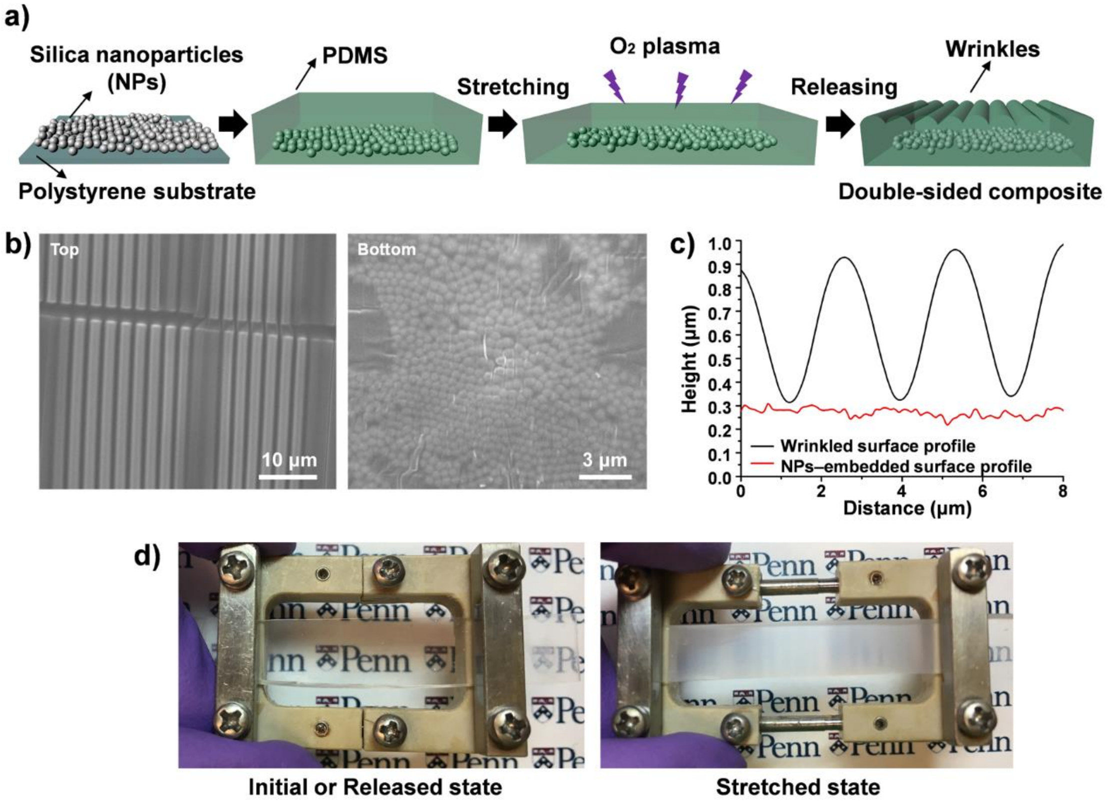

Figure 4.1 Overview of wrinkle-silica particle composite film. a) Schematic illustration of the procedure to prepare the wrinkle-silica composite films. b) SEM images of the top and bottom surfaces of the wrinkle-silica composite film with embedded 500 nm-sized silica NPs. c) AFM height profiles of the wrinkled surface and NPs-embedded surface of the composite film at released state. d) Photographic images of a wrinkle-silica composite film prepared from silica NPs with diameters of 200 nm at the initial or released state (left) and stretched state (right) with 40% of strain, respectively (oxygen plasma: 100 W for 1 min for all samples).

4.5 Mechanism

To understand the mechanism of the optical changes, we carefully characterized the change of the optical transmittance and the corresponding morphology at each side of the composite film upon stretching (**Figure 4.2**). Since our goal was to manipulate the visible to near infrared (NIR) optical transmittance, we embedded silica NPs with a diameter of 200 nm first. The one-dimensional (1D) wrinkles are formed in the direction perpendicular to the pre-stretch direction. Since transmittance is the highest when the wrinkles are stretched nearly flattened at the pre-strain level, maximizing the highest transmittance at the pre-strain will allow us to broaden the tunable range of the optical properties while keeping the strain level low. To do so, we prepare shallow wrinkles using a relatively low power of oxygen plasma (50 W) to treat the pre-stretched (pre-strain of 10%) PDMS film for a short duration (1 min), followed by releasing it. Wrinkles with the wavelength of ≈2.3 μm and amplitude of ≈190 nm are obtained (see **Figure 4.3a**). Increasing oxygen plasma treatment would increase wrinkle amplitude, leading to a blue shift of transmittance spectra, making it difficult to exhibit the scattering effect of silica NPs in the visible range. Therefore, we kept the oxygen plasma treatment time short.

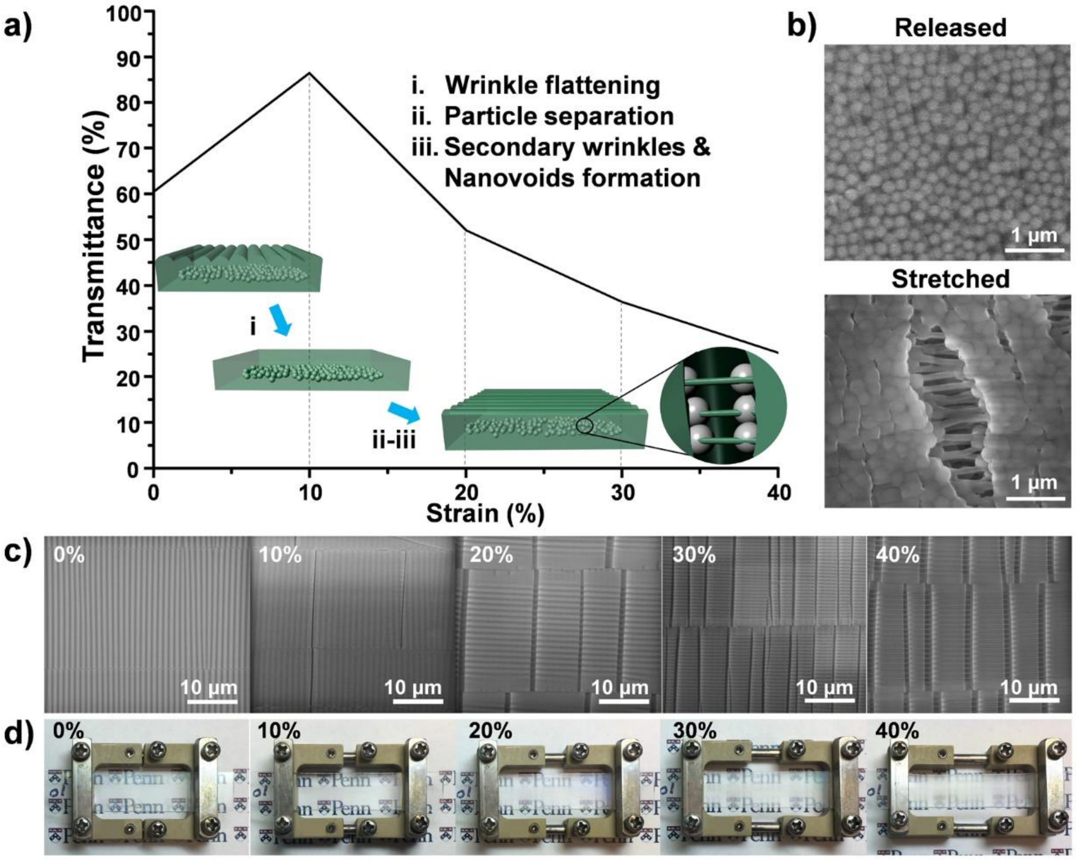

Figure 4.2 Tunable optical transmittance (%) at λ = 550 nm and surface morphologies of wrinkle-silica NP (diameter, 200 nm) composite film. The thickness of the silica layer is ≈5 µm, and the overall film thickness of the free-standing NPs-embedded films is ≈1 mm. a) Normal transmittance of wrinkle-silica NP composite film (pre-strain: 10%) at a wavelength of 550 nm as a function of the strain (0-40%). b) SEM image of NPs at the bottom of the PDMS film in the released state (top panel) and stretched state with 40% of strain (bottom panel). c) SEM images (wrinkle-side) of the wrinkle-silica NP (diameter, 200 nm) composite film prepared from 10% pre-strain and stretched at different applied strains (0-40%). d) Photograph images of the composite film at different applied strains (0-40%). All samples are treated with oxygen plasma at 50 W for 1 min.

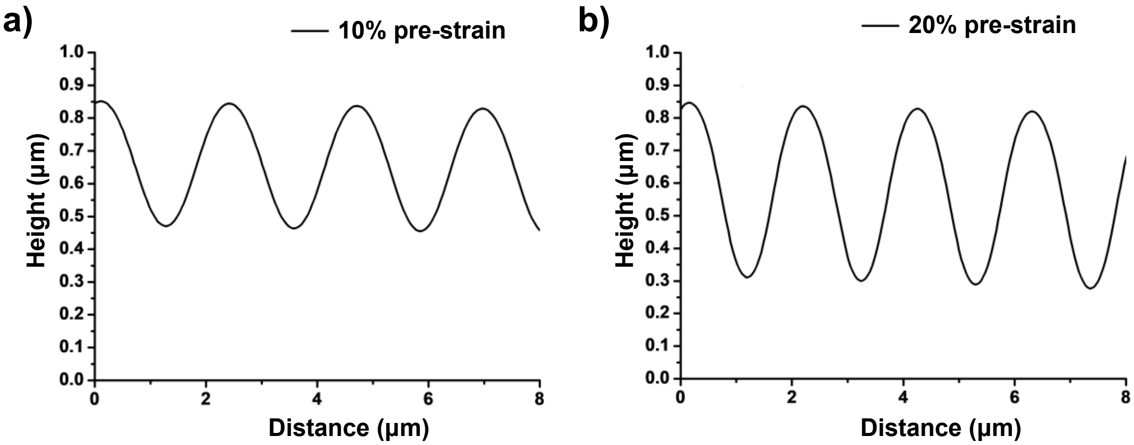

Figure 4.3 AFM scanning height profiles of wrinkle-silica NP (200 nm in diameter) composite films measured at different applied strains (0-40%). The composite films were prepared by pre-stretching the composite film at 10% (a) and 20% (b) strains, respectively, followed by oxygen plasma at 50 W for 1 min and release of the film.

4.6 Results and discussion

We measured the normal transmittance of the composite film using UV-vis-NIR spectrometer (see **Figure 4.2**a). At 0% strain, the film has 60.5% transmittance at a wavelength (λ) of 550 nm due to the light diffraction from the initial wrinkles. Upon stretching, up to the pre-strain level (10%), the maximum transmittance (86.4%) is obtained at 550 nm. As seen in **Figure 4.2a**, NPs became gradually separated from each other upon stretching (0-20% strain), resulting in the formation of nanovoids surrounding NPs, which acted as physical confinement to guide the crack formation. When stretching strain was >20% (see **Figure 4.2b**), the film became increasing opaque due to the increased scattering from the nanovoids. Meanwhile, secondary wrinkles began to form on the top surface (see **Figure 4.2c**) above the pre-stain (10%) as a result of the large Poisson's ratio of PDMS (≈0.5),[27] generating further diffraction and scattering. The secondary wrinkles and microcracks formed along the direction perpendicular to the wrinkles induce Mie scattering at the interface. Consequently, a large decrease of transmittance, from 86.4% at 10% strain to 52.1% at 20% strain, is exhibited with an overall change of strain of 10%, and significantly low normal transmittance of the film (25.2%) is achieved with additional 30% strain (i.e., at 40% strain level) due to the combined effect of scattering from the secondary wrinkles and/or microcracks and from nanovoids around NPs. Figure 2d shows the photos of wrinkle-silica NP composite films (10% pre-strain and 200 nm silica NPs) stretched at different applied strains (0-40%). As expected, the film is most transparent at 10% strain (i.e., at the pre-strain level), but becomes opaque as the applied strain further increases.

To demonstrate on-demand smart window performance, we prepared shallow wrinkles of two different geometries (**Figure 4.4a-b**). AFM profiles (**Figure 4.3**) and SEM images (**Figure 4.5**) show the comparison of wrinkles prepared from two different pre-strains (10% and 20%, respectively) at the same oxygen plasma treatment condition (50 W, 1 min). Wrinkled films generated from 10% pre-strain have ≈2.3 μm wavelength and ≈190 nm amplitude (**Figure 4.3a**) and those from 20% pre-strain have ≈2.06 μm wavelength and ≈267 nm amplitude (**Figure 4.3b**). For 10% pre-strain films, the transmittance of the wrinkle-silica NP composite film (red line) is compared to that of wrinkle-only film and silica NPs-only film at various applied strains (0% to 40%). For both silica NPs-only films and wrinkle-silica NP composite films seen in Figure 3a-b, the size of silica NPs was kept the same (200 nm in diameter) to exclude the NP size effect. Depending on the window location and season, as well as users, requirements of their optical transmittance are varied. For instance, for office window applications, films with high transparency at the initial state for clear vision, and a large drop of transparency for privacy is preferred. In the case of the silica-only film, the high initial transmittance (91.9%) is exhibited at 550 nm and 0% strain. However, the transmittance drops rather gradually as the strain increases, leading to the narrow tuning range of transmittance: 42.1% drop from 91.9% to 53.2% as strain increases from 0% to 40%. In the case of the wrinkle-only film, the larger drop of transmittance (52.3%) is observed above the pre-strain (from 10% to 40%), which can be attributed to the increased diffraction from the secondary wrinkles. In comparison, our wrinkle-silica NP composite film with 10% pre-strain exhibits much larger transmittance change, 70.8% (from 86.4% to 25.2%) when the stretch strain is increased from 10% to 40% due to the synergetic effect from wrinkles and NPs. Even with only 10% of additional strain after the wrinkles are flattened, 39.7% of transmittance drop (from 86.4 to 52.1%) is obtained.

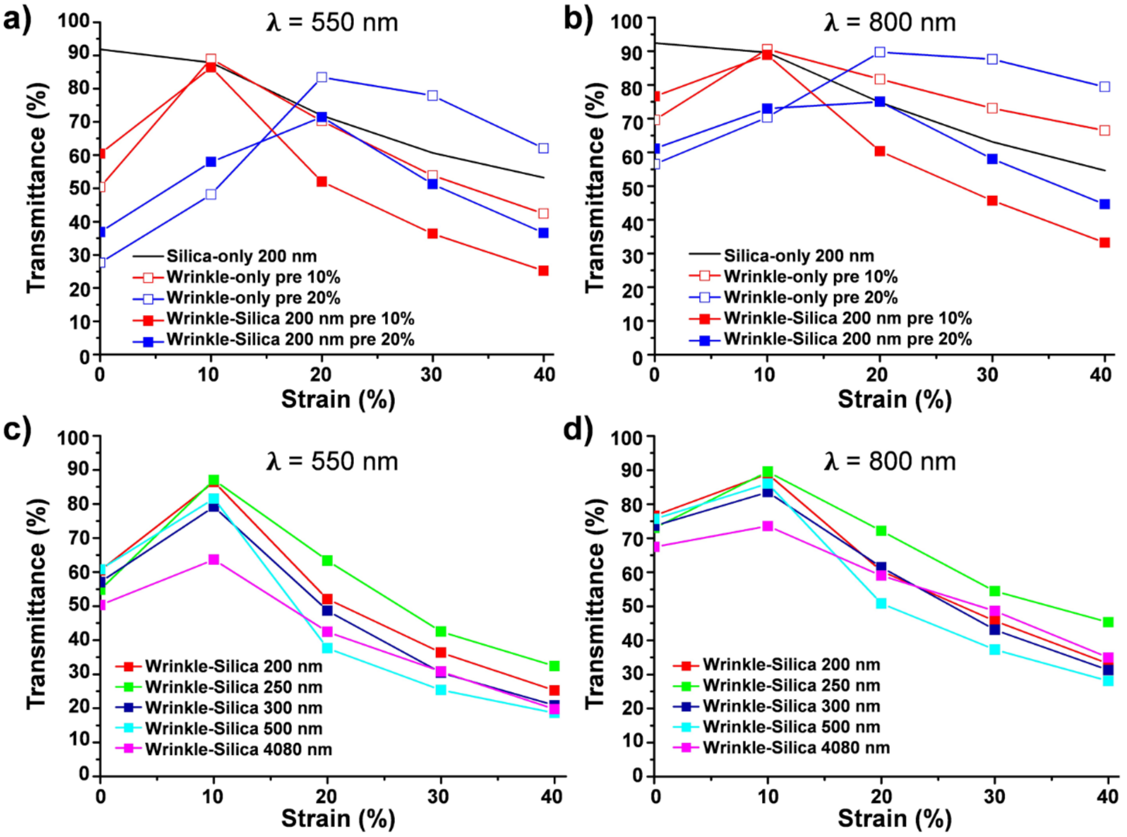

Figure 4.4 Optical transmittance of the wrinkle-silica particle composite films measured at a specific incident wavelength as a function of the applied strain (0-40%). a-b) Normal transmittance of wrinkle-silica NP (diameter, 200 nm) composite films (filled square) and wrinkle-only films (empty square) prepared with pre-strain of 10% (red lines) and 20% (blue lines) compared to silica-only film (black lines) at different applied strains (0-40%). All samples are treated with oxygen plasma at 50 W for 1 min. c-d) Normal transmittance of wrinkle-silica particle composite films prepared with pre-stretch strain of 10% (plasma: by 50 W for 1 min for all samples) composed of silica particles of variable sizes (diameter: 200 nm, 250 nm, 500 nm, and 4080 nm) at different applied strains (0-40%). (a) and (c) were measured at λ = 550 nm and (b) and (d) were measured at λ = 800 nm.

a) Pre-stretch strain, 10%

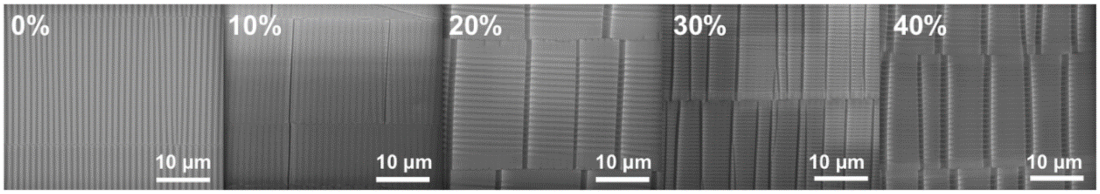

b) Pre-stretch strain, 20%

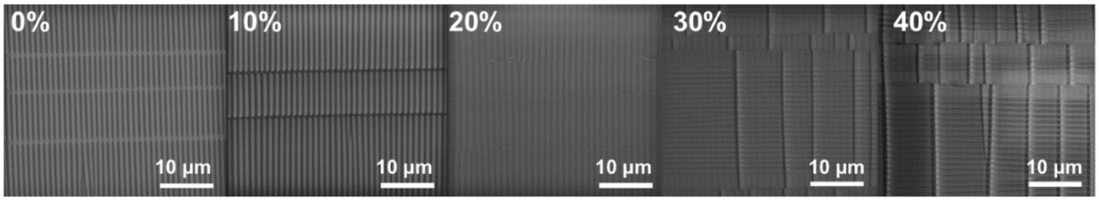

Figure 4.5 SEM images of wrinkle-silica NP (200 nm in diameter) composite films stretched at different applied strains (0-40%). The composite films were prepared with pre-strains of 10% (a) and 20% (b), respectively. All samples were prepared with oxygen plasma at 50 W for 1 min.

In the case of 20% pre-strained wrinkle-silica NP composite film, the initial film was moderately opaque due to diffraction from the initial wrinkles with a larger amplitude (see **Figure 4.6**). It reached the highest transparency when stretched at the pre-strain level, 20%, but became opaque as applied strain increased (20-40%), the same as the observation in the composite film with 10% pre-strain. The measured initial and the highest transmittance (occurred at the pre-strain, 20%) at 550 nm is 36.9% and 71.5%, respectively (**Figure 4.4a**), which may be suitable for uses that prefer a low transmittance in the initial state (e.g., for cars parked under the scorching sun).

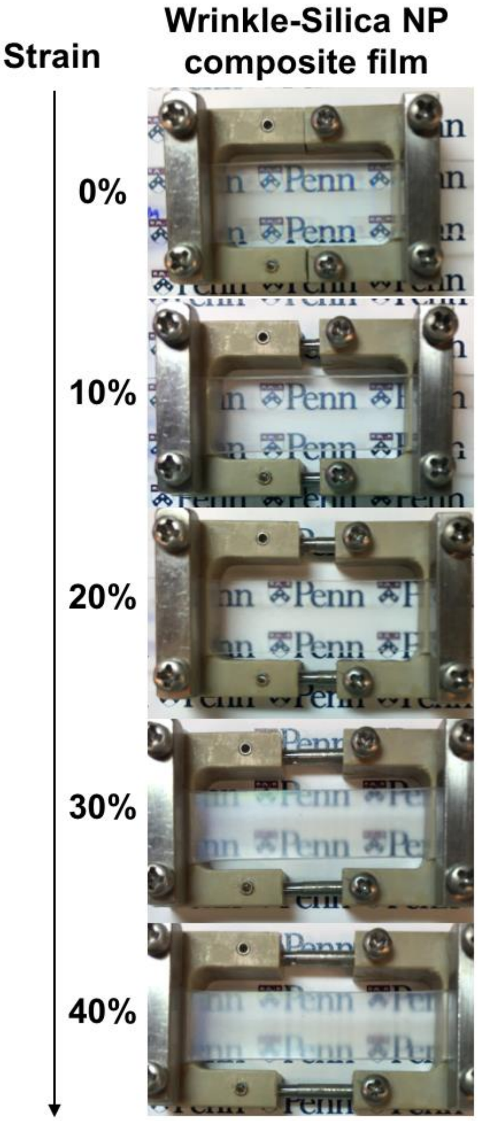

Figure 4.6 Photographs of a wrinkle-silica NP (200 nm in diameter) composite film prepared from 20% pre-strain and stretched at different applied strains (0-40%). The film is treated with 50 W oxygen plasma for 1 min.

The composite films exhibit very similar behaviors at NIR wavelength (λ = 800 nm), leading to a drastic transmittance drop upon stretching, which was not seen in silica NPs-only or wrinkle-only samples. When comparing **Figure 4.4a** and **Figure 4.4b**, wrinkle-silica NP composite films exhibited a larger transmittance drop at λ = 550 nm than those at λ = 800 nm. However, the silica NPs-only samples (diameter 200 nm) did not show the wavelength-dependent behavior (black lines from Figure 3a and 3b looks similar). Instead, wrinkle-only samples had lower transmittance at λ = 550 nm than that at λ = 800 nm when the wrinkles are not completely flattened due to the wavelength-dependent diffraction of light on the wrinkled surface. Therefore, the dip of transmittance in NIR should be attributed to the wrinkles, which could be further tuned by vary the geometry of the wrinkles or use larger silica particles.

To investigate particle size in controlling the optical behaviors of the composite films we used silica NPs of different diameters: 200 nm, 250 nm, 300 nm, 500 nm, and 4080 nm (**Figure 4.4c-d**). Compared to the smaller NPs, larger particle films exhibited further transmittance drop upon stretching because it is much easier to form voids around the larger particles that are more isolated from each other. When 4080 nm silica particles are introduced in the film, the maximum transmittance is decreased at both wavelengths, 550 nm (visible) and 800 nm (NIR) even at 10% of strain, possibly due to the much-increased scattering from the rapidly generated micro-scaled voids. Thus, we can exploit the interplay between the pre-strain of the wrinkles and particle size to further fine-tune the optical transmittance of films for different applications.

4.7 Further results and discussion

For practical applications in buildings and automotive vehicles, angle-dependent transparency needs to be considered. Here, we measured the angle-dependent light transmittance of 20% pre-strained wrinkle-silica NP (diameter, 200 nm) composite film as shown in **Figure 4.7**. The angle of incidence (α) was varied from 0 to 30° by tilting the sample stage (see **Figure 4.7a**), and the transmittance was measured at an angle, $\beta = \alpha$, while the film was stretched up to 40% strain using a custom-built stretcher. As seen in **Figure 4.7b**, the transmittance is nearly unchanged at different angles of incidence except at the applied strain of 0% and 40%, where the transmittance decreases rather obviously but no more than 10% as α changes from 0 to 30°. We believe this is because all the wrinkles prepared in our system are very shallow (amplitude on the order of hundreds of nm); the amplitude of the initial wrinkles is the largest at 0% strain, and secondary wrinkles begin to appear above the pre-stain, which is 20% here. The intensity of the diffracted light from the curved wrinkle surfaces seems to increase as α is increased. However, the overall change in transmittance with α is not large.

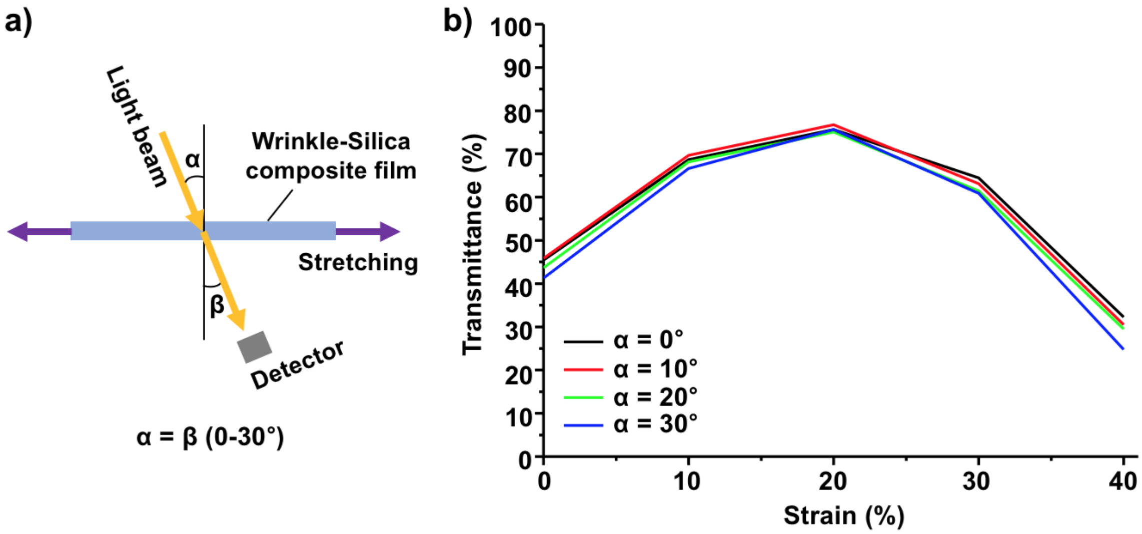

Figure 4.7 a) Schematic illustration of the experimental setup for measuring the angular dependence of transmittance. b) Transmittance of the wrinkle-silica NP composite film (pre-strain: 20%) at a wavelength of 500 nm as a function of the strain (0-40%). The film is treated with 50 W oxygen plasma for 1 min.

Finally, to illustrate the application of our smart window films, we captured images on photographic paper using a polaroid camera and imaged through our composite film (See **Figure 4.8a**). Released or stretched composite films are attached to the lens of polaroid camera, respectively. Here, the same sample used in **Figure 4.2** (10% pre-strain and 200 nm silica NPs) was selected. The photographic images of the object (baby dolls) are taken at a fixed distance between the object and the lens. As seen in **Figure 4.8b-c**, a fairly clear photo is formed from the released (or initial state) composite film. This is not the case from highly stretched (40% strain) composite film, where the image of baby dolls is very fuzzy. This means when the composite film is used as a window, most of the visible to NIR light will be blocked.

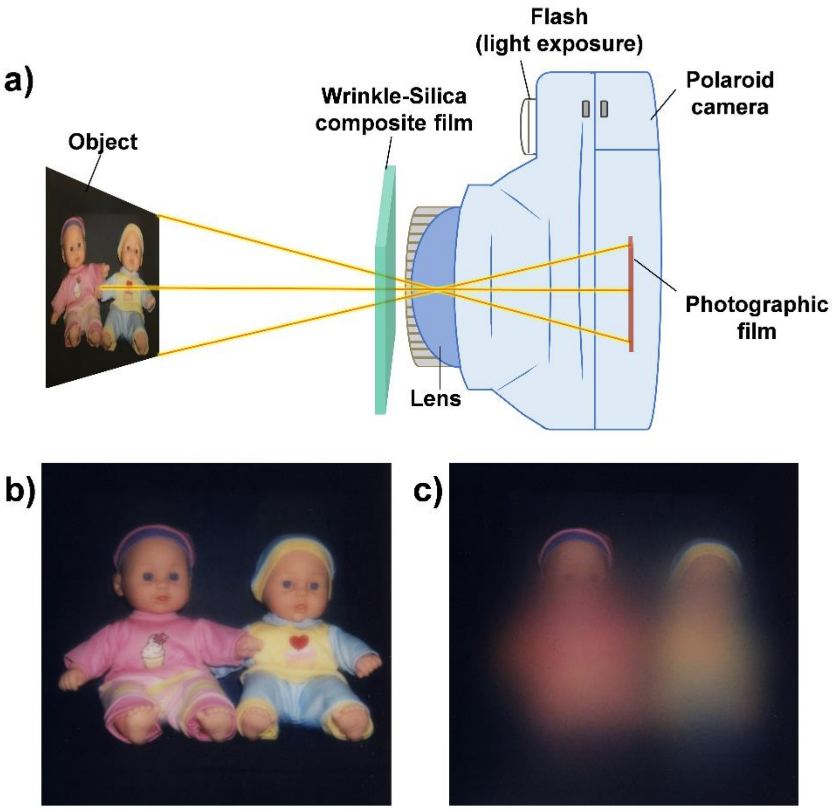

Released film

Stretched film

Figure 4.8 Photos obtained by imaging objects (here, baby dolls) through the smart window films. a) Schematic illustration of the photographic film experiment. Films were loaded onto the lens of polaroid camera and pictures of objectives (baby doll toys) were taken by using the camera setup with coupled film (distance from objectives to the lens: 70 cm). b-c) Photographic films developed by the light transmitted through the film. (b) Released wrinkle-silica NP (diameter, 200 nm) composite film and (c) stretched wrinkle-silica NP (diameter, 200 nm) composite film at 40% strain. The wrinkle-silica NP composite sample was prepared from oxygen plasma at 50 W for 1 min.

4.8 Conclusions

In summary, we have demonstrated multistate smart windows from composite PDMS films, consisting of wrinkles on top of the surface and silica particles embedded at the bottom. By carefully varying the wrinkle geometry, silica particle size, and stretching strain, we achieve different initial optical states and the large degree of optical transmittance change in the visible to NIR range with a relatively small strain (as small as 10%). For applications that prefer high resting transparency such as office and building windows in cold/cloudy climate zones, we create shallow wrinkles with a low amplitude from the sample with 10% pre-strain, showing moderate transmittance (60.5%) initially and the highest transmittance of 86.4% at 550 nm when stretched to the pre-strain level. Further stretching leads to the drastic decrease of the transmittance at 550 nm, 39.7% and 70.8% with an additional 10% and 30% strain, respectively. The large drop of optical transmittance is the result of combined effects from the formation of secondary wrinkles (and/or microcracks) and nanovoids generated around the particles. For applications that require comparatively low transmittance in the initial state, such as car and building windows in hot climate zones, we create wrinkles with a moderate amplitude from the sample with 20% pre-strain, showing 36.9% transmittance at 550 nm in the initial state. The highest transmittance of 71.5% at 550 nm is achieved when stretched to the pre-strain level. Further stretching also leads to increased opacity similar to the observation from the 10% pre-strain sample. Our method of preparing mechanically tunable composite films is simple, yet it achieves an appreciable tunable range of optical transparency with different initial states. The smart window film can be used as a Venetian blind-like window film installed onto the existing building windows or automotive windows with rollers or embedded in the window screen. They can be mechanically stretched either manually or electrically. For the former, it will not require any change of existing window designs; if embedded, it will require an entirely new design to fit into existing window frame with motors, which will be more costly. By varying wrinkle geometries and silica particle size, we could further improve the tunable range and lower the applied strain levels for on-demand smart window applications in different climate settings. The combination of NPs and wrinkles to maximize optical switching without the use of a large mechanical strain will offer new insights to improve energy efficiency in next-generation smart buildings and automobiles.

4.9 References

[1] H.-N. Kim, D. Ge, E. Lee, S. Yang, *Advanced Materials* **2018**, *30*, 1803847.

[2] C. F. Gao, W. L. Lee, *Build. Environ.* **2011**, 46, 961

[3] Y. H. Lin, K. T. Tsai, M. D. Lin, M. D. Yang, *Appl. Energy* **2016**, *171*, 336.

[4] M. A. Hassan, N. M. Guirguis, M. R. Shaalan, K. M. El-Shazly, *Desalination* **2007**, *209*, 251.

[5] W. J. Hee, M. A. Alghoul, B. Bakhtyar, O. Elayeb, M. A. Shameri, M. S. Alrubaih, K. Sopian, *Renew. Sust. Energ. Rev.* **2015**, *42*, 323.

[6] C. J. Sun, H. Giles, Z. W. Lian, *Sol. Energy* **2014**, *102*, 1.

[7] N. DeForest, A. Shehabi, J. O'Donnell, G. Garcia, J. Greenblatt, E. S. Lee, S. Selkowitz, D. J. Milliron, *Building and Environment* **2015**, *89*, 107.

[8] H. Khandelwal, A. Schenning, M. G. Debije, *Advanced Energy Materials* **2017**, *7*, 1602209.

[9] F. Bella, A. Lamberti, S. Bianco, E. Tresso, C. Gerbaldi, C. F. Pirri, *Advanced Materials Technologies* **2016**, *1*, 1600002.

[10] D. Cupelli, F. P. Nicoletta, S. Manfredi, M. Vivacqua, P. Formoso, G. De Filpo, G. Chidichimo, *Solar Energy Materials and Solar Cells* **2009**, *93*, 2008.

[11] S. M. Guo, X. Liang, C. H. Zhang, M. Chen, C. Shen, L. Y. Zhang, X. Yuan, B. F. He, H. Yang, *ACS Appl. Mater. Interfaces* **2017**, *9*, 2942.

[12] M. Kim, K. J. Park, S. Seok, J. M. Ok, H. T. Jung, J. Choe, D. H. Kim, *ACS Appl. Mater. Interfaces* **2015**, *7*, 17904.

[13] R. Vergaz, J. M. Sanchez-Pena, D. Barrios, C. Vazquez, P. Contreras-Lallana, *Solar Energy Materials and Solar Cells* **2008**, *92,* 1483.

[14] C. G. Granqvist, *Thin Solid Films* **2014**, *564*, 1.

[15] C. G. Granqvist, *Solar Energy Materials and Solar Cells* **2000**, *60*, 201.

[16] C. Bechinger, S. Ferrer, A. Zaban, J. Sprague, B. A. Gregg, *Nature* **1996**, *383*, 608.

[17] A. L. Dyer, C. R. G. Grenier, J. R. Reynolds, *Adv. Funct. Mater.* **2007**, *17*, 1480.

[18] K. A. Gesheva, T. M. Ivanova, G. Bodurov, *Prog. Org. Coat.* **2012**, *74*, 635.

[19] M. Kamalisarvestani, R. Saidur, S. Mekhilef, F. S. Javadi, *Renew. Sust. Energ. Rev.* **2013**, *26*, 353.

[20] K. H. Zhang, M. M. Zhang, X. L. Feng, M. A. Hempenius, G. J. Vancso, *Adv. Funct. Mater.* **2017**, *27*, 1702784.

[21] L. Y. L. Wu, Q. Zhao, H. Huang, R. J. Lim, *Surf. Coat. Technol.* **2017**, *320*, 601.

[22] C. J. Barile, D. J. Slotcavage, J. Hou, M. T. Strand, T. S. Hernandez, M. D. McGehee, *Joule* **2017**, *1*, 133.

[23] J. Kim, G. K. Ong, Y. Wang, G. LeBlanc, T. E. Williams, T. M. Mattox, B. A. Helms, D. J. Milliron, *Nano Lett.* **2015**, *15*, 5574.

[24] Making Smart Windows that Are Also Cheap, https://www.technologyreview.com/s/420221/making-smart-windows-that-are-also-cheap/ (accessed: March 2018).

[25] Preliminary Assessment of the Energy-Saving Potential of Electrochromic Windows in Residential Buildings, https://www.nrel.gov/docs/fy10osti/46916.pdf (accessed: March 2018).

[26] Z. W. Li, Y. Zhai, Y. Wang, G. M. Wendland, X. B. Yin, J. L. Xiao, *Adv. Opt. Mater.* **2017**, *5*, 7.

[27] P. Kim, Y. H. Hu, J. Alvarenga, M. Kolle, Z. G. Suo, J. Aizenberg, *Adv. Opt. Mater.* **2013**, *1*, 381.

[28] G. J. Lin, P. Chandrasekaran, C. J. Lv, Q. T. Zhang, Y. C. Tang, L. Han, J. Yin, *ACS Appl. Mater. Interfaces* **2017**, *9*, 26510.

[29] S. G. Lee, D. Y. Lee, H. S. Lim, D. H. Lee, S. Lee, K. Cho, *Advanced Materials* **2010**, *22*, 5013.

[30] K. W. Jun, J. N. Kim, J. Y. Jung, I. K. Oh, *Micromachines* **2017**, *8*, 7.

[31] M. Shrestha, G. K. Lau, *Opt. Lett.* **2016**, *41*, 4433.

[32] D. T. Ge, E. Lee, L. L. Yang, Y. G. Cho, M. Li, D. S. Gianola, S. Yang, *Advanced Materials* **2015**, *27*, 2489.

[33] M. Freedman, P. Zador, L. Staplin, *Hum. Factors* **1993**, *35*, 535.

[34] Hot car deaths reach record numbers in July, https://www.cnn.com/2017/08/01/health/hot-car-deaths/index.html (accessed: March 2018).

[35] N. R. Burns, T. Nettelbeck, M. White, J. Willson, *Ergonomics* **1999**, *42*, 428.

[36] T. Ohzono, K. Suzuki, T. Yamaguchi, N. Fukuda, *Adv. Opt. Mater.* **2013**, *1*, 374.

[37] P. Goel, S. Kumar, J. Sarkar, J. P. Singh, *ACS Appl. Mater. Interfaces* **2015**, *7*, 8419.

[38] J. Tang, H. Guo, M. M. Zhao, J. T. Yang, D. Tsoukalas, B. Z. Zhang, J. Liu, C. Y. Xue, W. D. Zhang, *Sci Rep* **2015**, *5*, 16527.

[39] P. C. Lin, S. Yang, *Appl. Phys. Lett.* **2007**, *90*, 241903.

[40] E. Cerda, L. Mahadevan, *Phys. Rev. Lett.* **2003**, *90*, 074302.

[41] J. Genzer, J. Groenewold, *Soft Matter* **2006**, *2*, 310.

[42] K. Raman, T. R. S. Murthy, G. M. Hegde, *Physics Procedia* **2011**, *19*, 146.

[43] B. Brixner, *Journal of the Optical Society of America* **1967**, *57*, 674.

CHAPTER 5. Fabrication of particle-embedded wrinkling patterns for tunable mechano-responsive optical transmittance

Kim, H.-N., Ge, D., Lee, E., and Yang, S.* (2018), "Fabrication of Particle-Embedded Wrinkling Patterns for Tunable Mechano-Responsive Optical Transmittance", Manuscript in preparation.

5.1 Introduction

Mechano-responsive optical materials are promising for light-modulating applications, including smart windows,[1, 2], data recording,[3] color displayers,[4] and stress-strain sensors[5]. Approaches based on nano- and micro-structured elastomers, including micro-holes arrays,[6] micro- and nanopillar arrays,[7, 8] and microprism arrays[9], have been extensively explored recently.[10-13] These systems are typically opaque in the initial state attributed to the light scattering from the micro- and nanostructures, and their transparency increases monotonically under the mechanical deformation e.g., by stretching or compressing. We and others have created composite material systems that are transparent in the initial state and turn to opaque in the deformed state by generating nanovoids surrounding silica nanoparticles (NPs) embedded in a polydimethylsiloxane (PDMS) film[11] or tuning the direction of aluminum micro-platelets in PDMS.[14] Nevertheless, the change of transparency in these systems remains monotonic. Therefore, in practical applications such as strain sensors, it would not be convenient to use such materials to assess the level of mechanical strain for a given degree of transmittance. Band-pass optical filters that can transmit only a certain intensity band while blocking others have been commonly used for signal processing, allowing for a programmable and non-monotonic change of intensity.[15] The concept of band-pass filters can be used in the mechano-optical materials to determine the peak positions for calibration purpose. Diffraction grating effect from the surface of wrinkled PDMS films[5, 10, 14, 16] have been investigated for dynamic and on-demand tuning of the optical transmittance by stretching/releasing wrinkles at different strain levels.

Periodically ordered wrinkles can be easily fabricated in PDMS by treating a pre-strained film with oxygen plasma or UV-ozonolysis, followed by release of the strain.[17, 18] A thin hard silica-like layer formed on top of the elastomer PDMS film causes a mismatch in elastic moduli at the skin layer-PDMS interface, leading to wrinkle formation to relax the compressive strain. In a bilayer, to balance the elastic strain energy, wrinkling relaxes the compressive strain in the thin hard layer, thus reducing the elastic strain energy. At the same time, it bends the thin layer, which increases the bending energy. Based on linear buckling theory, where the reduced elastic energy upon wrinkling is balanced out by the increase of bending energy, and assuming the underlying substrate is semi-infinite large compared to the top thin layer, the governing equations for wrinkle dimensions can be expressed as,[19]

$$\lambda = 2\pi t_h \left(\frac{\bar{E}_h}{3\bar{E}_S}\right)^{1/3} \tag{5-1}$$

$$A = t_h \left(\frac{\varepsilon}{\varepsilon_c} - 1\right)^{1/2} \tag{5-2}$$

$$\varepsilon_c = \frac{1}{4}\left(\frac{3\overline{E}_s}{\overline{E}_h}\right)^{2/3} \tag{5-3}$$

$$\text{where } \overline{E} = E/(1-\nu^2) \tag{5-4}$$

Here, λ is the wavelength of the wrinkles, t is the film thickness, E is the Young's modulus, ν is the Poisson's ratio of the substrate (ν=1/2 for PDMS), A is the amplitude of the wrinkles, ε is the applied strain, ε_c is the critical strain for buckling to occur. The subscripts h refers to the top hard layer and s refers to the underlying substrate. The thickness and modulus of the silica-like layer, and therefore the wrinkle dimensions depend on the power and exposure time of oxygen plasma treatment. Therefore, wrinkled PDMS films have been exploited for reversible switching optical properties,[10] wetting,[16] adhesion,[20] anti-biofouling for applications[21] including flexible electronic devices,[22, 23] microlens arrays,[24, 25] smart windows,[8, 11] photovoltaics, and pressure sensors.[26] When the wrinkled film is overstretched beyond the pre-strain, while the initial wrinkles are flattened, the secondary wrinkles are generated along the stretching direction,[10] creating a broad peak in the transmittance-strain curve.

Nevertheless, highly ordered wrinkles have their own limitations as mechano-responsive optical materials because: 1) The angle-dependent diffraction grating effect leads to multi-colors and inhomogeneous optical transmittance. 2) The change of transmittance as a function of the applied mechanical strain is gradual not in a narrow bandwidth. As presented in Chapter 4, we have recently achieved non-monotonic switching between transparency and opacity with a rather small mechanical strain (≈10%) by incorporating wrinkles on the top surface of the PDMS film while silica NPs are embedded at the bottom of the film.[27] The achievement of large degree of transmittance change addresses the third limitation listed above. Yet it remains to improve the uniformity of optical transmittance in different viewing angles and random formation of lateral cracks. The nanovoids in the previous composite film is gradually initiated at 0-20% strains regardless of the wrinkle flattening process,[27] and thus the maximum transmittance cannot always be observed when the applied strain approaches the pre-strain level in the case of wrinkles prepared from pre-strains greater than 20%. This is because the generation of microcracks and nanovoids around NPs embedded at the bottom side of the film already occurred at 10-20% of applied strain. Thus, further stretching beyond 20% strain will reduce the transmittance instead. Thus, it remains a significant challenge to develop an effective strategy for preparing mechano-responsive wrinkling patterns that will not only have a large optical modulation range but also offer programmable transmittance vs. strain for sensor applications.

Building upon the study in Chapter 4, here we fabricate silica NP/wrinkle films with wrinkles generated on the surface embedded with NPs to allow generation of nanovoids after the wrinkle flattening is completed. Meanwhile, we expect less-ordered wrinkles will be formed due to the presence of hard silica NPs on the top surface, thereby achieving more uniform optical transmittance by enhancing diffusive scattering whiling reducing the angle-dependent diffraction grating effect. First, we spay coat silica NPs on top of PDMS film, followed by pre-strain and oxygen plasma treatment to generate wrinkles. The presence of the NPs and the size of the particles can significantly affect the wrinkle formation. For example, small-sized NPs tend to dissipate the compressive stress in the film generated by the mismatch of elasticity between oxygen plasma generated silica and PDMS. Meanwhile, the mismatch of elastic modulus between silica NPs and PDMS can also cause surface buckling. The presence of NPs in PDMS will also increase the overall elastic modulus of the composite film, further complicating the wrinkle generation. In this chapter, we detail the formation of quasi-ordered wrinkles and the resulting morphologies (amplitude and wavelength), formation of lateral cracks, and the orientation or uniformity of the resulting wrinkles. We find that particle-embedded wrinkling patterns exhibit amplitudes and wavelengths relatively larger than those obtained from PDMS-only films. Along the lines, we study that the presence of particles and their sizes to the formation of both initial and secondary wrinkles, the formation of lateral cracks, and the resulting optical transmittance of films.

Here, the quasi-ordered wrinkles on the silica NPs-embedded PDMS films enhance light scattering, leading to narrow band-pass in transmittance vs. strain. As the particles embedded in wrinkles can generate nanovoids around them beyond the pre-strain level, the transmittance-strain curve has a pre-determined peak. When the wrinkles are stretched before the pre-strain level, the generation of nanovoids is not yet initiated. Thus, the generation of nanovoids does not reduce the transmittance until the applied strain is increased to the pre-strain level, allowing for narrower transition peaks, which could be used in strain sensor applications as well as in dynamic light blocks for smart window applications. The narrow band-pass filters can also be useful in color displays.

5.2 Experimental methods

5.2.1 Materials

Silica NPs (density = 2.1–2.2 g cm^{-3}) of different sizes (diameter = 200 nm and 500 nm with coefficient of variation: < 10%, respectively) were purchased from General Engineering & Research (San Diego, CA, USA). 500 nm (in diameter) silica particles (density = 2.0 g cm^{-3}, 99.9%) and 1.0 µm (in diameter) silica particles (density = 2.0 g cm^{-3}, 99.9%) were purchased from Alfa Aesar (Haverhill, MA, USA). Isopropyl alcohol (99.8%) was purchased from Fisher Scientific, Inc. Sylgard 184 Elastomer Kit (Dow Corning Corp. Midland, MI) was used for preparing poly(dimethylsiloxane) (PDMS) elastomer composite films.

5.2.2 Preparation of particle-embedded PDMS composite film

Silica NPs were thoroughly dispersed in isopropyl alcohol at 10 wt% in a sonication bath (Bransonic™ CPX Series Ultrasonic Bath, Branson Ultrasonics) for 2 h. The NP solution was loaded into an airbrush with a nozzle size of 0.2 mm (Master Airbrush Model G44), and the operating pressure was 40 kPa.[11, 27] The solution was sprayed for 10 s on the polystyrene (PS) petri dish at a spray distance of 10 cm and a moving speed of ≈ 10 cm s^{-1}. The thickness of the silica layer was controlled to be ≈1 µm. The mixture of Sylgard 184 silicone elastomer and curing agent (at a weight ratio of 10:1) was used as a PDMS precursor solution. Subsequently, the mixture was degassed in a vacuum desiccator for 40 min to remove air bubbles. Then, we cast the PDMS precursor mixture on the silica NPs-coated substrate and back-filled it into the gaps between the silica NPs.[27] The overall thickness of the PDMS film was controlled to be 0.5 mm. The whole sample was then cured in an oven at 65 °C for 3 h. After the full curing, we gently peeled the composite film from the petri dish to prepare a stretchable free-stranding film.

5.2.3 Preparation of particle-wrinkled PDMS films

The free-standing PDMS films were cut into 5 cm x 1 cm rectangle, then loaded onto the custom-built stretcher. The films were pre-stretched (10-40%) and placed into the chamber of Technics Series 800 RIE (Oxygen Plasma Asher) at the fixed distance (≈ 7 cm) for 1 min (power: 100 W, O_2 pressure: 0.2 Torr) to generate a thin hard SiOx layer on the surface. While the film is released slowly, wrinkle patterns were created on the surface.

5.2.4 Characterization

SEM images of film surfaces under various applied strains were taken by field emission scanning electron microscope (FESEM, JEOL 7500F) and FEI Quanta 600 environmental scanning electron microscope (ESEM) at an acceleration voltage of 5-10 kV coupled with the custom-built stretcher. Surface morphologies and the height profiles of particle-embedded wrinkling patterns were characterized by using atomic force microscopy (AFM) (Bruker Icon) in tapping mode. The optical microscope images were taken by Olympus (BX 61) optical microscopy. The transmission spectra at various strains were measured at the normal direction to the membrane by the fiber optical spectrometer (USB4000, Ocean Optics) coupled with the custom-built stretcher. Photographic images for optical transparency and opacity of the films at various strains were taken under the light panel with a 5 mm-sized slit. A camera was placed at the center or slightly outside of the light beam to characterize the intensity of transmitted light or the resultant angle-dependent color changes. A custom-built stretcher was used for stretching the film during the characterization.

5.3 Results and discussion

As shown in **Figure 5.1a**, experimental conditions such as the power of plasma, plasma treatment time, and pre-stretch strain were controlled so that we could generate different wrinkle patterns with various geometries (amplitude and wavelength) of wrinkles. Here we embedded 200 nm-sized silica NPs in a PDMS film and pre-stretched the film at 30%, followed by 3 min oxygen plasma treatment (power: 100 W). Since the wrinkle patterns can be flattened and re-generated as the mechanical strain increases, optical transmittance of the composite film can be tuned at different applied strains as seen in the photo shown in **Figure 5.1b**. At the applied strain of 30%, the film exhibits the highest transparency since the particle-embedded wrinkles are nearly flattened, thereby decreasing the light diffraction and transmitting more of light through the film. Thus, the composite film undergoes changes from opaque to transparent, then to opaque again as the applied strain increases from 0% to 30% and from 30% to 40%.

5.3.1 Surface morphologies of particle-embedded wrinkling patterns

Diffraction of light caused by cracks (either aligned laterally to the stretching direction) and the wrinkled surface can be fine-tuned. Thus, the initial optical transmittance of the film can be varied accordingly. In **Figure 5.1c**, the scanning electron microscopy (SEM) image shows the morphology of particle-embedded wrinkling patterns at the initial state (0% strain). The surface of particle-embedded pattern seems to possess non-uniformly formed wrinkles with a quasi-amorphous array of particles on the surface with short-range ordering.

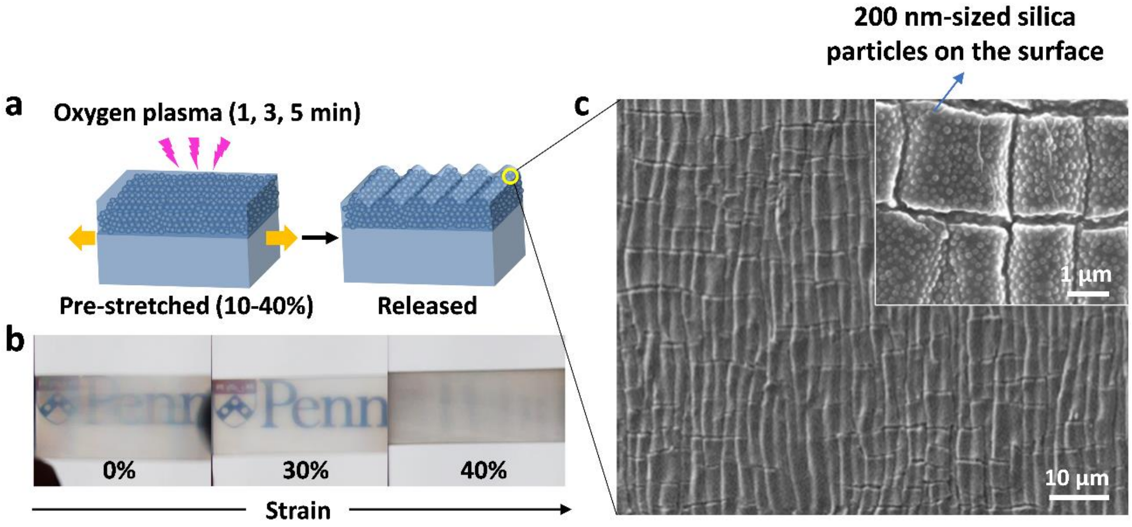

Figure 5.1 Wrinkle formation on the particle-embedded PDMS composite film. a) Schematic illustration of the procedure to prepare the particle-embedded wrinkling patterns. b) Photographs of the composite film at various applied strains consisting of particle-embedded wrinkling patterns on top prepared by embedding silica NPs with diameters of 200 nm and pre-stretching at 30%. c) SEM image of the top surface of the composite film seen in b) at the initial state. Oxygen plasma condition: 100 W for 3 min for all samples.

The surface topography of the wrinkle patterns is characterized by atomic force microscopy (AFM) (see **Figure 5.2a** and **Figure 5.2b)**. One pattern was prepared from the bare PDMS film ('wrinkle-only'), and the other one was prepared from the particle (diameter: 200 nm)-embedded PDMS surface ('wrinkle with 200 nm-silica'). The presence of silica particles (Young's modulus: ≈73 GPa)[28] on the surface increases the effective elastic modulus of the surface layer, subsequently affecting both the elastic modulus contrast between the particles and PDMS, and thus the critical strain of wrinkle formation. **Figure 5.2a** confirms that NPs could inhibit the formation of small-sized ordered wrinkles (wavelength, 1-3 μm) but rather create quasi-ordered and larger wrinkles with more lateral cracks, which was not seen in the wrinkle-only system. The height profiles in **Figure 5.2b** show that the amplitude of ‘wrinkle-only’ is ~400 nm, and the wavelength of it is ~3 µm. In the case of ‘wrinkle with 200 nm-silica’, the amplitude is ~800 nm-1 µm and the wavelength is ~8-10 µm.

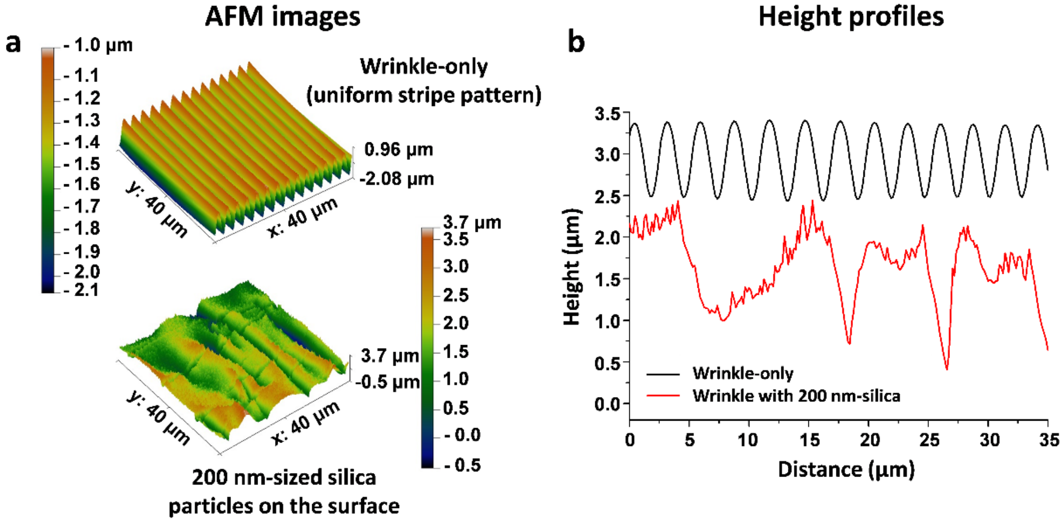

Figure 5.2 AFM images (a) and height profiles (b) of surfaces of the ‘wrinkle-only’ sample and the ‘wrinkle with 200 nm-silica’ at the released state. The latter sample was prepared by pre-stretching the film at 30%, followed by oxygen plasma treatment at 100 W for 3 min, and releasing the film.

We further use the optical microscope to image the wrinkle from the process over a larger area. **Figure 5.3** shows that the formation of wrinkling patterns is impeded by the presence of particles on the surface and the homogeneity of wrinkle formation is enhanced by using higher pre-stretch strain and longer plasma treatment time. As seen from the images with white frames, non-uniform wrinkles are formed when the pre-strain is less than 20% and/or plasma treatment time is less than 5 min, leading to patchy regions (red dotted circles) that have no apparent micron-sized wrinkles or their amplitude is small. The images with pink frames show that more uniform wrinkles prepared from larger pre-strain (≥30%), followed with 1-5 min plasma treatment or from pre-strain 20% sample but longer plasma treatment time (≥5 min). Finally, images with yellow frames show larger sized wrinkles with fewer lateral cracks when pre-strain is ≥30%, and oxygen plasma treatment is at the higher end, 5 min. These results suggest that NPs could inhibit wrinkle formation. However, when exposed to longer plasma treatment time and/or higher pre-stretch strain, wrinkle formation could occur uniformly over a large area.

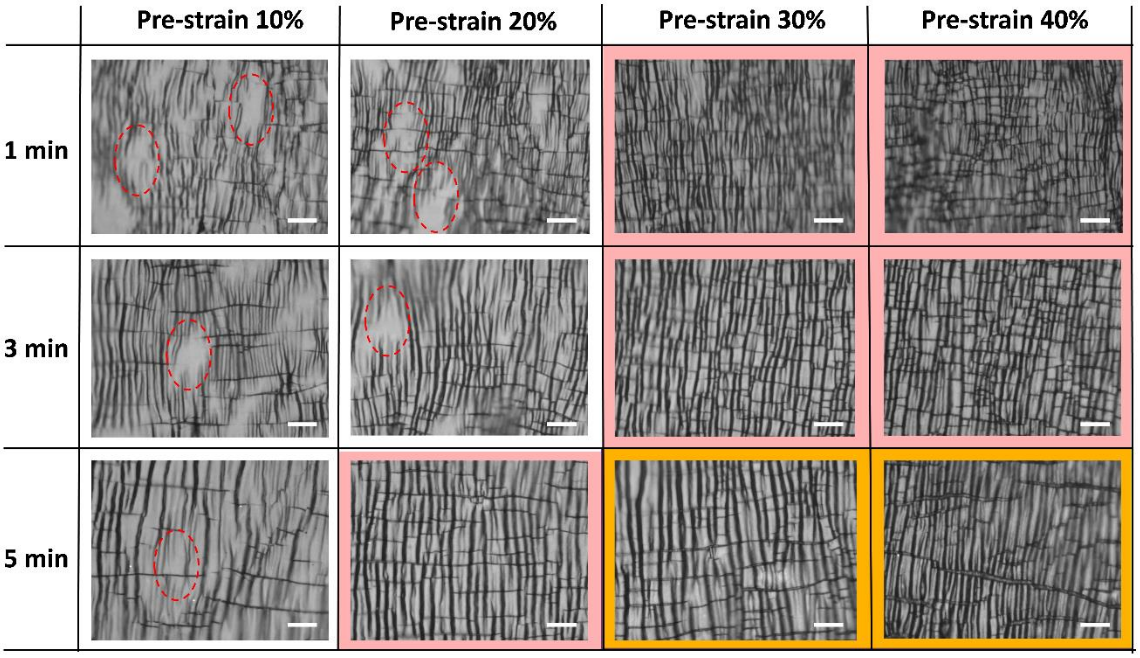

Figure 5.3 Optical microscope images of particle-embedded wrinkles prepared with variable pre-strains and plasma treatment times. All images were taken at the initial state with 0% of applied strain.

To confirm the roles of NPs and the underlying elastomer film, we compare surface morphologies of three kinds of particle-embedded wrinkling patterns prepared from different pre-strains (10, 20, and 30%) at a fixed plasma treatment time (3 min). SEM images in **Figure 5.4** show that as the pre-strain level increased, more lateral cracks were generated on the particle-embedded wrinkling patterns This might be attributed to more localized buckling imposed by the particles during wrinkle formation, thereby generating more of lateral cracks, which can affect the overall optical transmittance of films.

The presence of particles embedded in wrinkling patterns can significantly affect the formation of nanovoids and the generation of secondary wrinkles after the pre-strain due to the changed elastic moduli at the particle/PDMS interfaces, thereby affecting the overall optical transmittance of the film. Thus, we demonstrated how the size of particles (200 nm, 500 nm, and 1 μm) can affect the morphology of wrinkles when the composite films are stretched above the pre-strain . Then, we characterized their surfaces using SEM at 40% of applied strain (see **Figure 5.5**). When the particle diameter is 200 nm, we observe formation of secondary wrinkles perpendicular to the orientation of primary wrinkles, similar to that observed in wrinkle-only systems.[10] The secondary wrinkles appear quasi-ordered too, much like to the initial wrinkles. In contrast, when NP diameter is 500 nm or larger, formation of secondary wrinkles is impeded (see **Figure 5.5c**).

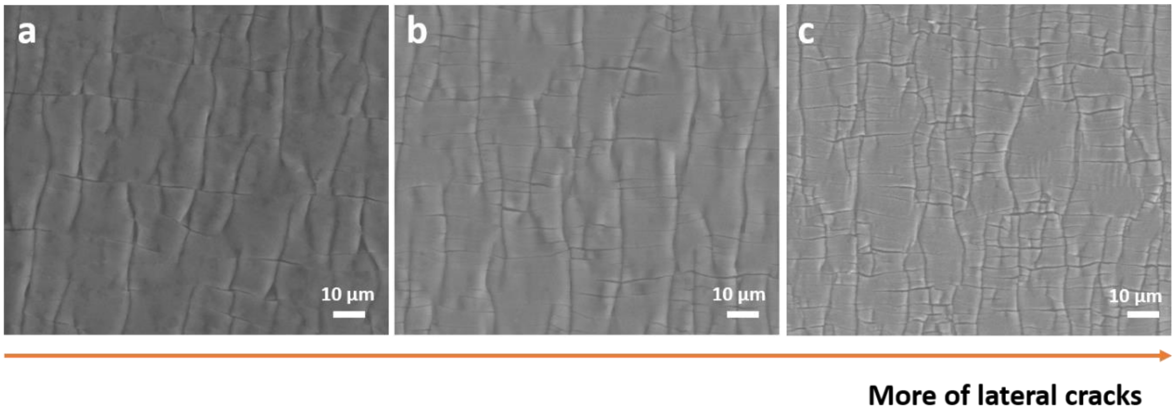

Figure 5.4 SEM images of the particle (diameter: 200 nm)-embedded wrinkles prepared by different pre-strains; 10% for a), 20% for b), and 30% for c). All images were taken at the initial state (0% of applied strain).

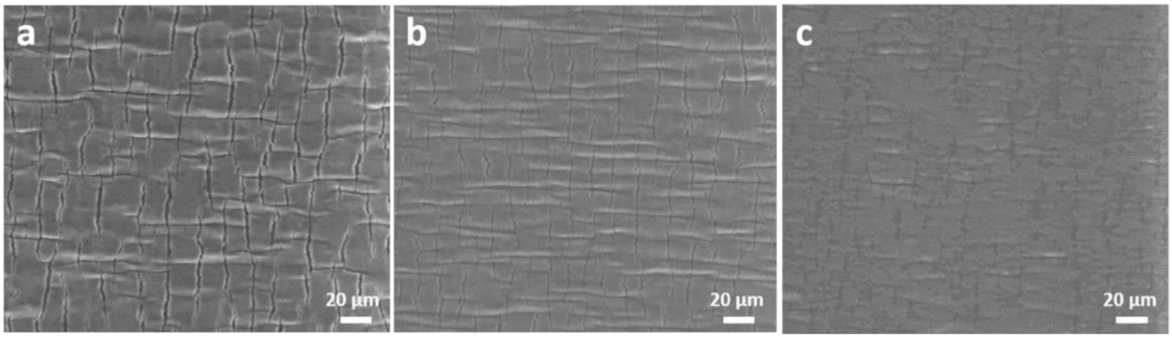

Figure 5.5 SEM images of the particle-embedded wrinkles prepared by using different particles with various diameter. (a) 200 nm. (b), 500 nm. (c) 1 μm. For all samples, 20% of pre-strain, 3 min of plasma time, and 100W of plasma power were used.

To confirm the generation of microcracks aligned perpendicular to the stretching direction and nanovoids around NPs, we compare the surface morphologies of particle-embedded wrinkling patterns prepared by pre-strain 20% at different applied strains (see **Figure 5.6**). As **Figure 5.6a** shows, wrinkles observed before the pre-strain level (at 10% of applied strain) are not yet flattened, and thus nanovoids around cracks were not observed wrinkles. At 20% of applied strain, the wrinkles are now nearly flattened, and the generation of nanovoids was still not observed (**Figure 5.6b**). When the applied strain exceeds the pre-strain level, then now the nanovoids around the microcracks were created on the surface (**Figure 5.6c**). Thus, we can confirm that the generation of microcracks and nanovoids around the NPs are initiated as the applied strain increases beyond the pre-strain level.

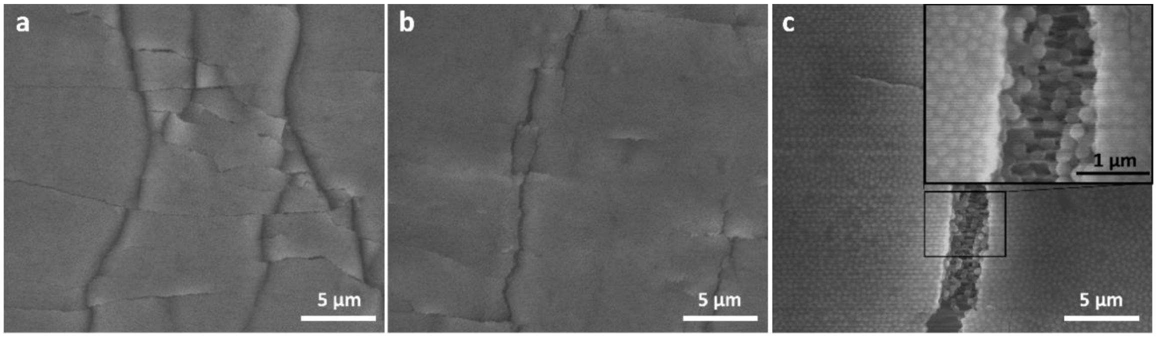

Figure 5.6 SEM images of the particle-embedded wrinkles prepared observed at various applied strains. (a) 10%, (b) 20%, (c) 30%. For all samples, wrinkles were embedded with 200 nm-sized silica NPs and prepared by 20% of pre-strain, 3 min of plasma time, and 100W of plasma power.

5.3.2 Optical properties of particle-embedded wrinkling patterns

We characterize the optical properties of the composite film consisting of both NPs (diameter, 200 nm) and surface wrinkles. To demonstrate the tunable transparency from particle-embedded wrinkle films under various strains, we took photos of the film under the light panel (white LED light source) at the center (i) and outside (ii) of the light beam to characterize the intensity of transmitted light and the resultant angle-dependent color changes, respectively (see **Figure 5.7a**). The film looks opaque before the pre-strain (30%) due to the scattering from the quasi-ordered wrinkles on the surface and it gradually becomes more and more transparent, reaching the maximum transparency at pre-strain (30%). At 60% of strain, the film looks opaque possibly (less angle-dependent) due to the scattering from the microcracks and nanovoids around NPs. Schematic illustration in **Figure 5.7b** shows the proposed mechanism of switchable transparency-opacity of the particle-embedded wrinkle film. Before pre-strain level (0-30% of applied strain), the quasi-ordered wrinkles can act as surface grating inducing diffusive-scattering of light, reducing the intensity of the transmitted light through the film. Surface roughness caused by the NPs also might affect the unselective scattering of light from the surface. When wrinkles are stretched to nearly flattened at pre-strain (30%), the intensity of transmitted light is increased, and the film looks much more transparent. After the pre-strain level, micro-scaled cracks and nano-sized voids can be formed due to the large mismatch in elastic modulus between silica NPs (E ~ 73 GPa)[28] and PDMS (E ~1.8 MPa)[29, 30]. NPs become gradually separated from each other upon stretching (0-30% strain), followed by the formation of nanovoids surrounding NPs after the pre-strain level, which can act as physical confinement to guide the crack formation. Thus, the opacity of the film can be increased by scattering from micro-scaled cracks and nano-sized voids around the particles. The yellowish tint appeared on the opaque film stretched at 60% applied strain (see **Figure 5.7**) results from the reflectance of light at UV wavelengths when the particle size is 200 nm.

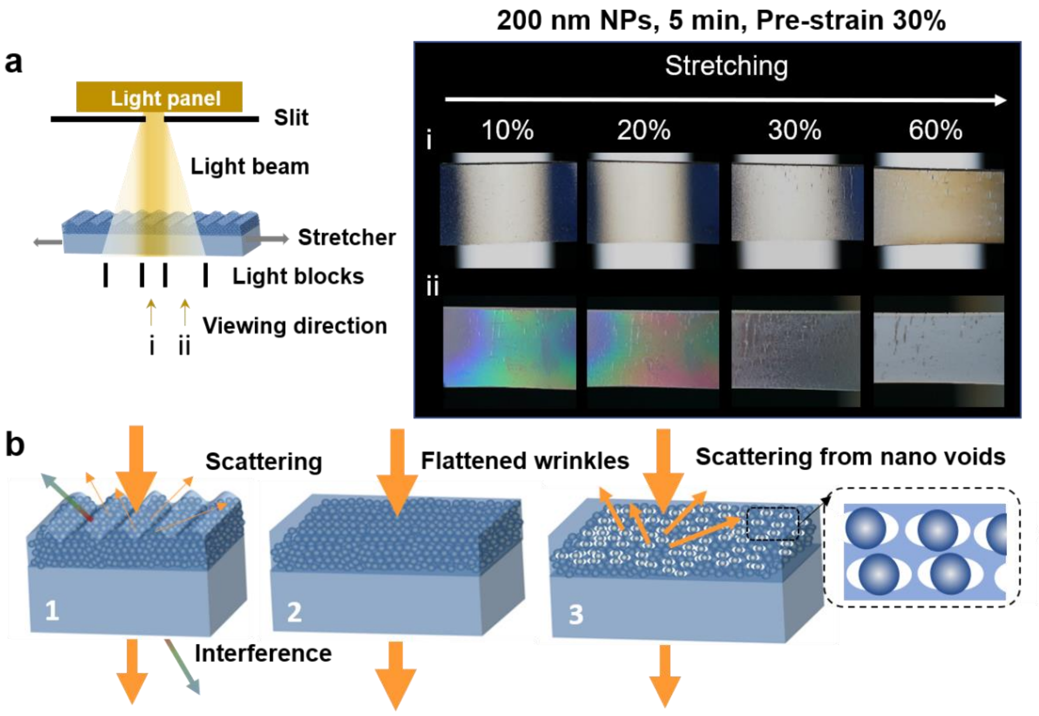

Figure 5.7 Optical properties of NPs (diameter, 200 nm)-embedded wrinkles, and their mechano-opto- responses. a) Schematic illustration of the setup for photographs and measurement of optical transmittances of the film at different applied strains (10-60%) seen in different viewing directions. b) Schematic illustration of the mechanism of the change of optical transmittance when stretching the particle-embedded wrinkle film.

From the optical microscope images and corresponding SEM images shown in **Figure 5.8**, we confirm that particle-embedded wrinkling patterns are nearly flattened at pre-strain level (30%), and micron-scaled cracks are generated when the film is stretched to 40% beyond pre-strain. Bluish color is generated by the light scattered from the nanovoids surrounding 200 nm-sized NPs formed around the cracks.

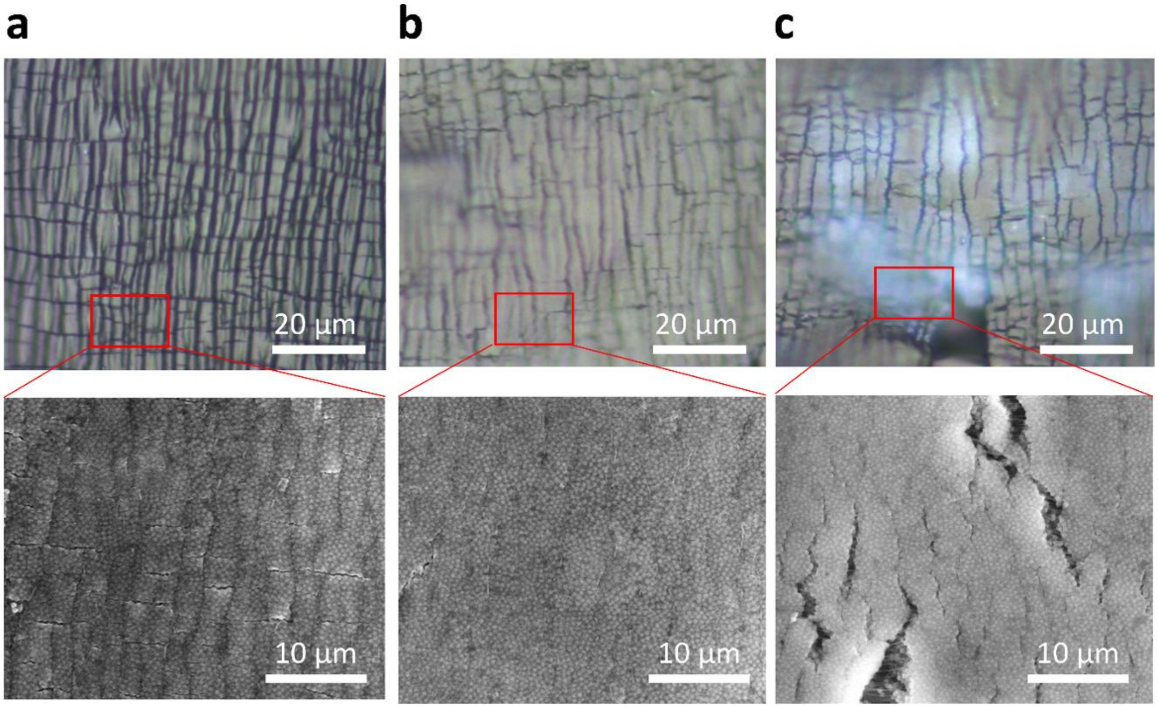

Figure 5.8 Optical microscope images (upper row) and the corresponding SEM images (lower row) showing the surface morphologies of particle-embedded wrinkling patterns at different applied strains. (a)10%, (b) 30%, and (c) 40%.

We then measure the optical transmittance of particle-embedded wrinkle composite films prepared from different pre-strains (10, 20, 30, and 40%) as a function of the applied strain (0-40%) (see **Figure 5.9**). For the particle-embedded wrinkles prepared by 1 min of O_2 plasma treatment, the highest transmittance of pre-strain 10% sample was observed at an applied strain of 5%, well-below the pre-strain due to the non-uniform generation of wrinkles over the surface. For pre-strain 20%, 30%, and 40% samples, they also exhibit maximum transmittance at an applied strain that is below the corresponding pre-strain level. In the case of the samples prepared from oxygen plasma for 3 min and 5 min, the transmittance peaked when the applied strain was close to the pre-strain, which was due to the regular scattering effect from the generation of particle-embedded wrinkles that occurred uniformly over the large area of the surface without an appearance of flat, empty regions. These results are in a good agreement with the results previously shown in **Figure 5.3**.

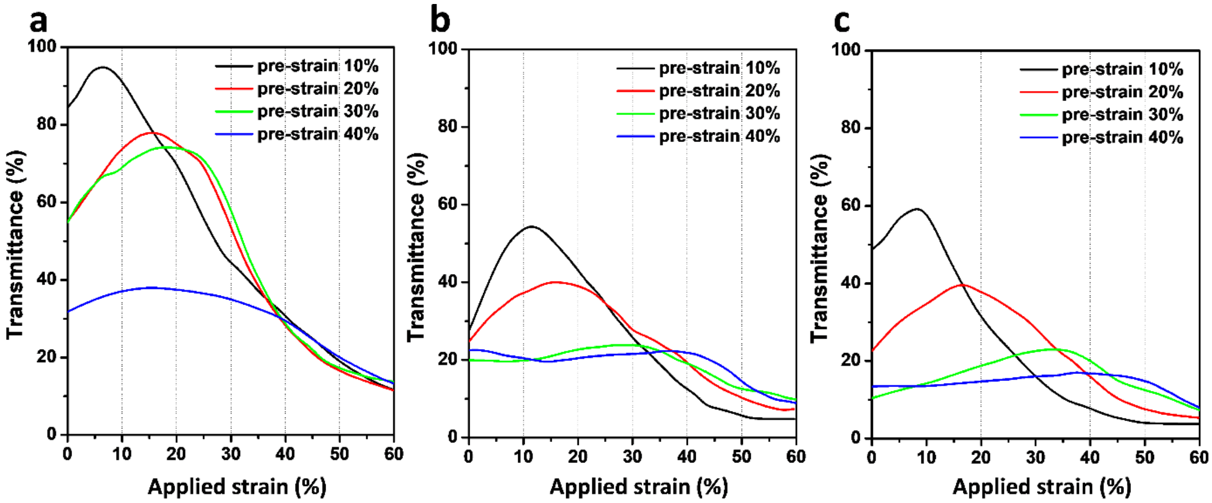

Figure 5.9 Optical transmittance (λ = 600 nm) of the particle-embedded wrinkle composite films vs. the applied strain (0-40%). The composite films are prepared from different pre-strains (10, 20, 30, and 40%) and O_2 plasma treatment time. (a) 1 min. (b) 3 min. (c) 5 min.

In **Figure 5.10**, we compared optical transmittance of the particle-embedded wrinkle composite films prepared from different pre-strains (10, 30, and 40%) in the visible to near infrared (NIR) regimes. For all samples, we could observe opacity in the initial state and before reaching the transmittance peaks. Around the peaks, transmittance intensities measured from different wavelengths were similar since the diffraction and interference of light were reduced when wrinkles are nearly flattened. Even after the applied strain is greater than the pre-strain, the transmittance intensities measured at different wavelengths still appear similar to each other, which might be attributed to the unselective scattering from microcracks and nanovoids. We could observe that the applied strain required to achieve the highest transmittance is close to the pre-strain.

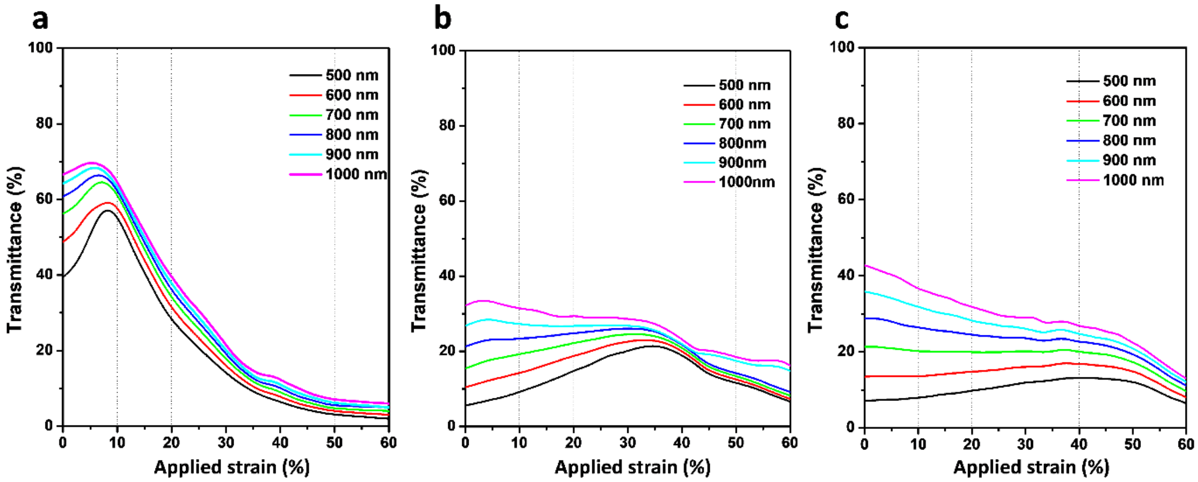

Figure 5.10 Visible-NIR optical transmittance (500-1000 nm) of the particle-embedded wrinkle composite films prepared from different pre-strains vs. the applied strain of (a)10%, (b) 30%, and (c) 40%. Oxygen plasma time is 5 min for all samples.

Particle size is also another importance variable to control the optical transmittance of the composite films. **Figure 5.11** shows the optical transmittance of the particle-embedded wrinkle composite films prepared from different sized NPs (diameter: 200 nm, 500 nm, and 1 μm). Their transmittance looks very similar to each other at the initial state (strain: 0%), where the diffraction grating effect from the initial wrinkles does not change much as the particle size increases. At applied strain of 10%, transmittance of the films increases as the particle size increases, probably due to the more flattened surface morphology as we discuss earlier that larger NPs will impede wrinkle formation (see **Figure 5.5**).

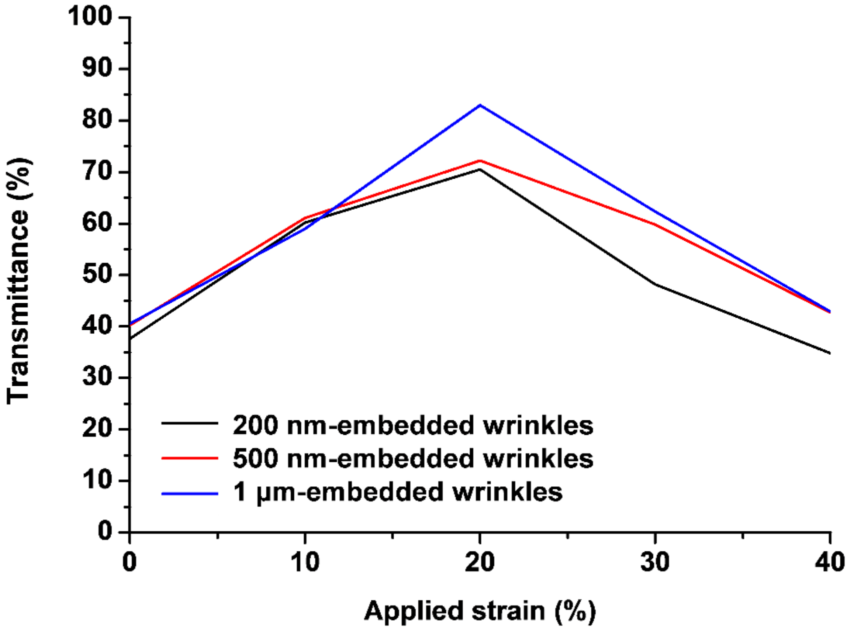

Figure 5.11 Optical transmittance of the particle-embedded wrinkle composite films measured at 600 nm wavelength. Three different particle sizes, 200 nm, 500 nm, and 1000 nm, are used. Pre-strain is 20% and oxygen plasma time is 5 min for all samples.

5.4 Conclusions

We fabricate the particle-embedded PDMS composite films with wrinkles on the same side of NPs and demonstrate mechano-responsive optical properties. Different from the case of wrinkle-only patterns, particle-embedded wrinkle patterns are not very ordered. We confirmed that the formation of wrinkle patterns is impeded by the presence of particles on the surface and the homogeneity of wrinkle formation is increased by higher pre-stretch strain and longer plasma treatment time. More lateral cracks were generated on the particle-embedded wrinkling patterns when the pre-strain was increased. When the applied strain exceeds the pre-strain level, the particle-embedded wrinkles are flattened, and nano-voids around the NPs and the micro-cracks aligned perpendicular to the stretching direction are formed. The highest transmittances are achieved from the films treated by oxygen plasma for 3 min or longer when the applied strain is equal to pre-strain. It seems that before reaching the pre-strain the diffraction grating effect from wrinkles and scattering from the lateral cracks dominate; after the pre-strain scattering from the nanovoids and the micro-cracks perpendicular to the stretching direction dominates. Further, we show that larger sized particles (diameter of 500 nm-1 μm) could impede the formation of secondary wrinkles. Therefore, we could control the optical transmittance of films by varying the pre-strains and the size of particles separately. In the future, we will focus on comparing the diffusive scattering from the quasi-ordered wrinkles generated at the particle-embedded surfaces vs. the one from the ordered wrinkles generated at the PDMS-only surfaces to confirm if the uniformity or angle-dependency of transmittance can also be improved by incorporating NPs into the wrinkling patterns. Further, we will study how the distribution of NPs and the thickness of NPs can affect geometries of wrinkles based numerical simulation different from the general wrinkle equations, estimating how the elastic modulus mismatch at the particle-PDMS interfaces affect the local formation of wrinkles on the surface.

5.5 References

[1] B. Jiang, L. Liu, Z. Gao, W. Wang, *Adv. Opt. Mater.* **2018**, *6*, 1800195.

[2] S. G. Lee, D. Y. Lee, H. S. Lim, D. H. Lee, S. Lee, K. Cho, *Advanced Materials* **2010**, *22*, 5013.

[3] H. Sun, S. Liu, W. Lin, K. Y. Zhang, W. Lv, X. Huang, F. Huo, H. Yang, G. Jenkins, Q. Zhao, W. Huang, *Nat. Commun.* **2014**, *5*, 3601.

[4] G. H. Lee, T. M. Choi, B. Kim, S. H. Han, J. M. Lee, S.-H. Kim, *ACS Nano* **2017**, *11*, 11350.

[5] F. Cellini, S. Khapli, S. D. Peterson, M. Porfiri, *Appl. Phys. Lett.* **2014**, *105*, 061907.

[6] J. Li, J. M. Shim, J. Deng, J. T. B. Overvelde, X. L. Zhu, K. Bertoldi, S. Yang, *Soft Matter* **2012**, *8*, 10322.

[7] S. G. Lee, D. Y. Lee, H. S. Lim, D. H. Lee, S. Lee, K. Cho, *Advanced Materials* **2010**, *22*, 5013.

[8] E. Lee, M. Zhang, Y. Cho, Y. Cui, J. Van der Spiegel, N. Engheta, S. Yang, *Advanced Materials* **2014**, *26*, 4127.

[9] H. X. Xu, C. J. Yu, S. D. Wang, V. Malyarchuk, T. Xie, J. A. Rogers, *Adv Funct Mater* **2013**, *23*, 3299.

[10] P. Kim, Y. Hu, J. Alvarenga, M. Kolle, Z. Suo, J. Aizenberg, *Adv. Opt. Mater.* **2013**, *1*, 381.

[11] D. Ge, E. Lee, L. Yang, Y. Cho, M. Li, D. S. Gianola, S. Yang, *Advanced Materials* **2015**, *27*, 2489.

[12] R. Zhang, Q. Wang, X. Zheng, *J. Mater. Chem. C* **2018**, *6*, 3182.

[13] Z. W. Li, Y. Zhai, Y. Wang, G. M. Wendland, X. B. Yin, J. L. Xiao, *Adv. Opt. Mater.* **2017**, *5*, 7.

[14] A. C. C. Rotzetter, R. Fuhrer, R. N. Grass, C. M. Schumacher, P. R. Stoessel, W. J. Stark, *Adv Eng Mater* **2014**, *16*, 878.

[15] B. A. Belyaev, V. V. Tyurnev, V. F. Shabanov, *Opt. Lett.* **2014**, *39*, 3512.

[16] P.-C. Lin, S. Yang, *Soft Matter* **2009**, *5*, 1011.

[17] J. Yin, J. L. Yagüe, D. Eggenspieler, K. K. Gleason, M. C. Boyce, *Advanced Materials* **2012**, *24*, 5441.

[18] D. Maji, D. Das, J. Wala, S. Das, *Sci Rep* **2015**, *5*, 17776.

[19] E. Cerda, L. Mahadevan, *Phys. Rev. Lett.* **2003**, *90*, 4.

[20] P.-C. Lin, S. Vajpayee, A. Jagota, C.-Y. Hui, S. Yang, *Soft Matter* **2008**, *4*, 1830.

[21] Y. Zhang, H. Hu, X. Pei, Y. Liu, Q. Ye, F. Zhou, *Biomaterials Science* **2017**, *5*, 2493.

[22] J. Tang, H. Guo, M. Zhao, J. Yang, D. Tsoukalas, B. Zhang, J. Liu, C. Xue, W. Zhang, *Sci Rep* **2015**, *5*, 16527.

[23] H. Guo, J. Tang, M. Zhao, W. Zhang, J. Yang, B. Zhang, X. Chou, J. Liu, C. Xue, W. Zhang, *Nanoscale Res. Lett.* **2016**, *11*, 112.

[24] D. Chandra, S. Yang, P.-C. Lin, *Appl. Phys. Lett.* **2007**, *91*, 251912.

[25] Z. Li, J. Xiao, *Extreme Mechanics Letters* **2015**, *4*, 118.

[26] J. Cui, B. Zhang, J. Duan, H. Guo, J. Tang, *Sensors* **2016**, *16*, 2131.

[27] H.-N. Kim, D. Ge, E. Lee, S. Yang, *Advanced Materials* **2018**, *30*, 1803847.

[28] C. Wan, B. Chen, *Nanoscale* **2011**, *3*, 693.

[29] K. M. Choi, J. A. Rogers, *Journal of the American Chemical Society* **2003**, *125*, 4060.

[30] F. Schneider, T. Fellner, J. Wilde, U. Wallrabe, *Journal of Micromechanics and Microengineering* **2008**, *18*, 065008.

CHAPTER 6. Summary and outlook

6.1 Summary

In this thesis, we develop new composite films by assembling silica nanoparticles (NPs) into different micron-scaled geometries and embedding them into selected polymer media for potential applications, including photovoltaics, photobioreactors, and solar-integrated smart windows. First, we control the assemblies of NPs and explore the effect of the size and geometry of the micro-confinement to the resulting optical properties. By embedding the assembled NPs into hydrogels or elastomers with matching refractive index, we explore synergistic optical effects, that is on-demand light scattering modulated by micro-scaled geometries and controllable reflectance of light attributed to nano-scaled periodicity, respectively, for optimized scattering, reflectance, and transparency, and their mechano-responsiveness.

In Chapter 1.1, I review different kinds of particle-polymer composites films for light-modulation applications. Polymers with high dielectric permittivity have been used for embedding NPs that are optically interesting but chemically vulnerable, e.g., metallic NPs, QDs, metal oxide NPs, and some of stimuli-responsive NPs. Polymers can also be used to support the optical properties of NPs by enhancing dispersion of NPs or tuning the effective refractive indices of composite films. Further, stimuli-responsive polymers embedded with NPs were also introduced as media that are dynamically tunable responsive to external stimuli. Thereby, the distance between the optical NPs and the arrays of NPs can be tuned, and thus the resultant optical properties of systems can be changed. In Chapter 1.2, I review the basic principles of light propagation including light scattering, the angular distribution of light scattering (Mie scattering phase function), diffraction of light by gratings, and thin film interferences in structured materials. In Chapter 1.3, I review the development of assembling NPs into different geometries (e.g., 2D and 3D colloidal crystals, photonic balls, and quasi-amorphous arrays) and how the reflectance or scattering of light from those structures can be controlled by the size of particles, the spacing between the particles, and the geometry of the assemblies. In Chapter 1.4, I show the previous studies on fabricating particle-polymer composites that can exhibit tunable optical behaviors in responsive to thermal, magnetic, mechanical, and electromechanical stimuli. I summarize approaches for creating patterned polymeric structures such as a hexagonal array of micron-sized circular holes and micron-sized wrinkles for strain-dependent deformation and the resulting optical properties, which is one of the main focuses of this thesis as detailed in Chapter 4 and 5.

In Chapter 2, we develop composite films to mimic giant clam iridocytes that can deliver equal, optimally efficient ″doses″ of sunlight to all photosynthetic algae cells packed in micropillars, while harnessing the entire solar flux. Backed by the numerical calculation and optimization on light scattering, the design, synthesis, and characterization of the synthetic scatterers that recapitulate the salient forward-scattering behavior of the Tridacnid clam system are reported. We present the first geometric solution to allow narrow, precise forward redistribution of flux, utilizing the solar resource at the maximum quantum efficiency possible in living cells. Our synthetic iridocytes are composed of silica NPs in microspheres embedded in low-refractive-index gelatin media. They exhibit wavelength selectivity with little loss (the back-scattering intensity is reduced to less than ≈0.01% of the forward-scattered intensity) and narrow forward scattering cone similar to giant clams. Moreover, by comparing experiments and theoretical calculation we confirm that the non-uniformity of the scatter sizes is a ″feature not a bug″ of the design, allowing for efficient, forward redistribution of solar flux in a micrometer-scaled paradigm. This method is environmentally benign, inexpensive, and scalable to produce optical components that will find uses in efficiency-limited solar conversion technologies, heat sinks, and biofuel production.

In Chapter 3, we detail the characterization of the optical properties of the synthetic iridocytes we have developed in Chapter 2. We measure the scattering intensity at given angles in both forward directions (θ = 0°-50°) and backward directions (θ = 110°-165°) to analyze the scattering phase function (angular dependent scattering behavior) of our composite film. Furthermore, intra-film radiometry is performed to characterize the light distribution at each depth of the composite film. We confirm that our composite film recapitulates the optical properties of clam iridocytes in the forward angles.

In Chapter 4, we design composite films consisting of wrinkles on top of the elastomeric poly(dimethylsiloxane) (PDMS) film and a thin layer of silica NPs embedded at the bottom is prepared as on-demand mechanoresponsive smart windows. By carefully controlling the wrinkle geometry, the mechanical strain, and size of silica NPs, a large degree of optical transmittance changes in the visible (Vis) to near-infrared (NIR) range with a relatively small mechanical strain (as small as 10%) is achieved. The sample from 10% pre-strain has shallow wrinkles with a low amplitude resulting in moderate transmittance (≈60.5%) (initially) and the highest transmittance of 86.4% at $\lambda = 550$ nm after the pre-strain.[1] Stretching beyond the pre-strain level with an additional 10% and 30% of mechanical strain results in a drastic decrease in the optical transmittance, 39.7% and 70.8%, respectively. The large drop of transmittance is caused by the combined effects from the formation of secondary wrinkles and nanovoids generated around the particles. The sample from 20% pre-strain possesses wrinkles with a moderate depth, showing 36.9% of optical transmittance in the initial state, and the highest transmittance of 71.5% at 550 nm when it is stretched to the pre-strain.[1] Further stretching results in further opacity similar as that seen from the 10% pre-strain sample.

In Chapter 4, we achieve large degrees of switching between transparency and opacity with a rather small mechanical strain (≈10%).[1] However, using wrinkle patterns for mechano-responsive optical applications have limitations: 1) Angle-dependent diffraction grating effect for wrinkle surface leads to non-uniform colors and non-homogeneous optical transmittance. 2) Random cracks are formed in the films. 3) The change of transmittance vs. a given strain is gradual not in a narrow window. Building upon the study in Chapter 4 of stretchable NP/PDMS composite films with wrinkles and NPs on different sides of the PDMS film, in Chapter 5 we fabricate mechano-responsive films with quasi-ordered wrinkles generated on the top surface of particle-embedded PDMS films to achieve more uniform optical transmittance as a result of diffusive scattering and reduced angle-dependent diffraction gratings. To create quasi-ordered wrinkles, we first assemble NPs on top of PDMS matrix, followed by oxygen plasma to generate wrinkle. The presence of the NPs and the size of the particles can significantly affect the wrinkle formation. For example, small-sized NPs (diameter <200 nm) tend to dissipate the compressive stress in the film generated by the mismatch of elasticity between silica and PDMS. Meanwhile, the mismatch of elastic modulus between silica NPs and PDMS can also cause surface buckling. The presence of NPs in PDMS will increase the elastic modulus of the soft layer, further complicates the wrinkle generation. In this chapter, we detail how to control the wrinkle formation and the resulting morphologies (amplitude and wavelength), crack formation, and the orientation or uniformity of the resulting wrinkles. As a result, we show that particle-incorporated wrinkling patterns exhibit relatively larger amplitudes and wavelengths than those obtained from PDMS only films. Along the lines, we study that the presence of particles and the size of particles to the formation of both initial and secondary wrinkles, and the resulting optical transmittance of films, which can be harnessed in strain sensors or on-demand smart window applications.

6.2 Outlook

The design and characterization of particle-polymer composite films reported in this thesis offer new insights for optimized designs of optical components to guide and modulate light. Building upon the studies in Chapters 2-3, we are currently experimenting to create clam-mimic photobioreactor designs combining synthetic iridocyte layer and synthetic algal pillars. We pattern transparent hydrogels into vertical micropillars to use them as media where algae can be cultivated so that we take advantage of the spatial redistribution of incoming solar flux in the system of scattering film-hydrogel pillars to assist photosynthesis of algae. Biocompatible poly(ethylene glycol) diacrylate

(PEGDA) hydrogel is selected as media to mimic the low refractive index and water-absorbing property of clam tissue (cytoplasm). We cover the synthetic iridocyte layer on top of the synthetic algal pillar arrays with the expectation that it can deliver equal, optimally defined ″doses″ of sunlight downward to feed algae at all region of pillars. In the future, we plan to optimize the composition and microstructure of PEGDA gel patterns to improve the fatality of algae on the surface of PEGDA gels.

Although we currently use 120 nm-300 nm silica NPs to weakly back-reflect the unwanted visible wavelength in photosynthesis, we can broaden the scope of particle sizes to modulate different wavelengths of light. For example, we can assemble larger particles with a diameter of 400 nm-600 nm into microspheres and thus back-reflect NIR light to protect algae from being exposed to heat, while simultaneously delivering visible light to them. Moreover, we can expand the scope of research by using other responsive materials introduced in Chapter 1, e.g., thermo-responsive poly(N-isopropylacrylamide (PNIPAM) and vanadium dioxide (VO_2) particles instead of silica NPs. It has been shown that PNIPAM nanogels can achieve temperature-responsive light scattering properties and back-reflectance[2, 3] We can also use silica NPs as core materials and coat them with either VO_2[4] or PNIPAM as shell layers so that we can assemble the composite particle into microspheres in water-in-oil emulsion systems. Then, we might be able to use the composite microspheres as synthetic iridocytes for thermo-responsive scattering. Furthermore, we can explore the porosity of microspheres that can be manipulated by mixing different sizes of NPs together in aqueous solution during the emulsification process. Then, we can harness the porosity of spheres as one of the experimental variables to vary the effective refractive index and fine-tune the scattering behavior of the synthetic iridocytes.

We can also expand the scope of applications beyond photobioreactors by incorporating the synthetic iridocyte layer with photoelectrodes for photovoltaic applications. Then, we can expect wavelength-selective light modulation and enhanced solar harvesting efficiency in photovoltaic applications. Current photovoltaics, including dye-sensitized solar cells (DSSCs) and perovskite solar cells, are based on nanostructures, which brings low defect-tolerance. Even the light harvesting efficiency is not very high enough to compensate for the disadvantages. Previously, inverse opals[5] and high refractive index materials[6] have been used in photoelectrodes to improve the light harvesting in solar cells by back-scattering light. Here, we can potentially use our synthetic iridocytes as forward scatterers covering the top surface of photoelectrodes, achieving the spatially efficient light scattering in micronscale and while reflecting unwanted wavelengths in the backward directions. The geometric design of forward scatterers can also be utilized in solar panels for producing, storing, or preventing heat to provide enhanced temperature control in smart building applications.

On the fabrication of composite microparticles, we have used the emulsion-evaporation method, which is simple, yet cost-effective, environmentally benign, and scalable. The size is not uniform though, which is not a problem in use of forward scattering. For other applications, it may become critical to precisely control the size and size distribution of the microspheres. In this regard, it is suggested to look into latest microfluidic technologies that have shown capability to produce uniform sized (sub)-10 micron particles.[7, 8] The robustness of the synthetic iridocytes is another factor that could be improved. Our current synthetic iridocyte film is not highly resistant to mechanical force because the microspheres consisting of silica NPs, which are sintered to enhance the robustness in our current design, can still be broken by shearing.

On the smart window project, our mechano-responsive particle-wrinkle composites can be potentially used as a Venetian blind-like window film on the existing building windows or vehicle window screens. This mechano-responsiveness design could offer additional energy saving in operation compared to conventional smart glazing systems, which require use of electricity to switch and maintain the switched state.[1, 9] Meanwhile, our studies on particle-incorporated wrinkle patterns can provide improved understanding of wrinkle formation in composite materials, which will offer new opportunities to create mechano-responsive particle-wrinkle composites for other light-modulation applications (e.g., color displays and strain sensors).[10] For the applications in multifunctional windows and displays, it is suggested to explore responsive NPs coated with silica and embed the core/shell NPs into PDMS films. For example, we might be able to use thermo-responsive phase transition materials such as vanadium oxide (VO_2) NPs with a diameter of tens of nanometer,[11, 12] thermochromic upconversion NPs,[13] and thermochromic dye-NPs.[14] They can change their absorption behaviors in response to temperature change. As an example of photochromic materials, tungsten trioxide (WO_3) has attracted much attention due to its strong, stable, and reversible photochromic properties. For this reason, WO_3-incorporated nanocomposites such as WO_3-TiO_2[15] and WO_3-VO_2[16] have been investigated as functional photochromic materials upon bandgap photoexcitation in response to the external light stimuli. Multilayered electrochromic metal oxide (e.g., nickel oxide (NiO)) thin films have exhibited persistent and reversible color changes induced by an electrical field, which is suitable for the applications in smart windows and displays. [17, 18] By using different kinds of responsive NPs as cores and silica as passivation layer to enhance the chemical stability of systems, we could create multi-functional particle-embedded polymer films.

I currently investigate the use of thermochromic VO_2 NPs embedded in PDMS films to fine-tune the optical properties in the near infrared wavelengths to expand the scope of the smart window applications. VO_2 NPs exhibit an efficient metal-to-insulator transition at a certain temperature (≈68°C) so that the reflectance of NIR light can be increased at high temperature beyond the transition temperature. When VO_2 is doped with tungsten, the phase transition temperature can be decreased to 27-32°C depending on the concentration of dopants.[19-22] Simultaneously, we can expect mechano-responsive optical transmittance at visible wavelength due to the strain-dependent nanovoids generation as the same as in the previously demonstrated silica-PDMS systems. To suppress unwanted oxidization of VO_2, we coat silica as shell. Then, we can embed the silica-coated VO_2 NPs (overall size, 100 nm-200 nm) into the PDMS film to demonstrate thermo-responsive and mechano-responsive switching of optical transmittance.

As the next step of the research, we plan to characterize the thermo-responsive and mechano-responsive light transmittance of VO_2-SiO_2-PDMS composite films at different wavelengths from visible to NIR regime. Embedding silica-coated metallic (e.g., silver or gold) NPs into PDMS can also give rise to the development of tunable IR light reflectance and visible light transmittance upon heating and mechanical stretching. It is suggested to explore the effect of particle sizes (tens of nanometers to a few micrometers) and shapes (e.g. rods) to manipulate wavelengths of the light reflected from the composite films. Besides PDMS, elastomers such as thermoplastic polyurethane (TPU)-based materials[23, 24] that have high elasticity and high transparency, can be investigated to generate more durable mechano-responsive particle-polymer composite films for practical applications (e.g., car window, smart window, and stretchable sensors).

6.3 References

[1] H.-N. Kim, D. Ge, E. Lee, S. Yang, *Advanced Materials* **2018**, *0*, 1803847.

[2] L.-L. Yue, R. Xie, J. Wei, X.-J. Ju, W. Wang, L.-Y. Chu, *Journal of Colloid and Interface Science* **2012**, *377*, 137.

[3] L.-W. Xia, R. Xie, X.-J. Ju, W. Wang, Q. Chen, L.-Y. Chu, *Nat. Commun.* **2013**, *4*, 2226.

[4] Y. Gao, S. Wang, H. Luo, L. Dai, C. Cao, Y. Liu, Z. Chen, M. Kanehira, *Energy & Environmental Science* **2012**, *5*, 6104.

[5] S.-H. Han, S. Lee, H. Shin, H. Suk Jung, *Advanced Energy Materials* **2011**, *1*, 546.

[6] H. Dong, Z. Wu, Y. Gao, A. El-Shafei, B. Jiao, Y. Dai, X. Hou, *Organic Electronics* **2014**, *15*, 1641.

[7] Y. Y. C. Sang, E. Lorenceau, S. Wahl, M. Stoffel, D. E. Angelescu, R. Höhler, *RSC Advances* **2013**, *3*, 2330.

[8] W.-C. Jeong, J.-M. Lim, J.-H. Choi, J.-H. Kim, Y.-J. Lee, S.-H. Kim, G. Lee, J.-D. Kim, G.-R. Yi, S.-M. Yang, *Lab on a Chip* **2012**, *12*, 1446.

[9] Making Smart Windows that Are Also Cheap, https://www.technologyreview.com/s/420221/making-smart-windows-that-are-also-cheap/(accessed: March 2018).

[10] F. Li, H. Hou, J. Yin, X. Jiang, *Science Advances* **2018**, *4*, eaar5762.

[11] R. Arezou, H. Ali, N. Abdolrahman, *Journal of Physics D: Applied Physics* **2018**, *51*, 375102.

[12] J. Zhou, Y. Gao, Z. Zhang, H. Luo, C. Cao, Z. Chen, L. Dai, X. Liu, *Sci Rep* **2013**, *3*, 3029.

[13] O. A. Savchuk, J. J. Carvajal, C. Cascales, J. Massons, M. Aguiló, F. Díaz, *J. Mater. Chem. C* **2016**, *4*, 6602.

[14] W. N. Harrington, M. R. Haji, E. I. Galanzha, D. A. Nedosekin, Z. A. Nima, F. Watanabe, A. Ghosh, A. S. Biris, V. P. Zharov, *Sci Rep* **2016**, *6*, 36417.

[15] T. He, Y. Ma, Y. Cao, X. Hu, H. Liu, G. Zhang, W. Yang, J. Yao, *The Journal of Physical Chemistry B* **2002**, *106*, 12670.

[16] A. Kaushal, N. Choudhary, N. Kaur, D. Kaur, *Applied Surface Science* **2011**, *257*, 8937.

[17] C. Larson, B. Peele, S. Li, S. Robinson, M. Totaro, L. Beccai, B. Mazzolai, R. Shepherd, *Science* **2016**, *351*, 1071+.

[18] D. T. Gillaspie, R. C. Tenent, A. C. Dillon, *Journal of Materials Chemistry* **2010**, *20*, 9585.

[19] T. Paik, S.-H. Hong, E. A. Gaulding, H. Caglayan, T. R. Gordon, N. Engheta, C. R. Kagan, C. B. Murray, *ACS Nano* **2014**, *8*, 797.

[20] Z. Liang, L. Zhao, W. Meng, C. Zhong, S. Wei, B. Dong, Z. Xu, L. Wan, S. Wang, *Journal of Alloys and Compounds* **2017**, *694*, 124.

[21] Z. Peng, W. Jiang, H. Liu, *The Journal of Physical Chemistry C* **2007**, *111*, 1119.

[22] O. Y. Berezina, A. A. Velichko, L. A. Lugovskaya, A. L. Pergament, G. B. Stefanovich, D. V. Artyukhin, A. N. Strelkov, *Technical Physics Letters* **2007**, *33*, 552.

[23] P. Wang, B. Sun, Y. Liang, H. Han, X. Fan, W. Wang, Z. Yang, *Journal of Materials Chemistry A* **2018**, *6*, 10404.

[24] Y. Lu, J. Jiang, S. Yoon, K.-S. Kim, J.-H. Kim, S. Park, S.-H. Kim, L. Piao, *ACS Appl. Mater. Interfaces* **2018**, *10*, 2093.

APPENDIX A: Fluorescent dye-coupling and amine-functionalization of silica nanoparticles

Adapted from:

L. Tran*, H.-N. Kim, N. Li, S. Yang, K. J. Stebe, R. D. Kamien, and M. F. Haase* (2018), “Shaping Nanoparticle Fingerprints at the Interface of Cholesteric Droplets", Science Advances, 2018, 4, 10, eaat8597.[1]

A.1 Introduction

Dye-coupled silica nanoparticles are prepared to examine dynamic colloidal/surfactant assemblies at aqueous/liquid crystal interfaces result from the interplay between colloid/surfactants and liquid crystal organization. Thus, we modify the surface chemistry of silica particle with amine functional groups so that the surface charge of the particle changes from negative to positive, reducing particle aggregation at the aqueous/liquid crystal interfaces. Then, the hydrophilic surfactants dispersed in the outer water phase can surround the liquid crystal droplets as well as assemble the colloidal particles at the interfaces. Hence, we can shape the nanoparticle fingerprints pattern at the interface of aqueous/liquid crystal droplet by varying the concentration of surfactants and the size of nanoparticles. As the liquid crystal material, a homogeneous mixture of 5CB (4-cyano-4′-pentylbiphenyl) doped with CB15 [(S)-4-cyano-4-(2-methylbutyl)biphenyl] is used. For the surfactant, trimethyloctylammonium bromide (C8TAB) is used.[1]

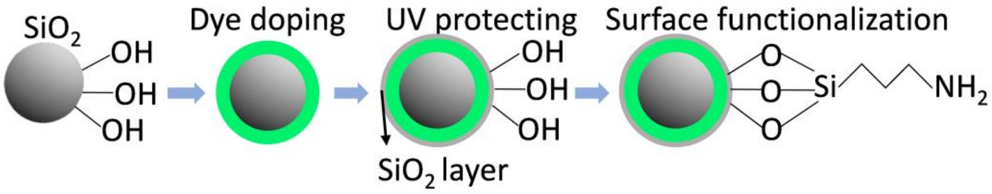

Figure A.1 Schematic illustration of the synthesis of amine-functionalized silica nanoparticle coupled with dyes.

A.2 Experimental methods

A.2.1 Materials

Amine-functionalized, fluorescent dye-coupled, 200 nm-sized silica nanoparticles are fabricated by the procedure described below. 200 nm-sized silica nanoparticles dispersed in DI water is purchased from General Engineering & Research. Materials, including fluorescein isothiocyanate isomer I (FITC), an aqueous solution of sodium hydroxide (NaOH, 0.1M), (3-aminopropyl)trimethoxysilane (APTMS, 97%), (3-aminopropyl) triethoxysilane (APTES, 99%), and tetraethylorthosilicate (TEOS, 98%), were purchased from Sigma-Aldrich. Ammonium hydroxide (NH_4OH, 30%) was purchased from Fisher Scientific.

A.2.2 Preparation of dye-coupled silica nanoparticles

The dye-coupled particles are synthesized following the procedure reported in our earlier paper.[2] Fluorescein isothiocyanate isomer I (FITC) molecules are covalently bonded with (3-aminopropyl)trimethoxysilane (APTMS). First, 0.0015 grams of FITC is added in 2 mL of ethanol and mixed with 0.237 mL of APTMS for 12 h under stirring. Then, silica nanoparticles (diameter, 200 nm) dispersed in DI water are re-dispersed in ethanol in a sonication bath for 1 h. Then, 2.755 mL of ammonia is mixed with 32.5 mL of an ethanol suspension containing 1 wt % of silica particles for 10 minutes. 0.689 mL of 0.1 M NaOH aqueous solution is added to the bath to activate the reaction. To couple the dye molecules to the silica nanoparticle surface, 208 μL of as-prepared, FITC-APTMS solution is added to the silica suspension. After 5 minutes of thorough mixing, 40 μL of TEOS is added drop-wise, and reaction time for 22 h under stirring. the resulting dye-coupled particles are washed with ethanol three times by centrifuging and replacing the supernatant with fresh ethanol.

A.2.3 Amine-functionalization of dye-coupled silica nanoparticles

The synthesis follows the procedure reported in the reference [3]. Briefly, for the functionalization of silica particles, 0.23 grams of silica pellet (as prepared above) is re-dispersed in 40 mL of fresh ethanol in a sonication bath. Under stirring with a Teflon-coated magnetic bar, 4 mL of ammonia solution (0.727 M in ethanol) is added. 170 μL of APTES solution (0.011 M in ethanol) is then slowly added drop-wise to the silica dispersion. After 15 hours, the resultant solution is washed with ethanol five times by centrifugation to remove the unreacted APTES molecules.

A.2.4 Characterization

FEI Quanta 600 Environmental Scanning Electron Microscope (ESEM) were used in 15 kV to characterize the morphology of surface-functionalized dye-coupled silica particles.

A.3 Results and discussion

As shown in the SEM image of **Figure A.2**, the spherical shape and the size of particles are maintained (200 nm-sized) even after the coating the exterior silica layer. The dispersion of surface-functionalized dye-coupled silica particles is also characterized. In **Figure A.3**, it seems that the particles are well-dispersed in both an ethanol solution (~1wt%) and in a pH =1 aqueous solution by naked eyes.

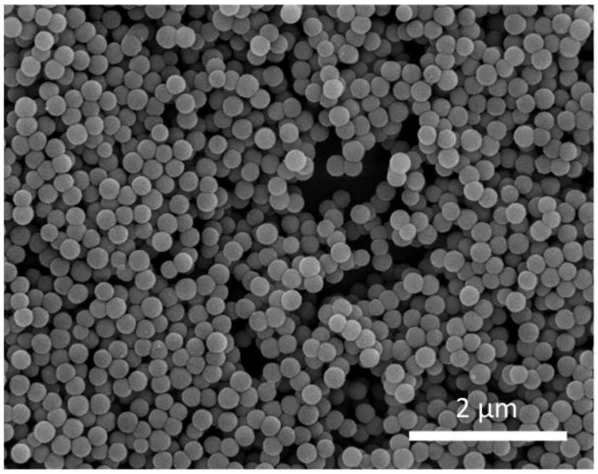

Figure A.2 SEM image of surface-functionalized dye-coupled silica particles.

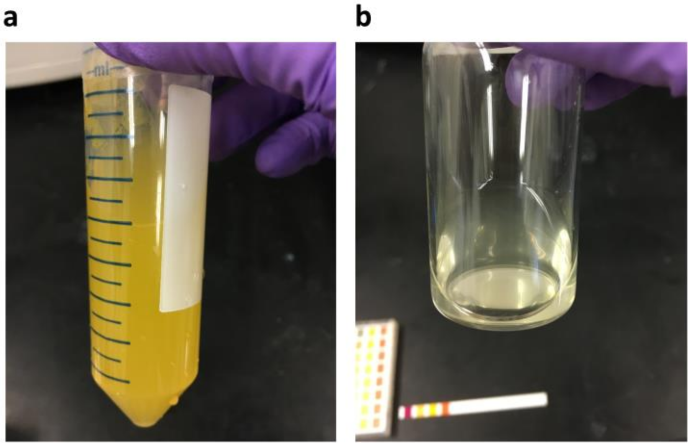

Figure A.3 Photograph images showing the dispersion of the amine-functionalized silica nanoparticles (200 nm-sized) in an ethanol solution (~1wt%) (a) and in a pH=1 aqueous solution (with HCl aq.) (b).

A.4 References

[1] L. Tran, H.-N. Kim, N. Li, S. Yang, K. J. Stebe, R. D. Kamien, M. F. Haase, *Science Advances* **2018**, *4*, 10, eaat8597

[2] S. Y. Lee, S. Yang, *Chemical Communications* **2015**, *51*, 1639.

[3] S. G. Jang, S.-H. Kim, S. Y. Lee, W. C. Jeong, S.-M. Yang, *Journal of Colloid and Interface Science* **2010**, *350*, 387.

APPENDIX B: Algal culturing and the fabrication of clam-inspired synthetic algal pillars

H.-N. Kim, S. Sen, and S. Yang*

We acknowledge Prof. Seth Herzon's group at Yale University for providing the initial batches of the brown algal cells with media and sharing the experimental procedure for the algal split with us.

B.1 Introduction

As the second part of the development of our clam-inspired photobioreactor design introduced in Chapter 2, here the fabrication of synthetic algal pillars is demonstrated (See **Figure B.1**). Sunlight levels that are too low or too high will limit or inhibit the photosynthetic reaction of algae.[1] Thus, the photosymbiotic algal cells are densely organized into vertical pillars in real clam tissue to protect themselves from strong sunlight.[1] For this reason, understanding the light transfer in pillars and optimizing it in confined pillar geometries would be a significant factor to be considered for developing the efficient photobioreactors. Mimicking realistic algae that are confined in deep and narrow pillars, synthetic algal pillars with the diameters of ≈ a few hundreds of μm and the aspect ratio of ≈1-4 are fabricated.

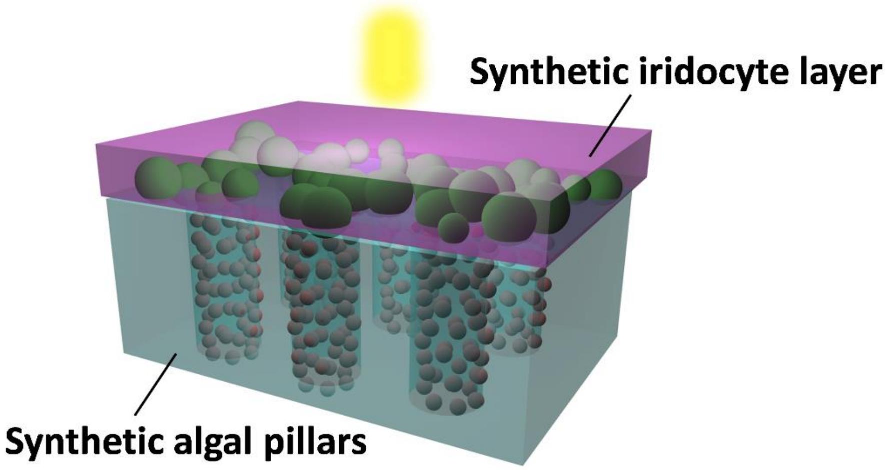

Figure B.1 Schematic illustration showing the design of a synthetic clam-inspired photobioreactor.

For demonstrating the photosymbiotic growth of algae inside the clam tissue, we have firstly cultivated algal batches in our lab and put the algae inside the synthetic pillars. By splitting them regularly every three weeks, we could observe happy, brown algae under the optical microscope. For materials, we have chosen to use hydrogels as extra-cellular matrix because they are mostly biocompatible and water-absorbable.[2, 3] Especially, using poly(ethylene glycol) diacrylate (PEGDA) hydrogels as materials for algal pillars is a good choice because they are nondegradable and able to be patterned into various geometries by UV-curing.[3] Further, they possess tunable physical properties (stiffness, elasticity) and anti-fouling effect, which is significant for algal cultivations. We add gelatin into the PEGDA hydrogels in different concentrations to induce further tunability in elasticity and toughness of the hydrogels.

B.2 Experimental methods

B.2.1 Algal culturing

Initially, the brown algal cells with media and the experimental procedure for the algal split were provided by Prof. Seth Herzon's group at Yale University (see **Figure B.2a**). To replace old media with new media containing fresh supplements, each algal batch is split into several batches (2-4) every three weeks. For the preparation of a fresh media solution, firstly ocean sea salt (7.4 g) is dissolved in 200 ml of DI water. The as-prepared sea salt water and the culture flask are sterilized by heating them up to 120 °C for 1 hr. The sea salt water is cooled down to room temperature. Then, 4 ml of supplemental media solution (Guillard's (F/2) Marine water enrichment solution, 50x, purchased from Sigma Aldrich, stored at -4˚C in freezer) is added to the sea salt water. Meanwhile, the glycerol and side product of the old batch is removed by centrifuging the supernatant (1500 rpm, 1 min). The remaining algal pellet is re-suspended in 1.2 ml of the as-prepared new media solution. Then, 100 μl of algal solution is added to each sterilized flask and 20-25 ml of the fresh media (salt water with supplements) is newly added. The new algal batches are located underneath a planting light source (15 W LED lamp) with an automatic timer for the light-sensitive culturing (time set: 14 hours of light and 10 hours of dark). After the split, the brown (not pale) algae were observed under the optical microscopy (see **Figure B.2b**)

B.2.2 Fabrication of synthetic algal pillars

15 wt% of PEGDA (Sigma Aldrich) in DI water and 1.5 wt% of photoinitiator (Ciba® IRGACURE® 2959) in 70% ethanol solution are prepared. Both solutions are sonicated for 10 minutes or until completely homogenized. Meanwhile, gelatin powder (Knox Gelatin) is dissolved in DI water (25 wt%). The gelatin solution is kept in an oven at 65ºC for at least 5 minutes. Then, 500 µl of the gelatin solution is added to 9 mL of the PEGDA solution and this mixture is sonicated for 2-3 minutes. Next, 100 µl of the photoinitiator solution is added to the mixture. The final mixture is transferred to a petri dish and the whole unit is purged with nitrogen gas for 3 minutes. Then, the purged mixture is UV-cured at 20K mJ/cm^2 dose. Finally, the cured hydrogel is cut into a small, rectangular block (size: 2 cm x 1.5 cm) and it is rinsed with 70% ethanol. Then, the micropillars are fabricated by using 3D printed scaffold (rigid polymer) while curing or punching the bulk hydrogel using a biopsy punch (inner diameter, 750 µm) (see **Figure B.3**). The diameter of pillars is controlled to be 500-700 µm and the overall thickness of the hydrogel block is 2 mm. The distance between the neighboring pillars is controlled to be over 1 mm so that they are not converged. The algal solution (5 times concentrated) from one batch is infiltrated into the micropillars in the hydrogel block. The hydrogel block containing algae is then immersed in the media solution and located underneath the planting light for algal growth.

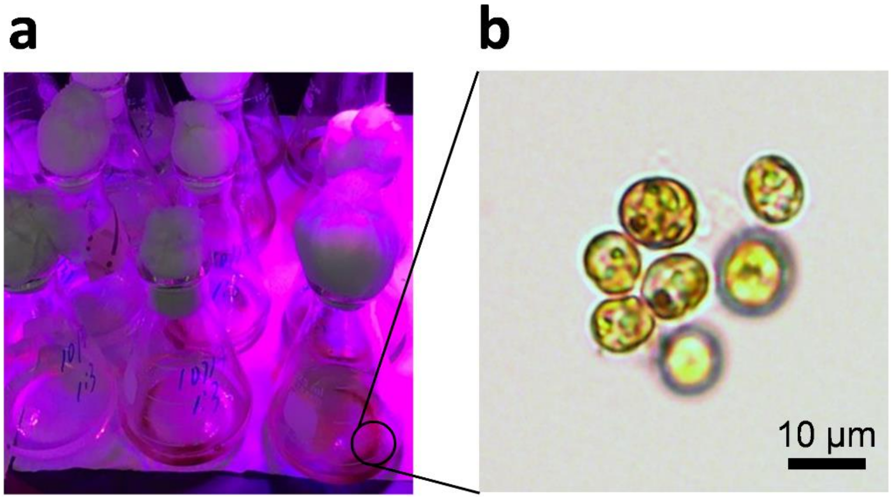

Figure B.2 (a) Algal culturing batches (initial ones from Prof. Seth Herzon's lab) and (b) An optical microscope image of happy, brown algal cells right after the algal split.

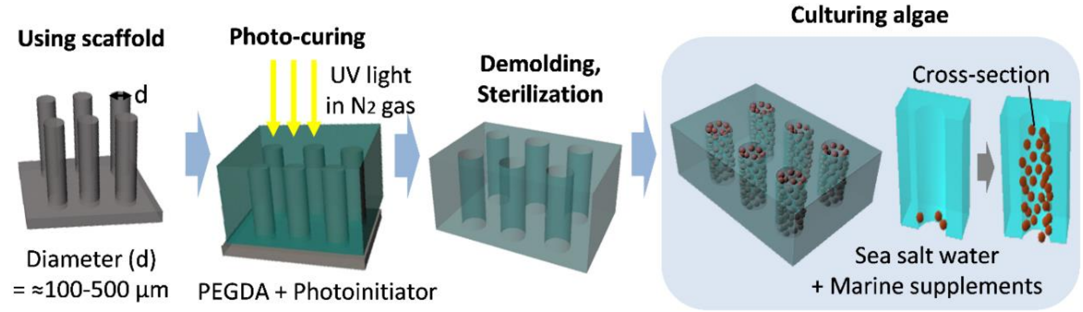

Figure B.3 Schematic illustration showing the preparation of synthetic algal pillars using the UV-curable PEGDA hydrogels.

B.3 Results and discussion

PEGDA channels (size of the hydrogel block: 2 cm x 1.5 cm) containing algal cells organized in vertical micropillars are fabricated (see **Figure B.4**). After 1 week, the algae grown under the planting light are observed. From the cross-section of the hydrogel block, we can observe algae grown at the bottom of micropillars by naked eyes. By optical microscope, we could confirm algae (white arrow in **Figure B.4e**) are growing well in the micropillars.

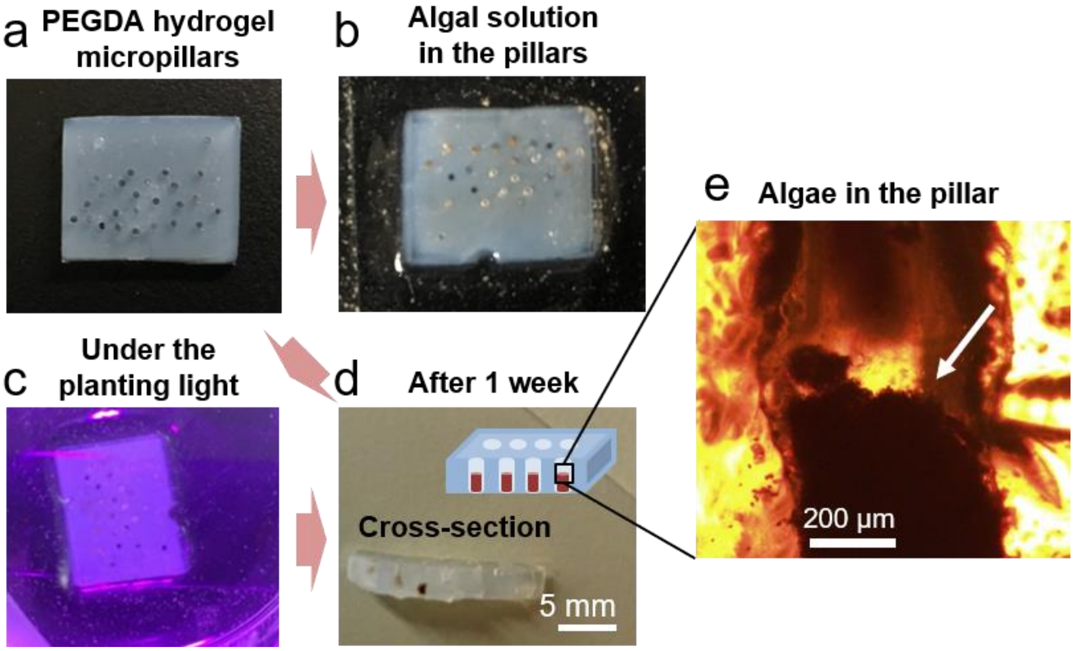

Figure B.4 Photograph images of the PEGDA hydrogel block with micropillars (a), the pillars with infiltrated algae (b), the hydrogel block under the planting light (c), the 1 week-old cross-section of the hydrogel block containing grown algae in the micropillars (inset: schematic diagram of the cross-section of the hydrogel block) (d), and the optical microscope image of algae grown in the pillars for 1 week (e).

For future work, we will observe the photosynthetic behaviors of algae in three different cases: (a) Algae on the flat substrate, (b) algae in the synthetic algal pillars, and (c) algae in the synthetic algal pillars underneath the synthetic iridocyte layer (see **Figure B.5**). Then, we might be able to explore how the confined geometry of algal pillars and the light distribution from synthetic iridocyte layer can affect the algal photosynthetic reaction in our synthetic photobioreactor design.

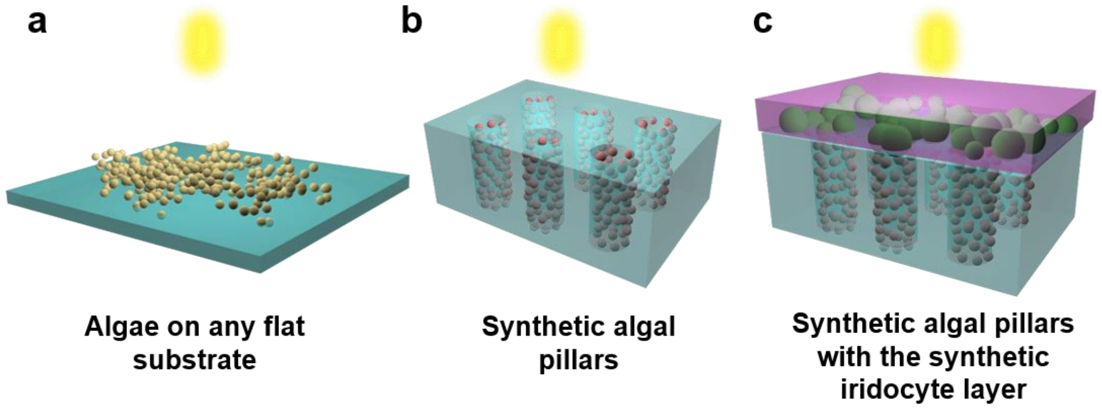

Figure B.5 Schematic illustrations showing (a) algae on any flat substrate, (b) algae in the synthetic algal pillars, and (c) algae in the synthetic algal pillars underneath the synthetic iridocyte layer.

B.4 References

[1] H.-N. Kim, S. Vahidinia, A. L. Holt, A. M. Sweeney, S. Yang, *Advanced Materials* **2017**, *29*, 1702922.

[2] X. Qin, Q. Hu, G. Gao, S. Guan, *Chemical Research in Chinese Universities* **2015**, *31*, 1046.

[3] M. Bae, R. Divan, K. J. Suthar, D. C. Mancini, R. A. Gemeinhart, *Journal of vacuum science & technology. B, Microelectronics and nanometer structures : processing, measurement, and phenomena : an official journal of the American Vacuum Society* **2010**, *28*, C6P24.

APPENDIX C: Synthesis of thermochromic vanadium dioxide (VO_2)/silica core/shell particles

C.1 Introduction

For demonstrating temperature-responsive smart window designs, we developed thermochromic composites using vanadium dioxide (VO_2) nanoparticles. VO_2 is a well-known thermochromic material since it exhibits a remarkable optical variation in the near-infrared regime from transmitting to reflecting upon the metal to insulator phase transition (MIT).[1-4] The development of VO_2 in energy-efficient windows has been hindered by high transition temperature (Tc), low luminous transmittance (T_{lum}), small solar modulation efficiency, the uncertainty of durability, and the lack of color change.[4] To address these problems, researchers have put many efforts in VO_2-based composite materials such as VO_2-WO_3 nanocomposites,[5] tungsten-doped VO_2 particles,[3] VO_2/SiO_2 core-shell particles.[6]

Here, we study the different morphologies of VO_2, so they can be utilized in practical smart window applications. By modifying the surface or coating passivation shells onto the surface of VO_2, we try to reduce unwanted oxidizations of VO_2. Coating VO_2 nanoparticles with a thin SiO_2 shell might significantly improve anti-oxidation, anti-acid abilities, and their optical performance. Gao et al. prepared transparent, stable and flexible VO_2-based thermochromic films composed of VO_2/SiO_2 core/shell composites.[6] The composite films exhibit UV-shielding properties and a significant thermochromism in the near infrared regime.

C.2 Experimental methods

C.2.1 Preparation of VO_2 nanoparticles by hydrothermal method

The procedure is done following or slightly modifying the steps outlined in the reference [6]. 0.125 g of V_2O_5 powders (Sigma Aldrich) are added into 40 mL of oxalic acid dihydrate ($C_2H_6O_6$) (Sigma Aldrich) aqueous solution (0.15 M in DI water). After thorough stirring for 10 min, a grey-white precipitate is formed. Then, the precipitate is washed with DI water for 3 times. 50 ml of the washed solution is transferred into 80 mL Teflon-lined stainless-steel autoclave. Then, we put the autoclave to heating-oven and heat up at 180 °C - 230 °C for 16-18 h. The hot autoclave is cooled down to the room temperature. The resulting VO_2 solution is washed with DI water, filtered by filter papers or porous sheets (the pore size > tens of μm), and air-dried.

C.2.2 Functionalization of VO_2 particles with PVP

The procedure is done following or slightly modifying the steps outlined in the reference [6]. As-prepared VO_2 particles are functionalized with PVP (poly-vinylpyrollidone, Mw=55,000 from Aldrich). Firstly, PVP is dissolved in DI water (concentration, 0.0256 g/mL). The PVP aqueous solution is mixed with as-prepared VO_2 solution in 1:2 volume ratio. The mixture is thoroughly stirred for 24 h to ensure complete PVP adsorption.

C.2.3 Preparation of VO_2/SiO_2 structure by TEOS hydrolysis (modified Stöber growth method)

The solution of PVP-treated VO_2 is centrifuged (8000 rpm, 15 min) for high purity. Then, the solution is transferred into 30 mL of ethanol and centrifuged again (8000 rpm, 15 min). After removing supernatant, 30 mL of fresh ethanol is added into VO_2 particles. After stirring them for 5 min continuously, we pour 2 mL of tetraethyl orthosilicate (TEOS, Sigma-Aldrich) which is pre-added in 8 ml of ethanol. To activate the silanol groups on the particle surface, we pour 2 mL of ammonia solution (28-30%, Fisher Scientific) which is pre-added in 8 ml of DI water. We keep the reaction for 12-13 h at 50 °C (temperature of the hot plate) under stirring. The resulting solution is washed with DI water three times for removal of remaining TEOS.

C.3 Characterization

FEI Quanta 600 Environmental Scanning Electron Microscope (ESEM) were used in 10-15 kV to characterize the morphology of VO_2 nanoparticles and VO_2/SiO_2 particles.

C.4 Results and discussion

VO_2 particles grown by the hydrothermal method have diameters of ≈200-250 nm and lengths of 3-5 μm. Depending on different temperature condition and reaction times, we could observe two different rod geometries of VO_2 (see **Figure C.1**). VO_2 rods prepared by the hydrothermal condition of 180 °C and 18h possess narrow and sharp rod-like shape. In contrast, VO_2 rods prepared by the hydrothermal condition of 210 °C and 17h possess wider and rather flat belt-like shape. **Figure C.2** shows the morphology of VO_2/SiO_2 core-shell composite particles. After coating SiO_2 onto the surface of VO_2, the flat and belt-like rods become less flat and more rounded. We could also observe many of silica spheres as byproducts. For future work, we will figure out how to avoid the generation of silica spheres during the coating reaction. Further, we will characterize the thickness of SiO_2 shell using transmission electron microscopy (TEM). Moreover, we will characterize the optical properties of the resulting VO_2/SiO_2 across the visible and infrared regime to see if the composites can be used as thermochromic materials for temperature-responsive smart window applications.

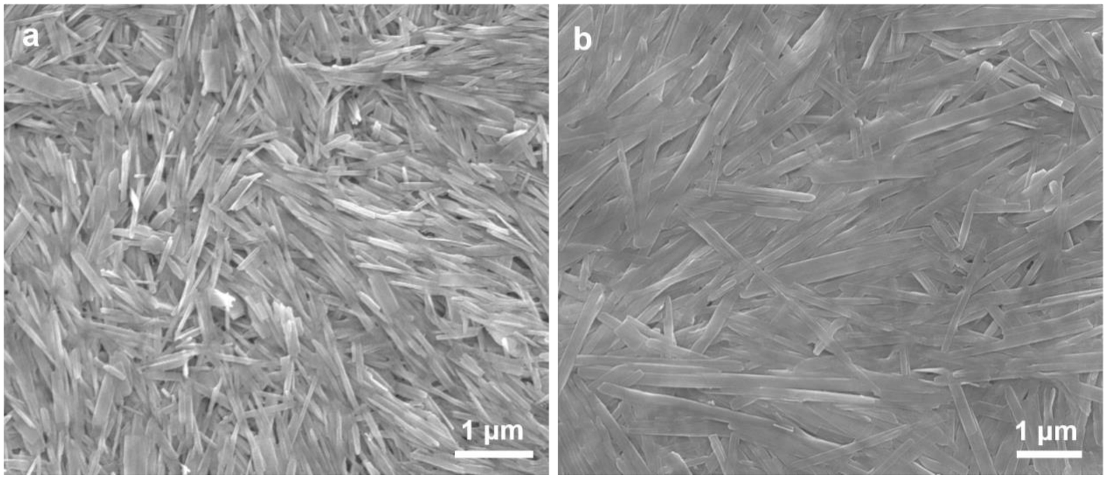

Figure C.1 SEM images of VO_2 particles. (a) VO_2 rods prepared by the hydrothermal reaction in 180 °C-autoclave for 18h (b) VO_2 rods prepared by the hydrothermal reaction in 210 °C-autoclave for 17h.

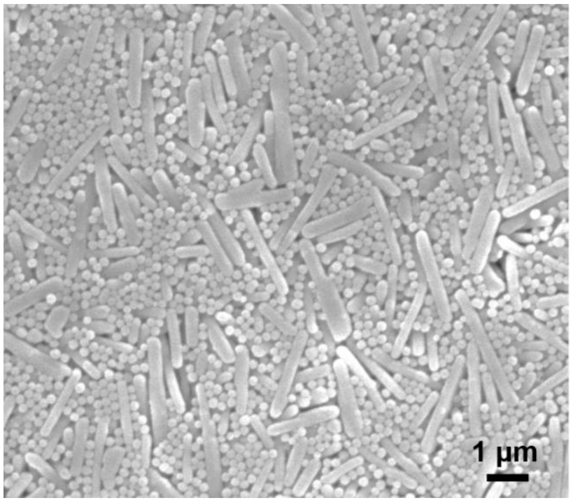

Figure C.2 SEM image of VO_2/SiO_2 core-shell composites. VO_2 rods were prepared by the hydrothermal reaction in 210 °C-autoclave for 17h.

C.5 References

[1] J. Zhou, Y. Gao, Z. Zhang, H. Luo, C. Cao, Z. Chen, L. Dai, X. Liu, *Sci Rep* **2013**, *3*, 3029.

[2] X. Xiao, H. Zhang, G. Chai, Y. Sun, T. Yang, H. Cheng, L. Chen, L. Miao, G. Xu, *Materials Research Bulletin* **2014**, *51*, 6.

[3] T. Paik, S.-H. Hong, E. A. Gaulding, H. Caglayan, T. R. Gordon, N. Engheta, C. R. Kagan, C. B. Murray, *ACS Nano* **2014**, *8*, 797.

[4] F. Xu, X. Cao, H. Luo, P. Jin, *J. Mater. Chem. C* **2018**, *6*, 1903.

[5] A. Kaushal, N. Choudhary, N. Kaur, D. Kaur, *Applied Surface Science* **2011**, *257*, 8937.

[6] Y. Gao, S. Wang, H. Luo, L. Dai, C. Cao, Y. Liu, Z. Chen, M. Kanehira, *Energy & Environmental Science* **2012**, *5*, 6104.

APPENDIX D: List of publications

1. **H.-N. Kim**, D. Ge, E. Lee, and S. Yang*, “Fabrication of particle-embedded wrinkling patterns for tunable mechano-responsive optical transmittance”, Manuscript in preparation.
2. L. Tran*, **H.-N. Kim**, N. Li, S. Yang, K. J. Stebe, R. D. Kamien, and M. F. Haase*, "Shaping nanoparticle fingerprints at the interface of cholesteric droplets", ***Science Advances***, 2018,4, 10, eaat8597.
3. **H.-N. Kim**, D. Ge, E. Lee, and S. Yang*, “Multistate and on-demand smart windows.” ***Adv. Mater.***, 2018, 30, 1803847.
4. **H.-N. Kim**, S. Vahidinia, A. L. Holt, A. M. Sweeney*, and S. Yang*, “Geometric design of scalable forward-scatterers for optimally efficient solar transformers.” ***Adv. Mater.***, 2017, 29, 1702922.
5. D. Ge, G. Wu, L. Yang, **H.-N. Kim**, W. Hallwachs, J. M. Burns, D. H. Janzen*, and S. Yang*, “Varying and unchanging whiteness on the wings of dusk-active and shade-inhabiting Carystoides escalantei butterflies”, ***Proc. Nat. Acad. Sci. USA*** 2017, 114, 7379
6. E. Lee, Y. Xia, R. C. Ferrier Jr., **H.-N. Kim**, M. A. Gharbi, K. J. Stebe, R. D. Kamien, R. J. Composto, and S. Yang*, “Fine golden rings: tunable surface plasmon resonance from assembled nanorods in topological defects of liquid crystals”, ***Adv. Mater.*** 2016, 28, 2731
7. M. A. Gharbi, I. B. Liu, Y. Luo, F. Serra, N. D. Bade, **H.-N. Kim**, Y. Xia, R. D. Kamien, S. Yang, and K. J. Stebe*, “Smectic gardening on curved landscapes”, ***Langmuir*** 2015, 31, 11135